AD-A186 464 THREE-DIMENSIONAL UNSTEADY FLOW ELICITED BY FINITE WINGS AND COMPLEX CONFIGURATIONS(U) AIR FORCE INST OF TECH WRIGHT-PATTERSON AFB OH J C ASHWORTH 1987 1/2

UNCLASSIFIED AFIT/CI/NR-87-142D F/G 1/1 NL

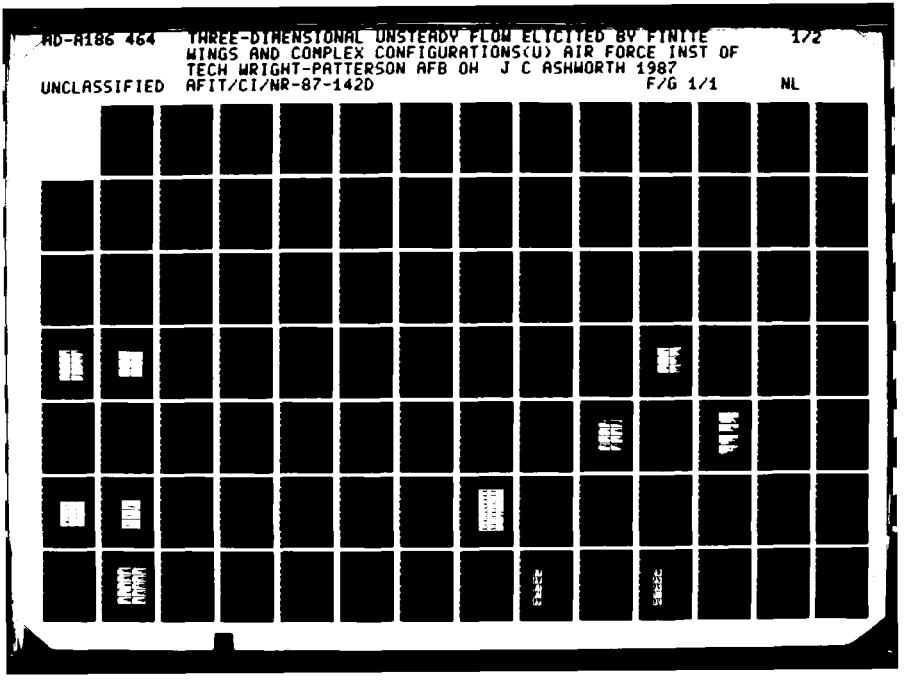

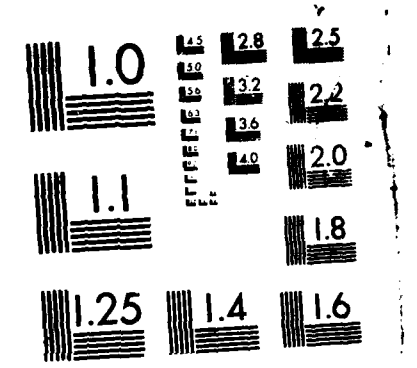

1412

THREE-DIMENSIONAL UNSTEADY FLOW ELICITED BY FINITE WINGS AND COMPLEX CONFIGURATIONS

BY

Jeffrey Clayton Ashworth

B.S., West Virginia University, 1971

M.S., West Virginia University, 1973

A thesis submitted to the

Faculty of the Graduate School of the

University of Colorado in partial fulfillment

of the requirements for the degree of

Doctor of Philosophy

Department of Aerospace Engineering Sciences

1987

UNCLASSIFIED
SECURITY CLASSIFICATION OF THIS PAGE *(When Data Entered)*

REPORT DOCUMENTATION PAGE		READ INSTRUCTIONS BEFORE COMPLETING FORM
1. REPORT NUMBER AFIT/CI/NR 87-142D	2. GOVT ACCESSION NO.	3. RECIPIENT'S CATALOG NUMBER
4. TITLE *(and Subtitle)* Three-Dimensional Unsteady Flow Elicited by Finite Wings and Complex Configurations		5. TYPE OF REPORT & PERIOD COVERED ~~THESIS~~/DISSERTATION
		6. PERFORMING ORG. REPORT NUMBER
7. AUTHOR(s) Jeffrey Clayton Ashworth		8. CONTRACT OR GRANT NUMBER(s)
9. PERFORMING ORGANIZATION NAME AND ADDRESS AFIT STUDENT AT: University of Colorado		10. PROGRAM ELEMENT, PROJECT, TASK AREA & WORK UNIT NUMBERS
11. CONTROLLING OFFICE NAME AND ADDRESS AFIT/NR WPAFB OH 45433-6583		12. REPORT DATE 1987
		13. NUMBER OF PAGES 178
14. MONITORING AGENCY NAME & ADDRESS*(if different from Controlling Office)*		15. SECURITY CLASS. *(of this report)* UNCLASSIFIED
		15a. DECLASSIFICATION/DOWNGRADING SCHEDULE

16. DISTRIBUTION STATEMENT *(of this Report)*

APPROVED FOR PUBLIC RELEASE; DISTRIBUTION UNLIMITED

17. DISTRIBUTION STATEMENT *(of the abstract entered in Block 20, if different from Report)*

18. SUPPLEMENTARY NOTES

APPROVED FOR PUBLIC RELEASE: IAW AFR 190-1

LYNN E. WOLAVER 26 OCT 87
Dean for Research and
Professional Development
AFIT/NR

19. KEY WORDS *(Continue on reverse side if necessary and identify by block number)*

20. ABSTRACT *(Continue on reverse side if necessary and identify by block number)*

ATTACHED

DD FORM 1 JAN 73 1473 EDITION OF 1 NOV 65 IS OBSOLETE

SECURITY CLASSIFICATION OF THIS PAGE *(When Data Entered)*

Ashworth, Jeffrey C. (Ph.D., Aerospace Engineering Sciences)

Three-Dimensional Unsteady Flow Elicited by Finite Wings and Complex Configurations

Thesis directed by Professor Marvin W. Luttges

Studies of two-dimensional unsteady separated flows have demonstrated possible aerodynamic benefits of controlled unsteady flows about airfoil surfaces. However, since all applicable wings are necessarily finite, a thorough understanding of three-dimensional unsteady flows is essential. Any direct application or modelling of this complex three-dimensional phenomenon may be somewhat premature until a characteristic data base is established.

The spatial and temporal transport, accumulation and dissipation of vorticity on the surface of three wings varying only in sweep angles (forward, straight and aft) were examined using flow visualization and hot wire anemometry techniques. Identical geometric positions were tested on each wing for a variety of dynamic parameters. Each sweep geometry produced distinct, time-dependent, spanwise and chordwise sites for vorticity accumulation into large scale leading edge and wingtip vortices. The wingtip and leading edge vortex interactions produced spanwise flow patterns uncharacteristic of two-dimensional flows. Wing sweep is a dominant geometric parameter in analyzing the effects of unsteady wingtip flow.

An initial investigation into the feasibility of unsteady flow application was performed on a model of the X-29 Forward Swept Wing Technology Demonstrator. This model geometry produces complex flow patterns but may be ideally suited for application of unsteady flow technology. Unsteady flow structures were observed which may ultimately generate beneficial, slow speed flight characteristics of advanced aircraft.

These investigations provide initial insight into three-dimensional flow behavior elicited by different sweep geometries and dynamic parameters. This attempt at visualizing possible benefits of forced unsteady flows predicts applicable areas for further study, and provides suggestive impetus for the exploitation of these flows to improve aerodynamic performance.

ACKNOWLEDGEMENTS

I would like to thank Dr. Marvin W. Luttges for his guidance and support throughout my endeavors as a graduate student. I appreciate the working relationship of friend and colleague. The assistance of Dr. Donald A. Kennedy, Dr. Peter Freymuth, Dr. C.Y. Chow and Dr. Frank Essenburg is also greatly appreciated.

The continuing technical support of Wolfgang Bank and Russel Meinzer has been invaluable throughout this research effort. I would also like to thank my friends and colleagues for their help and support. This work has been sponsored, in part, by the U.S. Air Force Office of Scientific Research, Grant F4962083K0009, Dr. James McMichael, project manager. My graduate program has also been sponsored by the Department of Aeronautics at the U.S. Air Force Academy.

Finally, I would like to dedicate this thesis to my wife Becky and my daughters Amy and Julie. Without their patience and support, it would not have been possible.

TABLE OF CONTENTS

FIGURES

Figure

CHAPTER I

INTRODUCTION

Fluid flow elicited about two-dimensional airfoils by airfoil pitching motions is known to enhance flow attachment and produce transiently large lift coefficients even at angles of attack well above static stall angles. All practical lift producing surfaces are, however, inherently three-dimensional. Therefore, before attempting application of unsteady flow technology, the implications of three-dimensionality of lifting surfaces must be realized for unsteady flow phenomena. Since high performance aircraft necessarily employ swept wing configurations, a combined investigation of three-dimensional, finite wing as well as wing sweep effects must be accomplished. These areas of aerospace technology have not been previously investigated for unsteady separated flows. This dissertation focuses on experiments that utilize sinusoidally driven three-dimensional wings to elicit unsteady flows. Variations in both geometric and dynamic parameters are related to systematic and reliable alterations in flow field structures and processes.

The experimental approach taken to achieve comprehension of finite, swept wing fluid dynamics includes orthogonal flow visualization using phase-locked stochastic evaluations combined

with hot wire anemometry techniques. Flow visualization was chosen to comprehensively record the complex three-dimensional flow patterns elicited about the complex test configurations. This data collection technique permits time-dependent flow field scrutiny for both spatial position of structures and directional interactions with freestream flow. Anemometric measurements added quantitative magnitudes and spatial verification to the visualized flow structures.

The experiments were designed to systematically evaluate and understand the effects of parameter changes on comprehensive, complex flow characteristics. Each investigation revealed unique relationships between test variables and flow structures and is discussed in each of the separate chapters that follow. Where possible, steady flow tests were performed to provide the foundation for comparisons with dynamic tests. Initial forward swept wing experiments evinced characteristics of finite wings and revealed effects peculiar to the distinct wing sweep angle. Sweep effects can only be evaluated when various sweep geometries are tested at otherwise identical geometric and dynamic conditions. Therefore, three wings varying only in sweep angle were evaluated using flow visualization techniques. These experiments disclosed distinct temporal and spatial sites for vorticity accumulation and transport for each of the three wing geometries. Further quantification of the unsteady flow fields about the distinct wings was accomplished using hot wire

anemometry. Complete analyses were achieved using both flow visualization and anemometric velocity data.

The collection of unique geometry, finite wing flow characteristics provided a basis for predicting the flow behavior about a much more complex geometry. For these tests a reflection-plane, X-29 aircraft model was used. This was a novel attempt to evaluate the application of three-dimensional unsteady flow technology to potentially beneficial aerodynamic flow characteristics over a complex model using dynamic forcing functions.

The overall comprehension of unsteady fluid behavior is discussed for this three-dimensional, finite wing analysis. However, to arrive at the current level of understanding of unsteady flows, the efforts of many previous investigators have preceded this work. Unsteady aerodynamics is a relatively youthful technology, but the application of limited forms of unsteady flows is not a recent breakthrough. Very few actual flight conditions exist where truly steady flow is incorporated. Initially, scientists and engineers studied unsteady flows only to predict how to prevent the occurrence of these poorly understood flows. Only recently have the possible benefits of these complex phenomena been envisioned. And since, these benefits have been the impetus for studies not unlike those reported here.

CHAPTER II

HISTORICAL REVIEW

Since man has walked on the Earth, he has marveled at the creatures that fly in the air. Nature's winged flyers were no doubt responsible for the first attempts at human flight. Man's first recorded, and probably many unrecorded, attempts at flying mimicked the unsteady flapping, twisting and bending wing motions of birds or other flyers. The arm strength required to support the human body weight aloft with these wing motions was prohibitive. Even early machines were not fast or powerful enough to drive wings through these unsteady motions and produce supporting lift and thrust. Man then turned to apparatus which developed lift and thrust by utilizing quasi-steady circular motions or immovable wings.

Many historical writings document the birth and development of manned aviation. One of these, compiled by Anderson (1978), traces modern aviation as evolving from Leonardo da Vinci, through hot-air balloons and gliders, to the first powered flight by the Wright brothers. Since the Wrights had no prior airplane references to follow, they put the tail of their flying machine in front of the main lift-producing wing. This configuration proved very unstable and resulted in a failure of

the first flight attempt due to aircraft stall. This tail-in-front or canard configuration is known to be somewhat unstable, but allows high maneuverability and may prove to be the ultimate high performance aircraft configuration some 80 or 90 years after the Wright Flyer. Since the first powered flight, convenience and necessity (military application in wartime) have provided impetus for expansion of the operating flight envelopes of every new aircraft design.

Another look toward nature may provide new insight into flight controllability in the very low airspeed regime. Many of nature's flyers utilize unsteady aerodynamics to produce lift and thrusting forces. For example, the dragonfly, as reported by Luttges, et al., 1985, Somps and Luttges, 1985 and Saharon and Luttges, 1987, has for millions of years been using unsteady large-scale vortices over tandem wings to produce lift magnitudes equal to 20 times dragonfly body weight. However, due to the complex nature of unsteady fluid dynamics, the possible utilization of this phenomenon for manned aircraft has only recently been investigated.

The basic research which precedes conceptual application of new aerodynamic technology has been pursued in a variety of parallel experimental and theoretical investigations. An attempt at detailed analysis of each study is beyond the scope of this review. Many of these studies have intentionally or otherwise made significant contributions toward advancing the science of

unsteady aerodynamics. This review briefly summarizes major areas of investigation and significant contributions toward the ultimate application of this relatively recent technology of unsteady aerodynamics. Since the focus of the present work is experimental in nature, only significant experimental work will be reviewed. For analytical and computational research efforts, the reader is referred to publications by authors such as McCroskey (1982), Telionis (1984) and Chow (1983).

Background Aerodynamics

Unsteady flows about lifting surfaces are dominated by the formation, accumulation and transport of vorticity. The subject of vorticity in conventional flows is discussed in nearly every comprehensive text on the theory of aerodynamics. Potential flow analysis encompassing flow away from the viscous effects of fluid-wall interactions is widely published and a thorough discussion can be found in the text by Karamcheti (1966). The behavior of fluid flow near solid surfaces can be predicted by solutions of the full Navier-Stokes equations of motion (Schlichting, 1968). These time-dependent equations relate velocity, pressure and viscosity in the three-dimensional boundary-layer space. Equations for flow vorticity are also widely published and are reviewed in texts by Kuethe and Chow (1976) and White (1974). Since some unsteady fluid motions produce three-dimensional vortical structures, the classical

Helmholtz Vortex Theorems are useful in analyzing this circular motion. Viscous effects near surfaces are unavoidable and a graphic display of the decay of vortex filaments in a viscous fluid are shown in the text by Kuethe and Chow (1976). The viscous fluid vortex equation contains the viscous diffusion term, and is known as the Helmholtz Equation of Hydrodynamics (White, 1974).

Initial Two-Dimensional Investigations

Initial studies of rapidly changing unsteady flows were conducted to find ways to eliminate adverse unsteady effects such as diverging flutter on wings, rotational flows in compressors, and gust response. One such investigation was undertaken on the dynamic retreating helicopter rotor blade stall that accompanies high loading and advance ratios (Martin, et al., 1974). Since this helicopter blade motion was cyclic, a sinusoidally pitching, two-dimensional airfoil was used to study the dynamic stall phenomenon. These tests incorporated flow visualization, static pressure and hot-wire velocity techniques. The formation and shedding of a leading edge vortex and the temporal effect of this vortex on pressure distribution, normal force, pitching moment and velocity profile are documented. These data agreed with earlier rotor studies, and suggest possible utilization of these unsteady flow fields for lift enhancement during portions of the cyclic rotor motion.

Further investigations with oscillating, two-dimensional airfoils expanded the parameter range to attempt more accurate prediction of the dynamic stall phenomenon. McCroskey, et al., 1975, collected flow visualization and pressure data about an oscillating airfoil and observed a boundary layer reverse flow which developed into a leading edge vortex. This study also revealed leading edge vortex convective velocities of 35 to 40% free stream velocity, formation of a second vortex near the midchord of the airfoil and shed vortices presumably fed vorticity by the abrupt unsteady separation of the turbulent boundary layer. McAlister and Carr (1979) visualized dynamic stall characteristics about a sinusoidally oscillating airfoil in a water tunnel. They observed the formation of multiple vortices in a shear layer which covered the top surface of the airfoil. Under repeatable oscillating conditions, this layer of vorticity progressed toward the leading edge of the airfoil and, with the sudden influx of fluid, coalesced into the dynamic stall vortex. Many parallel studies in unsteady fluid motion are documented and a comprehensive review of these efforts was published by McCroskey (1982). This review specified experimental and some theoretical approaches, parameter ranges and techniques to date.

Experiments in this area continued with two-dimensional studies on unsteady airfoils and flat plates conducted and published by Robinson and Luttges (1983). These experiments employed flow visualization and hot wire anemometry techniques to

record unsteady flow behavior about sinusoidally oscillating surfaces in a subsonic wind tunnel. During these tests, the sequence of leading edge vortex initiation, development and traversing was observed. Also, temporal shedding interactions between leading and trailing edge vortices were noted. When small amplitude oscillations were applied, there was an absence of large vortical structures. The presence of a leading edge vortex on the top surface caused reattachment of the flow at values where static separation occurred, and increased flow reattachment was noted with increasing K from 0.25 to 1.25. In these two-dimensional tests, increasing K incited smaller, more cohesive vortices with turbulent cores and high velocity circumferences. Lower K values precipitated larger leading edge vortices which became more turbulent as distance from the trailing edge decreased. It became apparent to the authors that the large scale leading edge vortices behaved in a predictable fashion and might be aerodynamically exploitable.

An initial investigation with swept surfaces was conducted by Carta (1983). This wind tunnel experiment utilized a NACA 0012 airfoil swept 30° to the freestream flow. The leading edge vortex convection across the aft portion of the chordlength of the swept airfoil was slower than observed for a geometrically similar airfoil mounted perpendicular to the freestream. With no three-dimensional wingtip effect, the swept airfoil leading edge vortex inception was independent of mean

angle of attack or amplitude of motion. Before stall occurred in the static tests, the lift coefficient for the swept airfoil attained higher magnitudes and angles of attack than the straight airfoil counterpart.

Two comprehensive review articles on two-dimensional unsteady flows were published and presented in 1985. The first, Reynolds and Carr, focuses on vorticity concepts and equations. This discussion notes that the time-mean vorticity flow rate is constant for a free-shear layer and the only source of vorticity along a flat surface is from viscous diffusion from the solid surface. It is also noted that the pressure gradient causes vorticity accumulation and formation of vortical structures in the boundary layer. Historical background and pertinent results of the dynamic stall process on airfoils are discussed. The second article, presented later by Carr, reviews unsteady flows by separately analyzing the effects of distinct variables. The author initiates the idea of expanding the low speed flight envelopes of future aircraft by applying forced unsteady flows.

Since many parameters affecting the formation of unsteady flow had been investigated, some research efforts were directed at the control of unsteady separated flow structures. Reisenthel and his colleagues (1985) investigated the flow over a two-dimensional flat plate with spoiler-like flaps and a backward step using flow visualization, static pressure measurements and hot wire anemometry. This wind tunnel test focused on low R

value (0.001 to 0.24), separated flow control of the interactions between the flap and step flow. Other studies by Luttges and his colleagues (1985) focused on visualizations of the flow patterns about two-dimensional flat plates and airfoils. These investigations incorporated sinusoidal pitching, longitudinal vortex generators and pulsed air injection to cause vortex formation. In these studies, increases in mean angle of attack caused earlier formation of the leading edge vortex while increasing K or oscillation amplitude caused later formation and greater convecting velocity. At higher angles of attack, a fluid reservoir or airfoil shadow was observed behind the leading edge where vorticity accumulates into large scale structures.

An extension of flow structure control was accomplished by Robinson and colleagues (1986) on two-dimensional airfoils in tandem configuration. An auto-rotating flat plate and an oscillating airfoil were used to generate an unsteady airflow upstream of a static airfoil. Flow visualization and pressure measurements recorded transient flow patterns and airloads over the trailing airfoil. Upper surface pressure coefficient data shows passage of the upstream-produced vortex over the trailing airfoil. The authors suspect the transient flow behavior over the aft wing may cause adverse control effects when applied to tandem configurations.

Accelerating Flows

A qualitative approach to investigating unsteady flow

field behavior has been taken by Freymuth and his colleagues (1984-86). A unique flow visualization technique was devised and employed to study vortical development during flows accelerated constantly from rest. This technique involves tagging fluid particles with dense white smoke produced when $TiCl_4$ is applied to the investigated surface. The smoke traces the streakline patterns developed during the flow acceleration, and provides an excellent medium for qualitatively observing the intricate flow structures produced by this unsteady flow. Numerous two and three-dimensional body shapes have been investigated successfully with this technique. Freymuth (1985) combined flow observations using this technique and others to publish a descriptive language (or nominal scaling) dictionary of dynamic separation patterns.

This flow visualization technique was initially applied to study cylinders, flat plates and airfoils at various angles of attack from below stall angles to as high as 90° to the freestream flow. Angle of attack and Re effects were observed from side and top view perspectives. Leading and trailing edge flow structure progression and ornamentation were visualized by applying the $TiCl_4$ along each or both of these surfaces and recording the development with high speed photographic techniques. Later experiments studied both leading edge and wingtip vortices in accelerating and steady flow. These top view sequences of a rectangular wing with smoke produced at the leading and trailing edges, provided initial three-dimensional

visualization of leading edge and wingtip vortex filament interaction. The test data show filaments nearly parallel to the leading edge of the wing that converge toward the forward edge of the wingtip. Also, the wingtip vortex converges toward this leading edge of the wingtip region. These flow patterns were consistently observed over numerous test conditions and wing geometries.

Pitching Airfoils

Parallel studies to the sinusoidal oscillation and accelerating flow tests are on unsteady flows produced about pitching airfoils. This method elicits an unsteady flow field by pitching an airfoil at high pitch rates to angles of attack well above static stall angles. The motion histories of the flow development were recorded using high speed photographic flow visualization, surface pressure measurements and hot wire velocity measurements. These investigations were conducted by Helin and Walker (1985), Walker and colleagues (1985) and Helin and colleagues (1986). The experiments evaluated effects of pitch rate, pitch axis and non-continuous pitching motions. Higher pitching rates caused dynamic stall to occur at higher geometric angles of attack and created more cohesive vortices. Moving the pitch axis aft along the chordline of the airfoil had an identical effect on the angular occurrence of dynamic stall. Increasing the pitch rate increased the maximum lift coefficient

while increasing the Re had an opposite effect. High rate pitching with short pauses was used to attempt to control the vortex structures on the surface of the airfoils.

Finite Wings

Investigations on unsteady flows about three-dimensional, finite wings show complex flow fields where interactions occur between leading edge and wingtip vortices. The complexity of these three-dimensional flows dictated flow visualization as the initial technique for analysis. Adler and colleagues (1983) utilized a smoke rake, flow visualization technique on both a two-dimensional airfoil and a three-dimensional wing. Later, Adler and Luttges (1985) concentrated on the three-dimensional effects of a sinusoidally oscillating, finite wing. The quantitative measurements accomplished were leading edge vortex temporal and spatial initiation, size and convecting velocities toward the trailing edge of the wing. The flow about the wing appeared to be characteristically separable into three distinct regions. The flow near the tip of the wing was dominated by the unsteady wingtip vortex. The wing midspan region supported interactions between the leading edge vortex and the wingtip vortex. Inboard toward the wing root, the flow behaved much like that observed during two-dimensional airfoil studies.

Finite wing investigations utilizing a water tunnel and flow visualization techniques were conducted by Gad-el-Hak and his colleagues (1983) and Gad-el-Hak and Ho (1985-86). Finite

wings with different sweep geometries and delta wings with different sweepback were tested in a towing tank. The delta wing studies during static conditions reveal shear layer roll-up into discrete vortices which form nearly parallel to the leading edge of the wing. When the delta wing was oscillated about the quarter chord point, the unsteadiness delayed separation and promoted hysteresis effects similar to those observed on two-dimensional airfoils. Wing sharp leading edges were observed to cause a larger vertical separation zone than more blunt leading edges. Comparisons between straight and swept wings demonstrate greater leading edge vortex dwell time for the forward swept wing and greater convective tendencies for the straight wing.

Experimental results of unsteady flows elicited by sinusoidally oscillating wings with different sweep geometry were published by Ashworth and colleagues (1986) and Ashworth and Luttges (1986). These three-dimensional studies are discussed later in this text. Other visualization experiments on three-dimensional unsteady separated flow were accomplished by Robinson and his colleagues (1986).

Advanced Prototypes

Any application of unsteady flow technology depends on aerodynamic advantages that might be realized on existing or future prototypes. Modern aircraft are typically designed for a particular mission. The concept of supermaneuverability, first

defined by Herbst (1983), envisions a highly maneuverable aircraft which is also efficient. To be efficient at high Mach numbers, aircraft must have swept wings (McCormic, 1979 and Busemann, 1971). This demanding combination of supermaneuverability and efficiency may only be satisfied through the use of unsteady separated flows on aircraft with swept wings. Yet, much research stands between this conceptual realization and the actual implementation of such ideas. Nevertheless, recent technology advances in structural materials and computer controls now permit aerodynamic design to match the demanding missions of future of aviation.

The recent technology of forward swept wings (Uhuad, et al., 1983) and canard-configured aircraft (Landfield and Rajkovic, 1986) may permit the effective operation of aircraft in flight regimes that have not been previously utilized. Flight of such vehicles may be thoroughly evaluated before manned flight through the use of advanced autopilot controls (Duke, et al., 1986). Advanced three-dimensional computational methods (Mann and Mercer, 1986 and Batina, 1986) may also prove useful in verifying such novel conceptual designs.

The X-29 Forward Swept Wing Technology Demonstrator is an example of the combination of recent technological developments (Hoey, 1985). The forward swept wing concept shows efficient operation at high Mach number flight (Moore and Frei, 1983). The root-to-tip stall characteristic of the forward swept wing

appears to be very beneficial at the low speed end of the flight envelope (Tierney, 1985). Wind tunnel investigations on scale models of this unique design (Whipple and Ricket, 1986; Griffin, et al., 1983) may show areas for possible application of unsteady aerodynamic technology. Basic research in steady as well as unsteady flows about advanced prototypes must continue.

CHAPTER III

METHODS

In order to attain clear pertinent results and to establish critical variables relating to three-dimensional unsteady flow traits, experimental techniques need be as exact and comparative as possible. The complex flow structures produced by sinusoidally driven, finite wings are somewhat difficult to record and analyze precisely. The cyclic, three-dimensional nature of these flows precludes instantaneous, single plane data acquisition. Therefore, any data recording technique must necessarily be time-dependent with maximum spatial resolution. Flow visualization techniques were employed throughout these experiments to observe the temporal and spatial flow fluctuations produced both by geometry changes and by dynamic parameter variations. Numerous quantitative flow characteristics such as vortex size, position, convective velocity, initiation point and tip deflection angle can be visually recorded. Subsequent comparative analyses can be readily accomplished. To further quantify flow characteristics, velocity measurements were documented using hot wire anemometry. Both of these data acquisition techniques possess inherent limitations which prevent precise flow quantification, however,

both present excellent comparative attributes. These two data recording techniques, when used together, provide flow field comparisons which clearly define crucial effects of geometric and dynamic parameters on finite wing aerodynamics.

The systematic investigations discussed in this text were conducted using different wind tunnels and methods of data collection and reduction. Since the focus of these studies is toward understanding low speed, unsteady flow characteristics, all experiments were performed in the subsonic wind tunnels at the University of Colorado. Each test was designed to scrutinize the effects of specific parameter variations. The apparatus and methodology of each investigation are discussed in the order of test chronology.

The initial forward swept wing (FSW) experiments and the geometric comparative studies between the forward swept wing (FSW), straight wing (STW) and aft swept wing (ASW) were conducted in the 16 by 16 inch test section wind tunnel. The test section side wall and top are constructed of cast acrylic Plexiglas such that flow could be visualized from any perspective. Walls not used for specific visualization perspectives were painted flat black to help reduce light reflections during flow visualization tests. The tunnel freestream velocity (V_∞) was recorded by a reference pitot tube located in the test section. The velocities were set to achieve Reynolds numbers (Re) based on wing chordlength of 30,000 and

40,000.

A hollow core aluminum NACA 0015 airfoil section with 6 inch chordlength was used to manufacture the three wings. The wings were each constructed with the chordline swept at a different angle: (1) a forward swept wing, $\Lambda = 30°$ forward; (2) a straight wing, $\Lambda = 0°$; and, (3) an aft swept wing, $\Lambda = 30°$ aft. The root and tip of each wing were cut parallel to the angle of the oncoming flow. An attachment shaft with axis parallel to the wing quarter chord line was fitted to each wing root. The resulting wingtip cut was sealed with a flat plate fashioned to match the contour of the airfoil profile. With the sweep modifications, the effective chordlength (c) was measured parallel to the tunnel freestream. The STW chordlength was 6 inches while that of the FSW and ASW was 6.928 inches. The wings were mounted horizontally with the attachment shaft through the side wall of the tunnel. Spacing between the wing root and side wall was approximately 3/8 inch while the wingtip was no closer than 4 inches to the other side wall. The effective span positions studied were across 8 inches in horizontal distance. No data points were taken within 4 inches of any wall and appear from flow visualizations closer to the wall to be well away from the wall effect. The wings were also painted black to reduce reflection and permit flow structure analysis very close to the surface.

A small D.C. motor (1/6 h.p.) permitted variable speed

driving of a scotch yolk that in turn produced a sinusoidal pitching motion of variable amplitude. The motor and scotch yoke were mounted outside the tunnel side wall. Both the driving mechanism and the wing attachment shaft were mounted at the desired sweep angle relative to the tunnel test section wall. The induced wing pitching motion was constant throughout the full length of the wing along an axis running through the quarter chord location. By adjusting the position of the shaft and scotch yoke, the mean angle about which oscillations occurred (α_m) and the oscillation amplitude (α_ω) could be varied. Instantaneous angles of attack (α) for static tests could also be changed from outside the tunnel. A magnetic reed switch was mounted on the flywheel of the motor to record the rotational frequency, ω , and to produce a synchronization pulse when the wing was at maximum angle of attack. This reed switch signal was coupled with an electronic variable delay to trigger data signals at any desired position in the oscillation cycle. Data points could be recorded at desired intervals throughout one complete pitching cycle from nondimensional oscillation phase angles of ϕ = 0.0 to 1.0. In the dynamic tests, the motion histories began at the maximum angle of attack where ϕ = 0.0, and returned to the highest α where ϕ = 1.0.

One data collecting technique employed during investigations on the three wings was flow visualization. This procedure includes the use of a smoke wire to mark the flow about

the surfaces and photography to record the flow patterns. The smoke wire technique produces a vertical sheet of smoke from the top to the bottom of the test section. The smoke is produced by passing a current through an Elgin alloy wire (0.008 inch diameter) which has been coated with equal parts of Rosco theatrical fog fluid and 30W motor oil. The current used to heat the wire was determined empirically to create the ideal density and duration for visualizations. The wire was suspended from top to bottom of the test section and introduced a vertical plane of smoke into the flow approximately 1.5 feet upstream of each wing root. The wire could be positioned to produce the smoke sheet that impinged on the wing surface at any desired span location. Spanwise sites along each wing were measured from the wingtip inboard along the quarter chord line of the wing. This distance was non-dimensionalized by dividing by the chordlength, c, of each wing and is symbolized by S. The light illuminated smoke patterns about the wings were recorded by photographic techniques.

As the smokelines passed over the wing, smoke illumination was provided by a short duration (7 μ sec) focused stroboscopic flash unit positioned about the tunnel to maximize illumination and minimize spurious reflections or diffuse lighting. The flash was triggered by wing phase angle so that each time the wing passed through the same angles of attack, illumination occurred. The resulting multiple (4-6 flashes)

exposure photographs were recorded by a 35mm camera using ASA 400 film. The multiple exposure photographs provided evidence of reliability in the observed flow field structures. To gain an orthogonal perspective, photographs were taken from the side, viewing down the wing span from tip to root, and from the top of the wind tunnel test section. In all photographic visualizations presented in this text, the flow is passing from left to right in the picture.

The initial FSW experiments employed flow visualization techniques for data acquisition. Freestream velocities were set to maintain Re = 30,000 and 40,000. The FSW was initially tested under static (no oscillating) conditions. Static angles of attack tested were α = 3°, 5°, 9°, 12°, 15°, 18°, 21°, 25° and 27°. The smoke wire was positioned to afford smoke passage over three span locations: wingtip, S = 0.58c inboard, and S = 1.15c inboard. By oscillating the wing at frequencies up to 10 Hz, values of nondimensional reduced frequency parameter, $K = \omega c/2V_\infty$, of 0.6, 0.8, 1.0, 1.2, and 1.4 were realized. Mean angles of attack were 12°, 15° or 18° with oscillation amplitudes of ±9° and ±10°.

To make valid comparisons of sweep angle effects, an investigation using the FSW, STW and ASW was performed. As with the FSW tests, static conditions over all three wings were first evaluated across the α range of 3° to 27°. The dynamic tests of the three wings were accomplished using a mean angle of attack of

15° and an oscillation amplitude of ±10°. The reduced frequency values were varied from 0.6, 1.0 to 1.4K. Photographs were prepared for discrete span locations varying from the wingtip, 0.17c, 0.33c, 0.5c, 0.67c, 1.0c to 1.33c inboard. In order to determine the interactive dependencies between wing test dynamics and the time dependencies of flow structure initiation, the whole sinusoidal oscillation period was examined by flow visualization. Photo documentation was done, however, only for those periods in the wing motion that were essential to understanding flow initiation and development. Vortex initiation point, vortex size, spatial time dependent positions, shear layer development and boundary layer growth were measured. These measurements were completed from both side and overhead views. The results were compared for different wing sweep angles at various span locations.

In order to better quantify flow characteristics about the three wings, hot wire anemometry was used to record local velocity magnitudes. These velocity measurements were made using a constant temperature hotwire probe constructed of 10% Rh Pt 0.0001 inch Wollaston wire. The linearized circuit 0 to 5 volt full scale output was preset for maximum anticipated velocity. The data acquisition and reduction were accomplished with a 16 channel DT 1761 Data translation A/D interface and Digital Equipment Corporation LSI 11/23 microprocessor. Data was reduced and then plotted on an Esterline Angus Model 575 x-y plotter.

During the hot wire anemometry tests on the three wings, a Reynold's number of 40,000 was sustained. Reduced frequencies of $K = 0.6$, 1.0 and 1.4 were used to initiate and maintain leading edge vortex structures on the wing surfaces at these low tunnel velocities. To identically match the flow visualization data already accumulated for the three wings, a mean angle of attack of 15° and oscillation amplitude of ±10° were used. Identical wing spanwise locations as the previous flow visualization experiments were investigated. The anemometric measurements were taken at each span location and chordwise at 0.00c(leading edge), 0.17c, 0.33c, 0.50c, 0.67c, 0.83c and 1.00c. An X, Y, and Z coordinate system was established with the origin at the leading edge of each wingtip. The X-axis parallels freestream and wing chordline; Y-axis is perpendicular to freestream in the vertical direction; and, the Z-axis parallels the wing span. The hot wire data were collected at an A/D sampling frequency of 2 KHz. Phase-locked sampling was done for ten runs (over 200 points per run) each consisting of two complete oscillation cycles. The independent trigger pulse signaled $\phi = 0.0$ in each oscillation cycle. The orientation of the hot wire probe was normal to the freestream flow. The hot wire, thus, sensed absolute velocity magnitudes while flow direction was monitored by orthogonal top and side view flow visualizations. The oscillating motion prevented probe locations very near the wing surface. This limitation precluded

comprehensive velocity measurements of small vortical structures and of those located near the wing surface.

The large size of the 1/10 scale reflection-plane model of the X-29 aircraft necessitates the use of the 2 foot by 2 foot test section, low turbulence wind tunnel. The freestream tunnel velocity was set using a reference pitot tube in the test section. Throughout the X-29 model tests, the velocity was maintained at 25 feet per second. One side wall with splitter plate supported the model while the opposite wall was fitted with glass to permit flow visualizations. The top and bottom walls as well as the model and splitter plate were painted black to reduce reflections and enhance flow structure clarity. The visualization smoke was introduced into the flow by a smoke rake located in the plenum chamber. This technique provided a vertical plane of smoke lines through the test section spaced approximately one inch apart. The model was positioned in the tunnel so the plane of smoke impinged the canard at the midspan location. A limitation of the smoke system is the vertical distance between the smoke lines. Under certain test conditions, the streaklines at critical locations would not be as visible as desired due to the spatial gap between the lines. This adverse characteristic could be eliminated by employing a smoke wire.

The X-29 reflection-plane model is mounted to a splitter plate which extends from top to bottom of the test section. The model can be rotated about a point near the center of gravity to

change the angle of attack (AOA) of the entire model. A small D.C. motor and scotch yoke are mounted outside the tunnel and are affixed to the canard attachment shaft. This assembly induces sinusoidal canard pitching motions of variable frequency and amplitude. Flow visualization photography with 35mm camera and stroboscopic illumination record the flow patterns during both static and dynamic (oscillating canard) tests. Photographic procedures were adjusted to capture the flow patterns about both the canard and the wing. To record pertinent three-dimensional flow data, photographs were taken from both side and rear view perspectives.

Much like the previous finite wing tests, the X-29 investigations began with static experiments. The model AOA was set at 0°, 5° and 10° while the canard was varied in 5° increments between 0° and 40°. The canard angle of attack, α , was always measured with respect to the model centerline. The dynamic tests included parameter variations in the canard mean angle of attack of 0°, 5° and 10° and oscillation amplitude of ±5°, ±10° and ±20°. Model AOA values of 0°, 5° and 10° were also used during dynamic tests.

The systematic data collection methods and techniques described above have produced a reasonable data base from which to extrapolate and compare flow characteristics about three-dimensional surfaces. Limitations to each of the techniques have been discussed and were considered when data reduction and

analysis was accomplished. Every experimental investigation produced unique results and each are discussed separately in the sections that follow.

CHAPTER IV

FORWARD SWEPT WING

Three-dimensional swept wings are utilized on all high performance aircraft, therefore, an appropriate beginning toward application of unsteady aerodynamics is to investigate sweep effects. Much has been accomplished and documented on two-dimensional unsteady airflow. However, aircraft have finite wings. Any applicable unsteady flow producing mechanisms must be preceded by basic understanding of complex, three-dimensional unsteady flow characteristics. To date, the sweep effects of airfoils and delta wings have received only minor attention in regard to unsteady flows. This analysis focuses upon the three-dimensional characteristics of unsteady flows produced about a swept forward wing tested under a variety of dynamic pitching conditions. The complexity of flows known to be produced by lifting surfaces pitching sinusoidally beyond static stall angles dictates the initial use of flow visualization.

Static Tests

As a basis for dynamic comparisons, the swept forward wing was first examined using flow visualization across a wide range of static angles of attack. To characterize the spanwise

perturbation of the resulting flow fields, smoke was allowed to pass over three locations: wingtip, 0.58c inboard and 1.15c inboard. The flow was photographed from the sideview (tip to root) and from above. In all instances, the photographs used multiple exposure, stroboscopic illumination that assured flow field reproducibility. Angles of attack were varied from 3 to 27 degrees.

The adherence of the smoke to the contour of the upper surface of the wing was dependent upon the spanwise site visualized. Failure of the smokeline to follow the wing contour was used as evidence of flow separation. At about 3° alpha, flow remained attached at all locations on the wing visualized (Fig. 1,Aa). At a static angle of attack of 9°, the most inboard span location visualized (1.15c) began to show indications of flow separation (Fig. 1,b) in contrast to the immediately outboard location (0.58c) where the flow remained attached (Fig. 1,B). When the angle of attack was increased to 15°, above stall for this airfoil, the flow was fully separated inboard and only beginning to separate nearer the wingtip (Fig. 1,Cc). Further increases in the angle of attack (Fig. 1,Dd and 1,Ee) result in more dramatic separations of the flow field from the wing. In all of the visualizations, the separation is less fully developed near the wingtip than it is at more inboard locations.

The flow field visualized at the wingtip was dominated by the presence of a strong helical flow around the tip (Fig. 2,Aa).

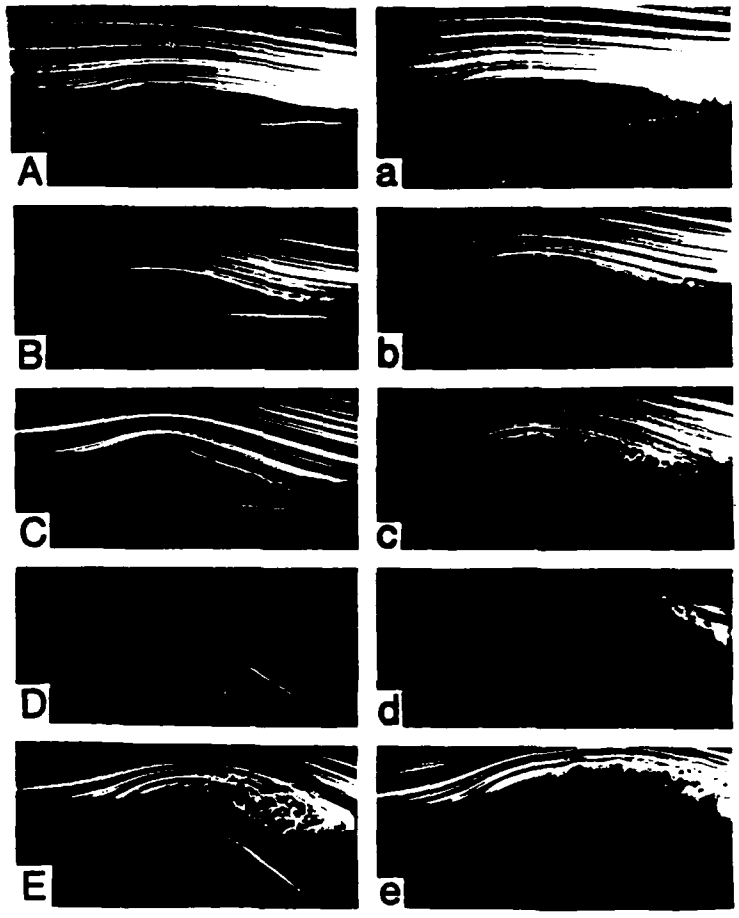

Fig. 1 Spanwise separation on static wing, Re = 40,000, A-E: span location S = 0.58c, a-e: span location S = 1.15c, Aa - Ee: α = 3°, 9°, 15°, 21°, and 27°, respectively.

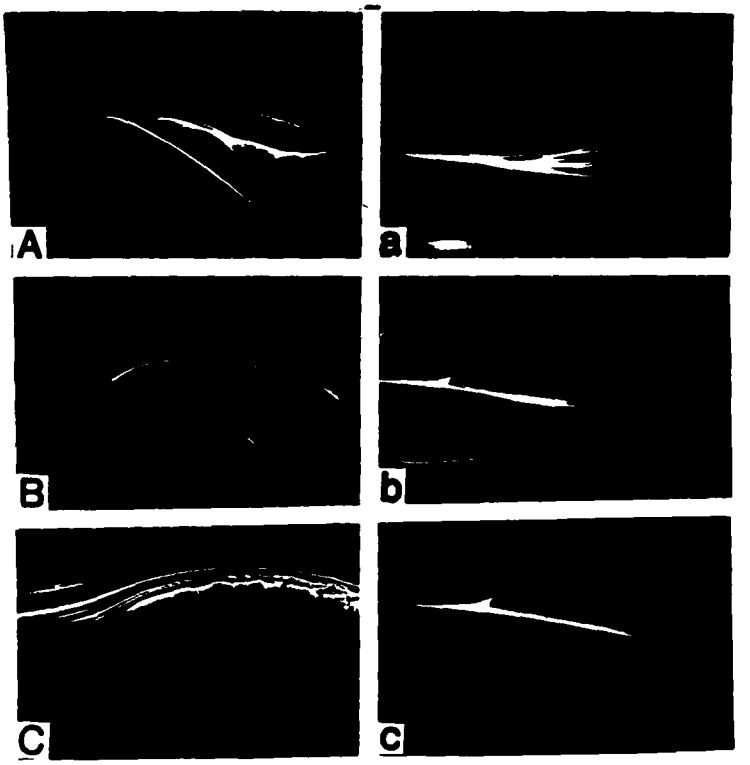

Fig. 2 Spanwise flow displacement on static wing, Re = 40,000, α = 27°, A-C: side view, a-c: top view, Aa: wingtip, Bb: S = 0.58c, Cc: S = 1.15c.

To quantify the relative apparent strength of the wingtip vortex, a spanwise flow angle β was measured at the tip of the wing. The top schematic in Fig. 3 graphically depicts the measurement of this angle. Top view photographs show the initial chordwise crossing of the smoke sheet from the pressure to the suction side of the wing. A line tangent to the flow is drawn at the point where the smoke initially crosses the plane of the wingtip. The angle β is measured from this tangent line to the plane of the wingtip. Across the static angles of attack tested, increased values were associated with ever tighter helical bending of the smoke around the wingtip. This tightening of the helical flow is formalized in Fig. 3 with the β angle. As can be seen, the positive correlation between the α and β angle persists across all tests and the β angle flattens only at angles of attack associated with inboard flow separation.

When seen from above (Fig. 2), spanwise displacements of the flow are most obvious near the wingtip. The smoke from the upstream smokewire intercepts the wingtip in a manner that pulls the underside flow outward around the tip and then inward over the upper wing surface. The upper surface flow appears to be spatially influenced by the wingtip vortex at nearly all span locations. At the midspan location (Fig. 2b), the flow near the wing surface is pulled toward the tip by the strong helical tip vortex. At tested span locations further inboard, the wingtip effect still seems to draw the flow in the direction of the

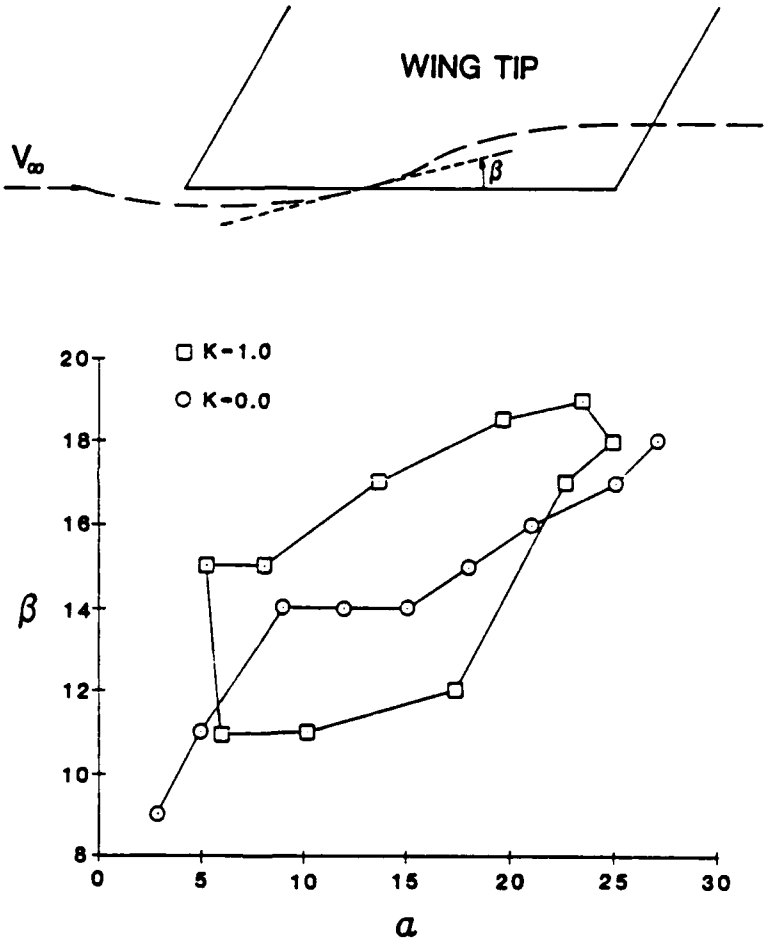

Fig. 3 Tip deflection angle for static and dynamic wing, Re = 40,000, $\alpha_m = 15°$, $\alpha_\omega = \pm 10°$.

unstalled tip.

Dynamic Tests

Using multiple exposure, phase-locked photography, the flow field was visualized for the swept forward wing for a variety of K values, mean angles and spanwise locations. Photographs taken stroboscopically at different angles of attack throughout the oscillation cycle produced a record of the resulting flow field. Inevitably, the test conditions yielded vortex dominated flows that varied temporally and spatially both in initiation and development. These variations exhausted the full freedom of the three-dimensional analyses used. Resulting visualizations exhibited considerable reliability, in that the multiple exposures revealed consistently superimposed smoke lines despite the complexity of the elicited flows. This level of reproducibility was clear from both the side and top view visualizations.

Inboard span location. At S = 1.15c, the span location far inboard from the wingtip, the sinusoidal pitching motions of the wing elicited flow field structures similar to those previously reported for airfoils and flat plates as well as for inboard sites on a straight symmetrical wing. A leading edge vortex was produced as the wing pitched upward through the static stall angle. First appearing in the 0.0 to 0.2 chord location, the vortex grows in apparent size and then begins to convect

toward the trailing edge of the airfoil. As the vortex passed into the wake, only a small amount of evidence of a trailing edge vortex appeared.

Across the test conditions used in these studies, the vortex initiation occurred earlier in the upward pitching motion if the mean angle of attack was increased. When K values were increased, vortex initiation was altered. Also, increased K values yielded higher overall convecting velocities for the passage of the leading edge vortex over the upper airfoil surface and yielded smaller, apparently more cohesive vortex structures. All of these correlates between flow field structure and pitching dynamics are quite similar to those reported earlier by authors of two-dimensional literature. Accordingly, vortex initiation using 18±9° occurred at 15° on the upstroke but using 12±9° occurred at 17°. As noted before, earlier vortex initiation was associated with slower average convecting velocities and later initiation was associated with higher convecting velocities. Average convecting velocities tended to mask the fact that earlier initiation yields convection histories characterized by initially slow convection and more rapid acceleration whereas later initiation shows initially modest convection without later acceleration of the vortex to the trailing edge.

Wingtip location. The wingtip flow about the swept forward wing varied in substantial ways from that observed using a straight symmetrical wing. By characterizing the bending of

the smokelines around the wingtip to the upper surface of the wing, β angle, it was possible to quantify the relative characteristics of the wingtip flow throughout a full pitching cycle. A comparison of the β angle of tip flow is provided in Fig. 3, for both static tests conducted across a variety of angles of attack and for dynamic tests conducted across pitching motions that moved the wing through the same angles. The dynamic test conditions were $\alpha = 15 \pm 10°$ with a K value of 1.0. The relatively linear relation between β and static angles of attack is displayed and the hysteresis loop of β with dynamic angles of attack is also shown. In the latter case, the β angle is small through early stages of the wing upstroke but then increases rapidly through the later stages of the upward pitching motion. Near the top of the pitching cycle where $\alpha = 25°$, the associated β angle is greater than that observed during the static tests at the same angle of attack. The β angles remain larger than those observed for static test counterparts through the downstroke. At the end of the pitching downstroke and the beginning of the upstroke, the wingtip flow is characterized by rapidly decreasing β angle. Once again, the β angle remains small until the midpoint of the upstroke is attained.

This dynamic time history of the wingtip flow correlates well with the inboard initiation, development and convection of the leading edge vortex (Fig. 4). As β angle

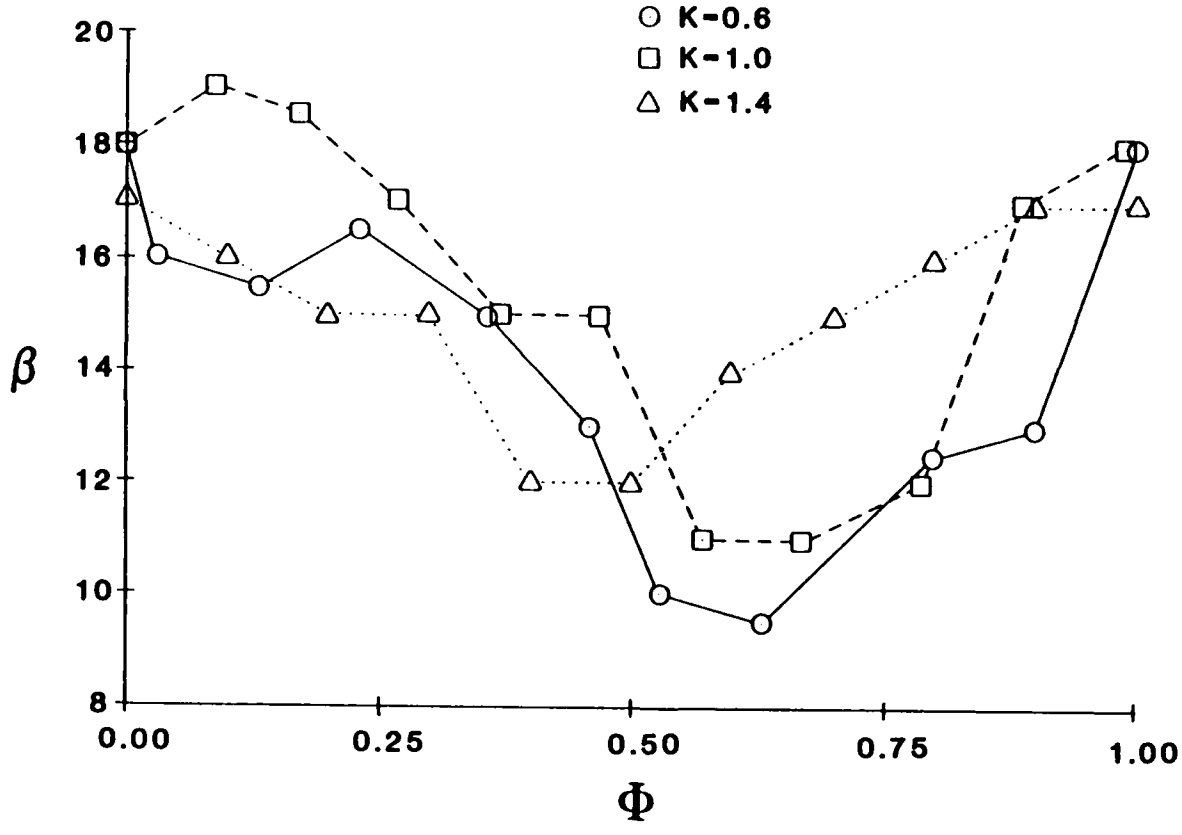

Fig. 4 Tip deflection angles for various K values, Re = 40,000, $\alpha_m = 15°$, $\alpha_\omega = \pm 10°$.

appears to increase dramatically on the upstroke of the wing, the leading edge vortex is growing over about 0.2c inboard. When the β angle is the largest, the vortex has attained mature size and is beginning to convect over the wing surface. The β angle remains elevated over that seen in static tests as long as the leading edge vortex remains over the upper surface of the wing. When the leading edge vortex sheds into the wake of the wing, the β angle drops precipitously to a value smaller than that shown for static tests at the same angle of attack.

Tip vortex flow appears to respond in a systematic manner to alterations in the K values. In the tests that employed $K = 0.6$, the β angles remain low during the wing upstroke until near the maximum angle of attack. Then, the angle of the wingtip flow increases to β values above static test values. The increased β values decrease rapidly but remain at levels higher than the static counterparts through most of the wing downstroke. Notably, the β angles at the lowest angles of attack were quite small at the transition to wing upstroke. These values remain lower than static counterparts throughout much of the upstroke. In contrast, the $K = 1.4$ tests resulted in β values that were routinely higher than static counterparts throughout almost all of the oscillation cycle. The rapid changes in β angles characteristic of tests done with $K = 1.0$ and $K = 0.6$ were absent in the flattened hysteresis loop for the β angles recorded using K =

1.4. It is tempting to relate these observations to the fact that a vortex is present over the inboard surface of the wing at all times when a K = 1.4.

Midspan locations. Using the above flow field characteristics as reference points, the flow over the wing between these tip and inboard sites was evaluated. The smoke wire was moved spanwise such that the smoke lines intercepted the wing at points 0.29c, 0.58c and 0.87c inboard of the wingtip. Again, multiple exposure photographs were taken both from the side and from above the wing. Fig. 5, provides sideview comparisons of flow over some of these spanwise locations for both static and oscillating (K = 1.0) wing test conditions where the angle of attack is either constant or instantaneous 18°, respectively. A major difference in the apparent amounts of flow separation is clearly shown for the static as compared to the dynamic test conditions. And, the separation is quite sensitive to spanwise location. Fig. 5 shows a definite separation of the flow from the wing surface in the static tests (B and C) but an attached vortex-initiation flow in the dynamic tests (b and c). At the wingtip, a strong vortex is evident in both test cases (Fig. 5A and 5a) and no evidence of flow separation appears. Farther inboard, the flow separation in the static case is preceded upstream about the leading edge of the wing by turbulence whereas in the dynamic

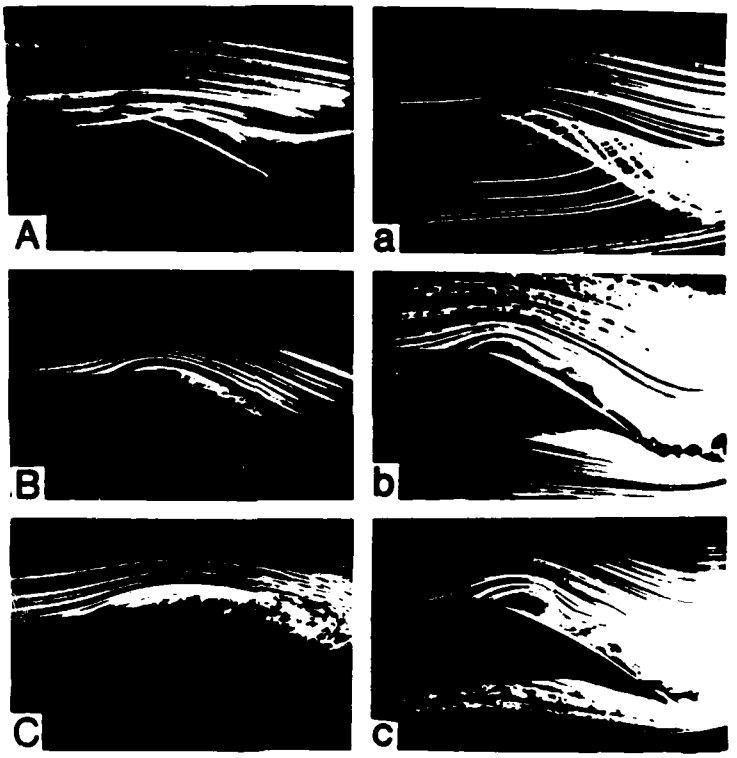

Fig. 5 Side views of static and dynamic wings, Re = 40,000, A-C: static wing, K = 0.0, α = 18°, a-c: dynamic wing, K = 1.0, α = 18°, Aa-Cc: wingtip, S = 0.58c and S = 1.15c, respectively.

case the same site shows the presence of a highly structured vortex (Fig. 5C and 5c).

When the same test conditions are visualized from above the wing it is possible to characterize the spanwise deflections of the flow field. Although the spanwise deviations in flow are often complex, an average was obtained by measuring the smoke line displacements at the trailing edge of the wing from the initial plane of smoke introduction upstream of the leading edge. In this way it was possible to evaluate the spanwise flow of both the upper and lower surface smoke lines. The resulting measures were collected and summarized for each set of test conditions. These summaries were helpful in interpreting the data reported here, but will not be formally presented.

The apparent size of the leading edge vortex, SZ, is measured (in cm.) from the wing surface to the top of the vortical structureand has been previously reported in two-dimensional studies to be inversely related to the magnitude of the K value. In tests with the swept forward wing, this relationship appears to be strongly related to the spanwise site of the observations (Fig. 6). At S = 1.15c the vortex size is inversely related to K value. At S = 0.87c the vortex size changes very little with alterations in K value. And at S = 0.58c or S = 0.29c, the vortex size actually increases with increasing K values. At these sites closer to the wingtip

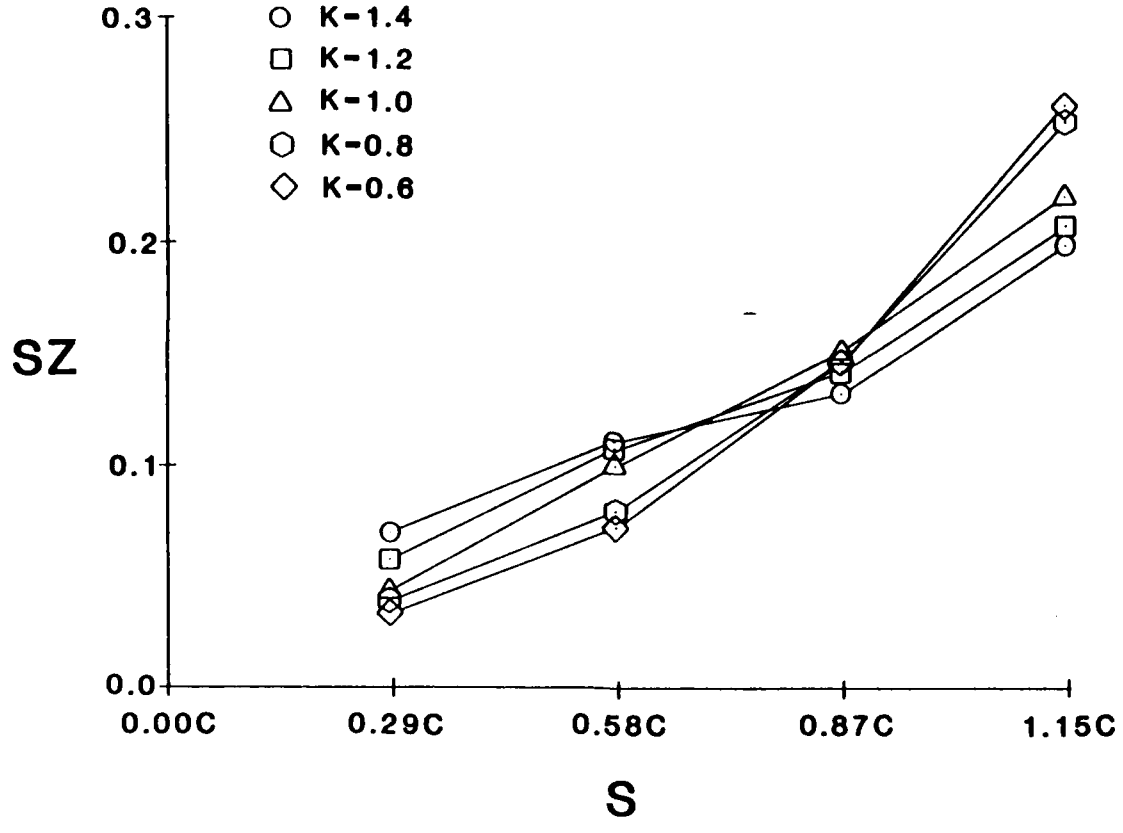

Fig. 6 Leading edge vortex size, Re = 40,000, $\alpha_m = 15°$, $\alpha_\omega = \pm 10°$.

the vortex forms and grows near the leading edge but then the vortex structure dissipates as it begins to move toward the trailing edge of the wing. Despite these variations in growth dynamics related to K values, it remains clear that the leading edge vortices are very much smaller near the wingtip than at inboard locations on the span.

The convection velocities, V_c, were calculated as average values for the time of vortex appearance near the leading edge to the time of shedding from the trailing edge. Or, it was calculated from the time of appearance to the time of structure dissipation. This method includes both the initiation and formation times for the vortex, times when the vortex appears not to move over the surface of the wing. In all cases, the vortex was observed to convect slowly over the leading portions of the chord and more rapidly over the downstream chord locations. The influence of span location on V_c is summarized in Fig. 7. The progressive acceleration of the vortices for different span locations is summarized across the chord (X/C) of the wing throughout an oscillation cycle in Fig. 8. Regardless of span location, increases in K were associated with higher V_c values. And, the more inboard locations on the span also were associated with higher V_c's. To better summarize these observations, the positions of the vortices over the wing are plotted on the wing planform for different portions of the pitching cycle, 0.0, 0.25 and 0.50, in Fig. 9.

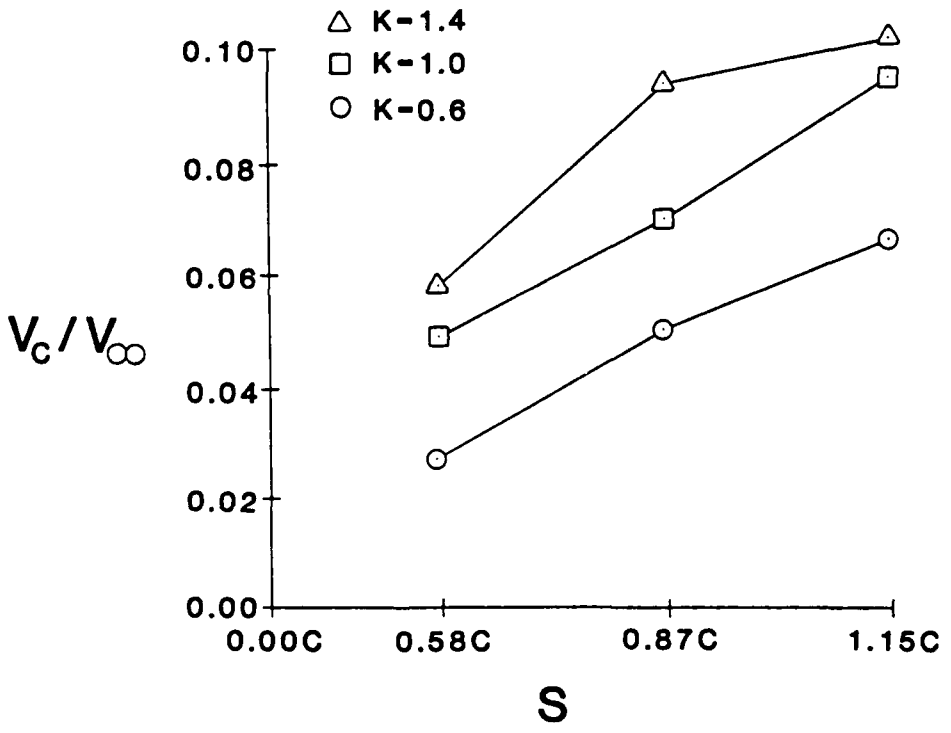

Fig. 7 Convective velocities, Re = 40,000, $\alpha_m = 10°$.

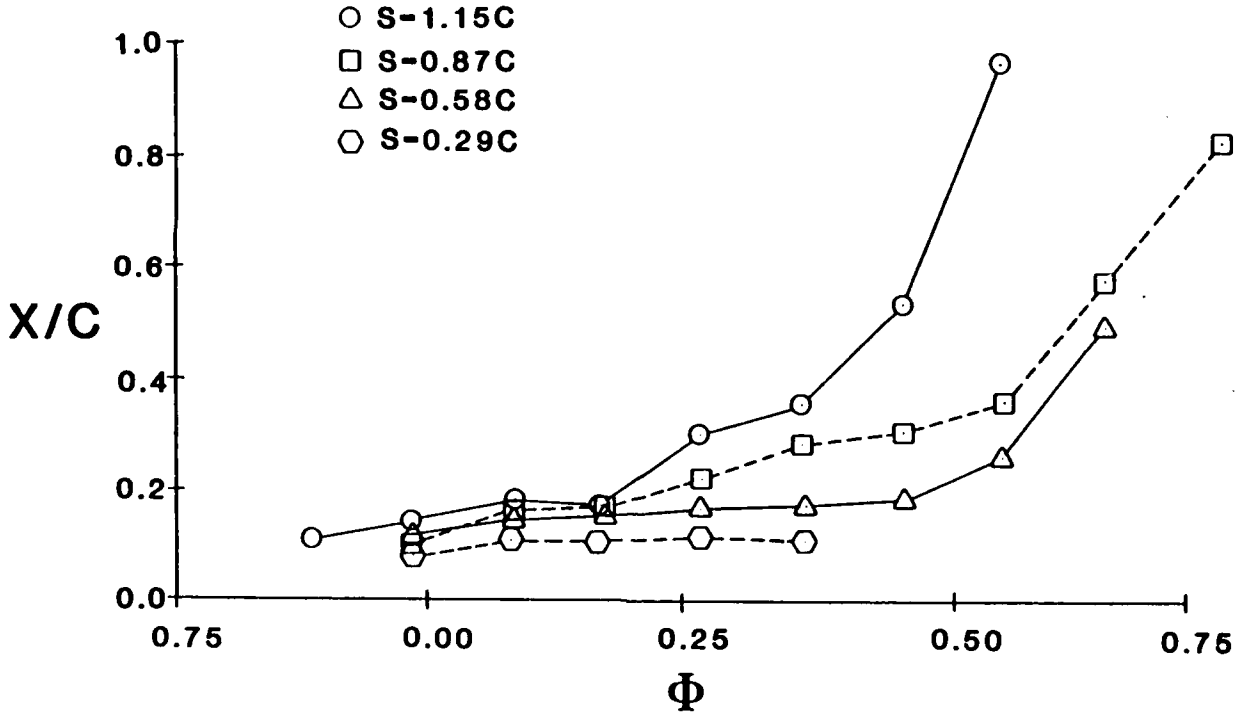

Fig. 8 Leading edge vortex position along the chordlength, Re = 40,000, K = 1.0, $\alpha_m = 15°$, $\alpha_\omega = \pm 10°$.

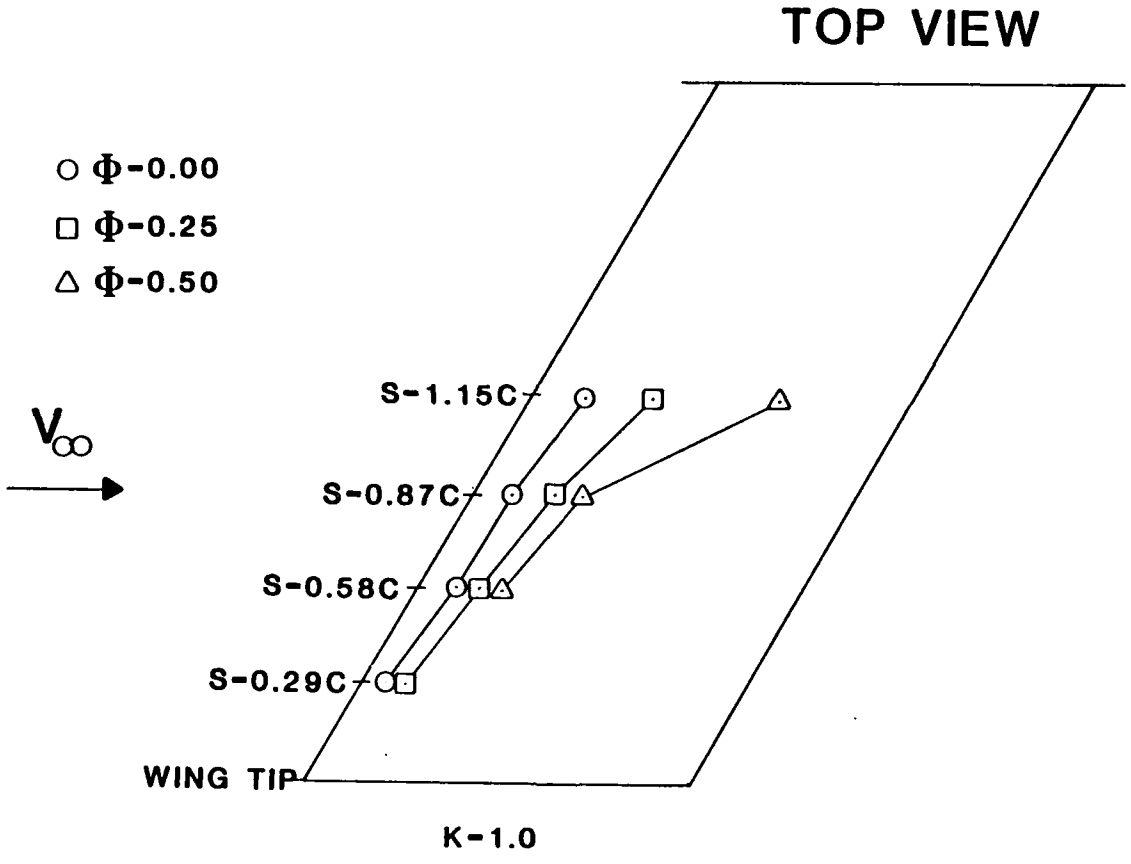

Fig.9 Planform leading edge vortex position, Re = 40,000, K = 1.0, α_m = 15°, α_ω = ±10°, ϕ = 0.0: α = 25°, ϕ = 0.5: α = 5°.

The mean angles of attack around which the sinusoidal motions of the wing were driven were varied between 12°, 15° and 18° using motions of ±9° and ±10°. The leading edge vortex formation occurred earlier in the upward pitching motion when the mean angle of attack was increased (Fig. 10) and when the observation site was S = 1.15c. At a span location closer to the tip (S = 0.58c), the initiation of vortices was delayed until later in the upward pitching motion cycle. But, the higher mean angles of attack led to more delay in the vortex initiation. In this instance it appeared that the effect of the mean angle of attack on tip vortex flow was greater than it was on inboard flow; thus the inboard flow was clearly influenced by high angle of attack strengthening of wingtip flow. Coupled to the differences in vortex initiation, the overall V_c was lower for lower mean angles of attack. As may be seen in Fig. 11, the low V_c values derive from earlier vortex initiation with high angles of attack. It is equally clear that higher mean angles eventually produce greater vortex convection than lower angles when the whole oscillation cycle is considered. Inboard (S = 1.15c) vortices traveled faster and further than outboard (S = 0.58c) vortices as indicated by the planform plots of Fig. 12. These observations are not to be confused with the initiation phenomena presented above.

One manner for comparing the interaction between the tip and inboard flow patterns elicited on the pitching wing is to

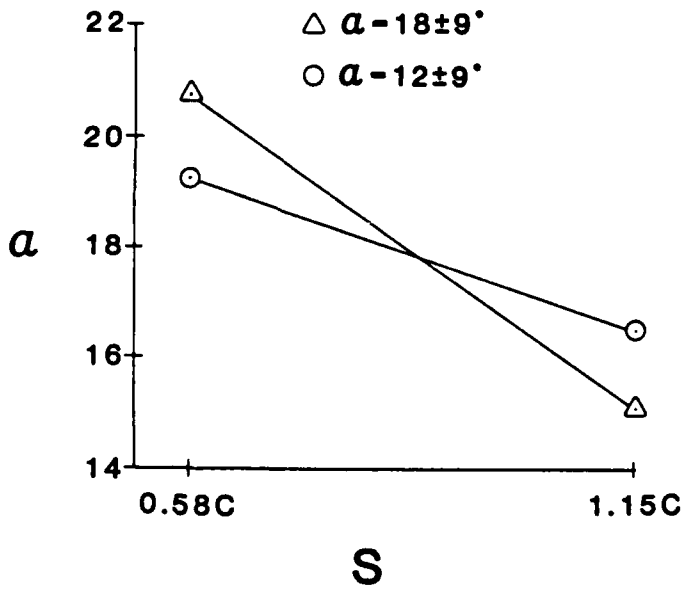

Fig. 10 Leading edge vortex initiation point, Re = 40,000, K = 1.0, α_m = 12° and 18°, α_ω = ±9°.

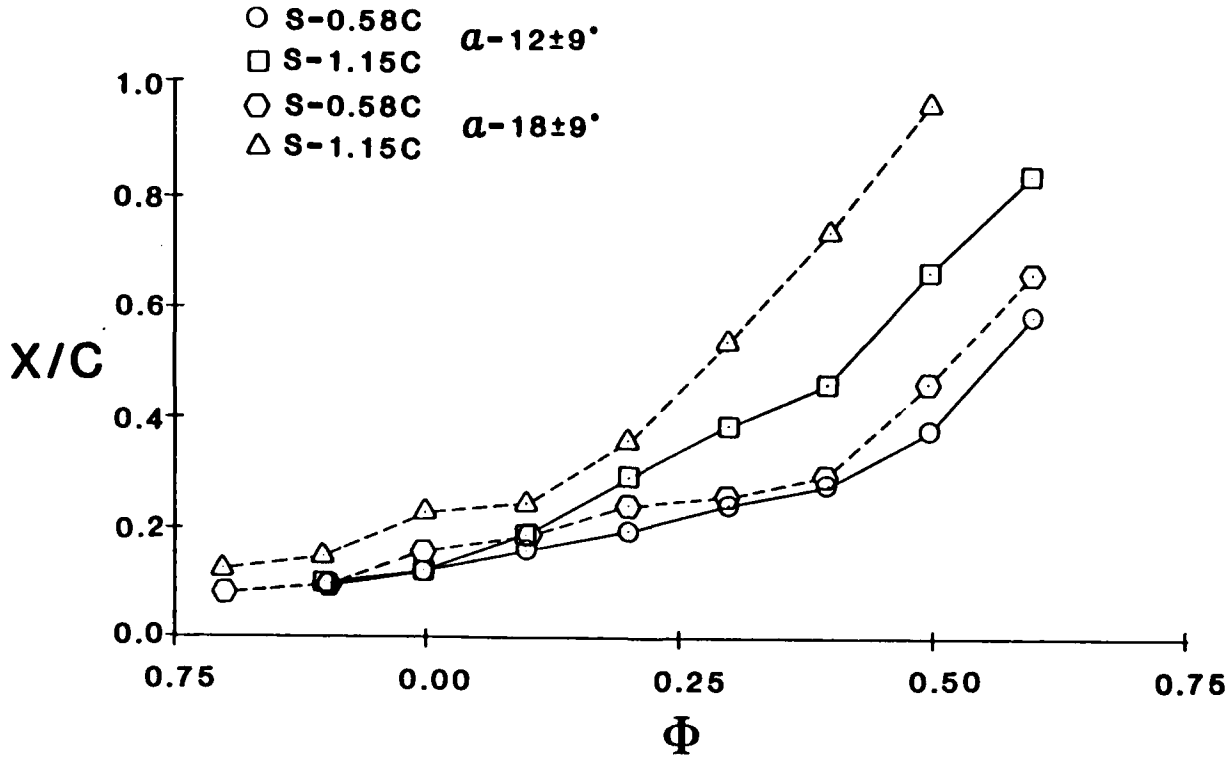

Fig. 11 Leading edge vortex position, Re = 40,000, K = 1.0, α_m = 12° and 18°, α_ω = ±9°.

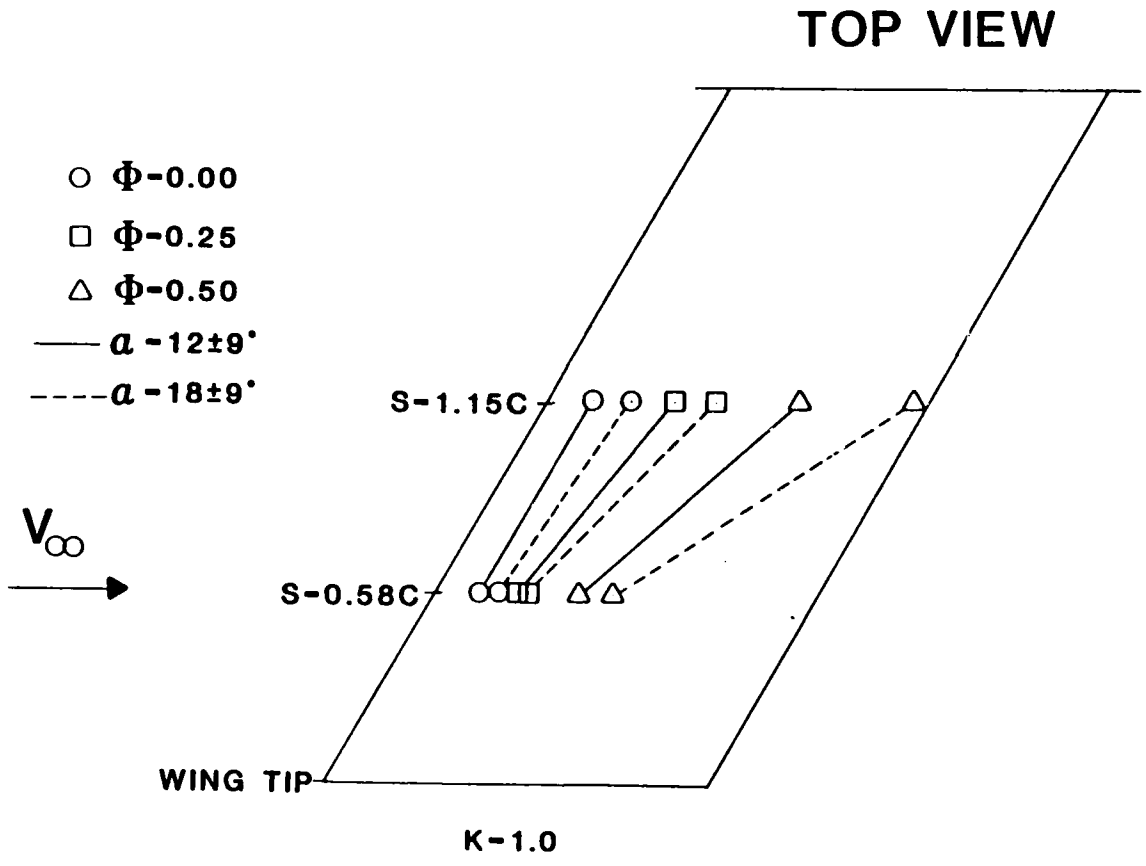

Fig. 12 Planform leading edge vortex position, Re = 40,000, K = 1.0, α_m = 12° and 18°, α_ω = ±9°.

compare signature characteristics of each across a full oscillation cycle. The data presented in Fig. 13, show a comparison between the β angle of wingtip flow with vortex size, SZ, measured at S = 0.29c inboard. When the vortex is apparent inboard, the tip β angle is large. When the inboard vortex has dissipated, the β angle is at minimum value. Variations between these extremes show a very high correlation between changes in β angle and changes in vortex size across the whole oscillation cycle. In these studies no causal relationship was tested but it appears clear that such relations deserve further attention.

Multiple Vortices and Flow Elaboration. Two leading edge vortices were always observed during certain test conditions and at specific sites on the wing (Fig. 5). Other flow structures such as the appearance of another vortex and the appearance of an apparent shear layer were also reliably observed. The two vortices that were produced during a single upward pitching motion are shown in Fig. 14. They appear one after the other in time and chord location. The main vortex forms in the usual fashion on the upstroke with the secondary vortex appearing slightly later and slightly downstream. The secondary vortex is only half or two-thirds the apparent size of the primary vortex but has the same rotational sense. The secondary vortex, formed downstream, convects more rapidly toward the trailing edge of the wing than the primary vortex.

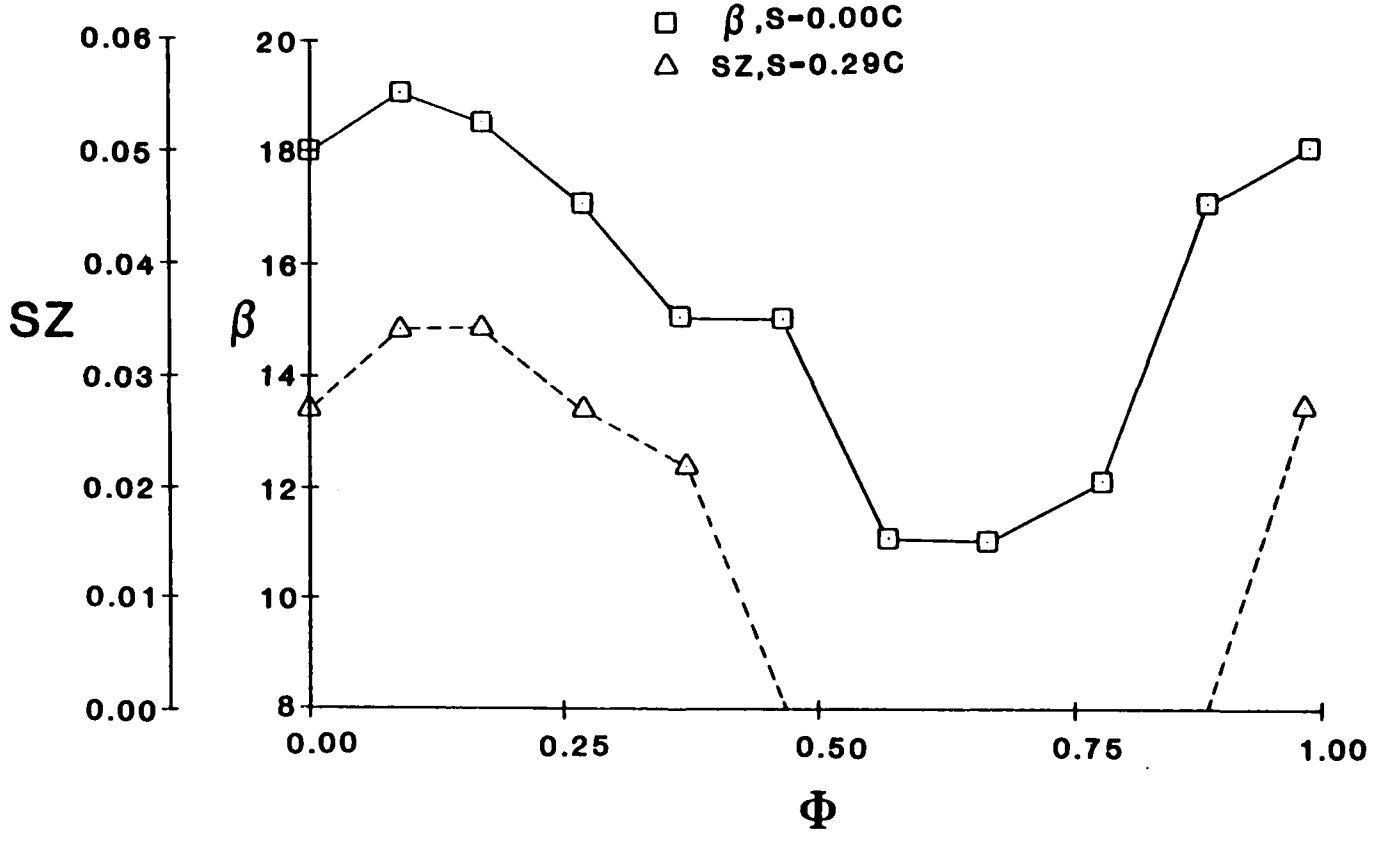

Fig. 13 Wingtip deflection angle and leading edge vortex size comparison, β at S = 0.0, SZ at S = 0.29c, Re = 40,000, K = 1.0, $\alpha_m = 15°$, $\alpha_\omega = \pm 10°$.

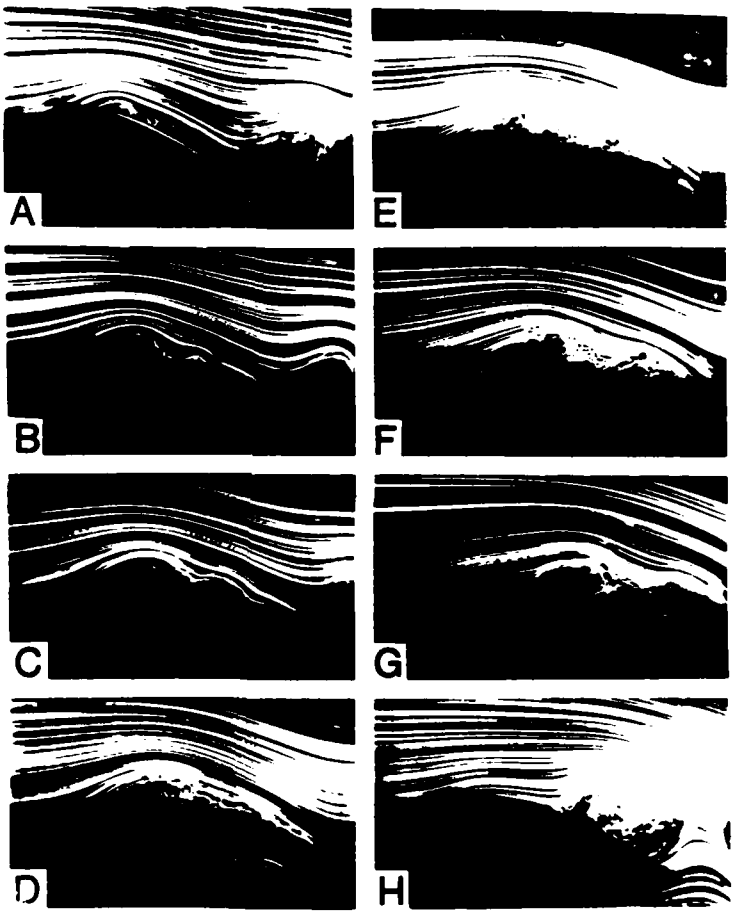

Fig. 14 Progression of second vortical structure,Re = 30,000, K = 1.5, S = 1.15c, A-H: α = 25°, 23°, 18°, 12°, 7°, 5°, 7° and 12° respectively.

Thus, the two vortices appear to pull apart once they have formed. Consistent with previously described flow behavior, the tandem vortices were only seen briefly over the upstream chord locations at S = 0.58c. As may be seen in Fig. 15B and 15C, the shedding of the second vortex coincides with the appearance of a tertiary vortex upstream of the primary structure. This third vortex appears to rotate with the same sign as both the primary and second vortices. If this vortex appeared, it traversed the whole chord of the wing immediately ahead of the primary vortex. Further toward the tip, a variety of other structures appeared quite transiently and shear layer flows appeared to be in evidence.

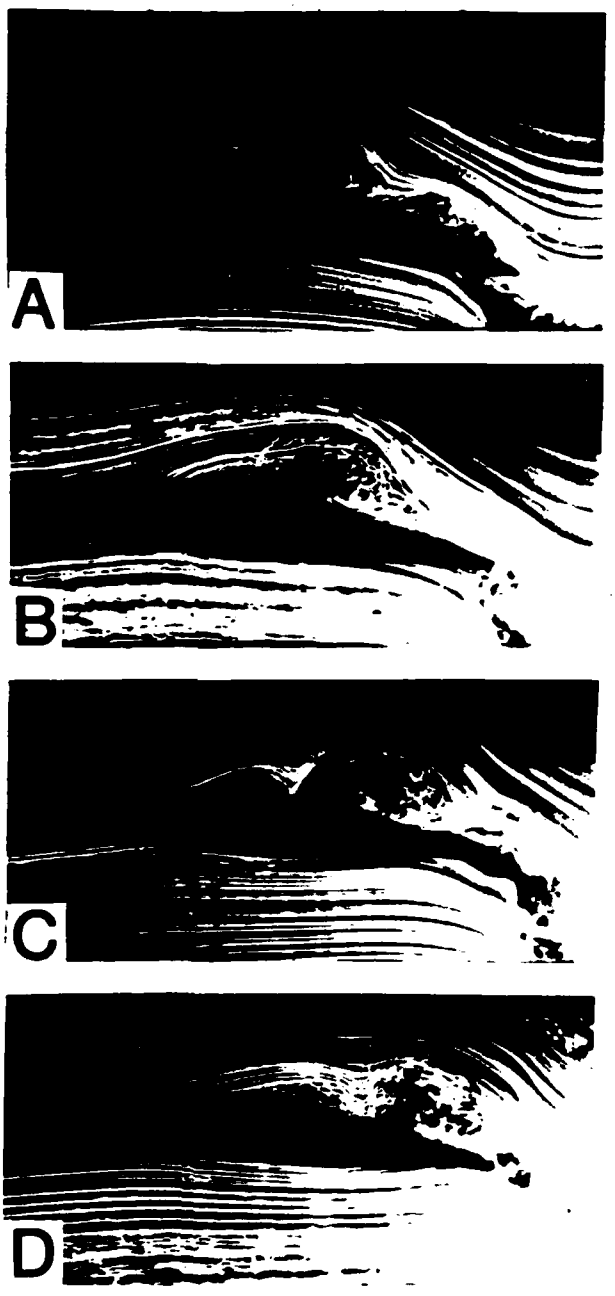

Fig. 15 Formation of third leading edge vortex, Re = 40,000, K = 1.2, S = 1.15c, A-D: α = 12°, 7°, 5° and 7°, respectively.

CHAPTER V

VISUALIZED SWEEP EFFECTS

In previous studies, the detailed impact of comparative sweep angles remains unclear. Yet, the existing research suggests that the sweep angle has a profound effect on both the genesis and development of unsteady flows elicited by various pitching motions. The present study focuses on wing sweep effects using three test wings that varied only in sweep angle: forward, straight and aft swept. Identical test conditions were used both in the static and pitching evaluations. Using multiple phase-locked photographic exposures, the evolving flow fields were examined both in side view and from above with smoke delivered to a variety of span locations.

Static Comparisons

Comparisons between straight and swept wings reveal very different spanwise flow separation characteristics. To visualize these differences and provide a basis for dynamic comparisons, the smoke sheet was introduced into the flow field to intercept each of the wings at three spanwise locations; wingtip, 0.67c and 1.33c. For each spanwise observation, angles of attack were varied from 3 to 27 degrees. The flow field

was photographed from sideview (tip to root) and from above.

A sideview comparison at $\alpha = 15°$ is shown in Fig. 16. The left column for the FSW indicates a strong helical wingtip vortical structure at S = 0.00c, while the beginning of a separation layer is evident at S = 0.67c, and a fully separated flow is present at S = 1.33c. The STW, center column, also indicates a wingtip vortex at the tip, however, both inboard locations are fully stalled. The right column, ASW, shows stall characteristics along the span that are the reverse of those shown by the FSW. The wingtip flow for the ASW does not roll into the clear helical wingtip pattern shown by other wings. On the ASW, the tip flow seems to be influenced by a stalled condition very near this tip location. Inboard spanwise visualizations indicate a fully separated flow region at S = 0.67c and a less aggravated stall pattern at S = 1.33c. These static stall characteristics are consistent with previous studies and theory.

Top view photographs of the wingtip flow are shown in Fig. 17, for the three wing configurations at $\alpha = 27°$. The helical wingtip flow is visualized by the bending of the smoke sheet about the tip. Different comparative magnitudes of β can be seen with maximum β values observed for the FSW. The chordwise location of the flow passing around the wingtip varies not only for each wing at $\alpha = 27°$ but also for the same wing when visualized at different phases in the oscillation

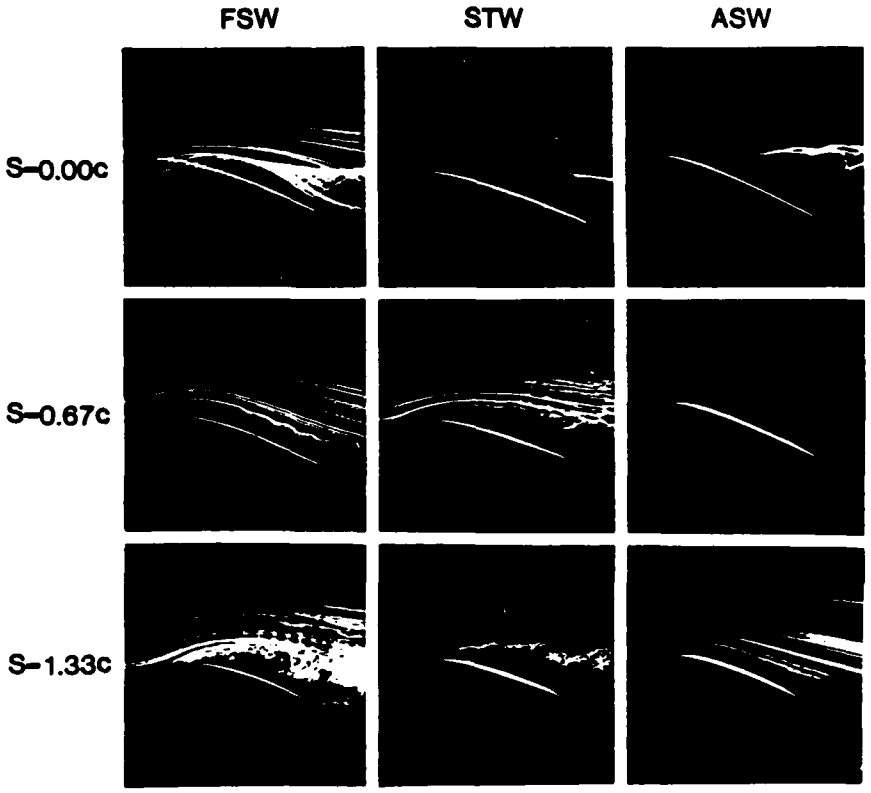

Fig. 16 Sideview static stall comparison, $\alpha = 15°$.

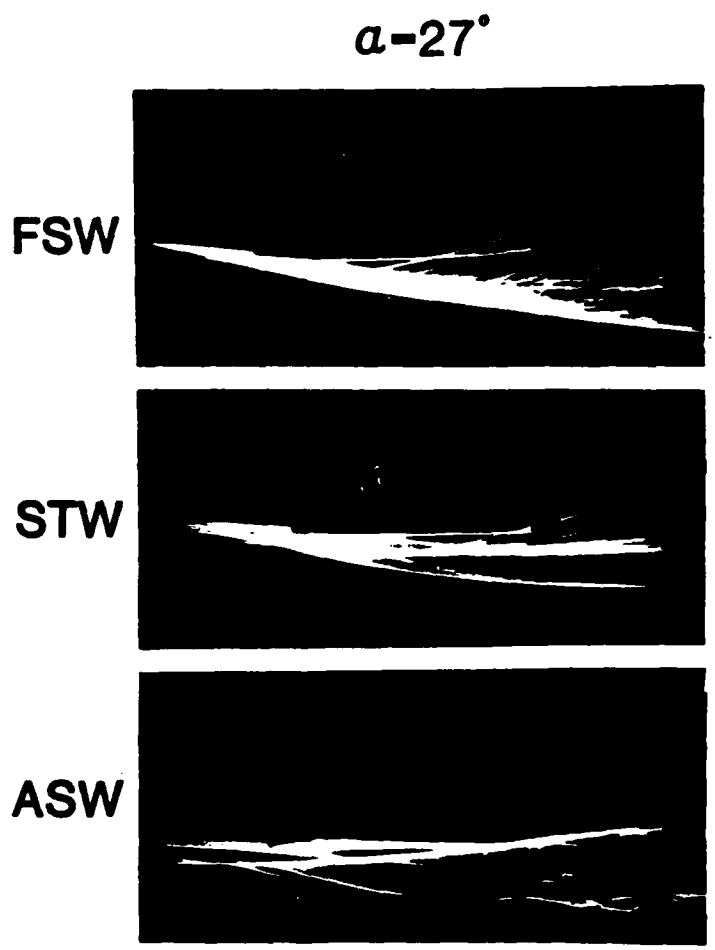

Fig. 17 Topview static β comparison, α = 27°.

cycle.

The spanwise flow deflection at the wingtip, β, is plotted for the three wing configurations over an α range from 3° to 27° (Fig. 18). Specific patterns of β variations occur throughout increments for each wing. For the FSW, β increases with increased α throughout the α range. The β values of the STW, however, initially increase with increasing α then remain constant between α= 9° to 15° (near static stall angle for this airfoil section) and finally decrease with increased α. The β values for the ASW increase with α up to α = 9° then steadily decrease as α is increased. The highest magnitude of the ASW β value does not reach the level of values recorded for either the FSW or STW.

Dynamic Comparisons

Wingtip flow. When the test wings were forced into sinusoidal pitching motions, the flow field about the wingtip remained dominated by the strong wingtip vortex. A comparison of the observed inboard deflection angles of tip flows for each wing is provided in Fig. 19, where K = 1.0. In all cases, when the wings pitch upward, β values increase to a maximum level near maximum angles of attack. The β values then persist above those for static α tests until the lowest angles of attack are attained. Rapid decreases in β values are observed when the wing pitches to minimum angles of attack. Minimum β values occur in all tests at approximately α = 12° during the

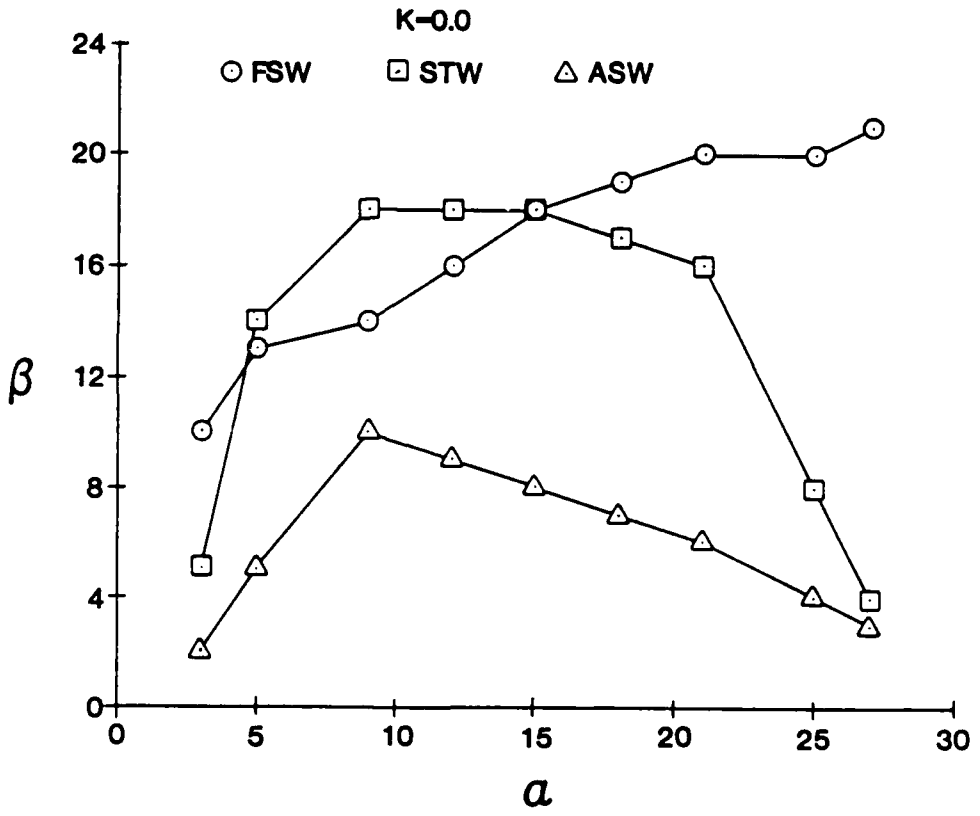

Fig. 18 Static β comparison.

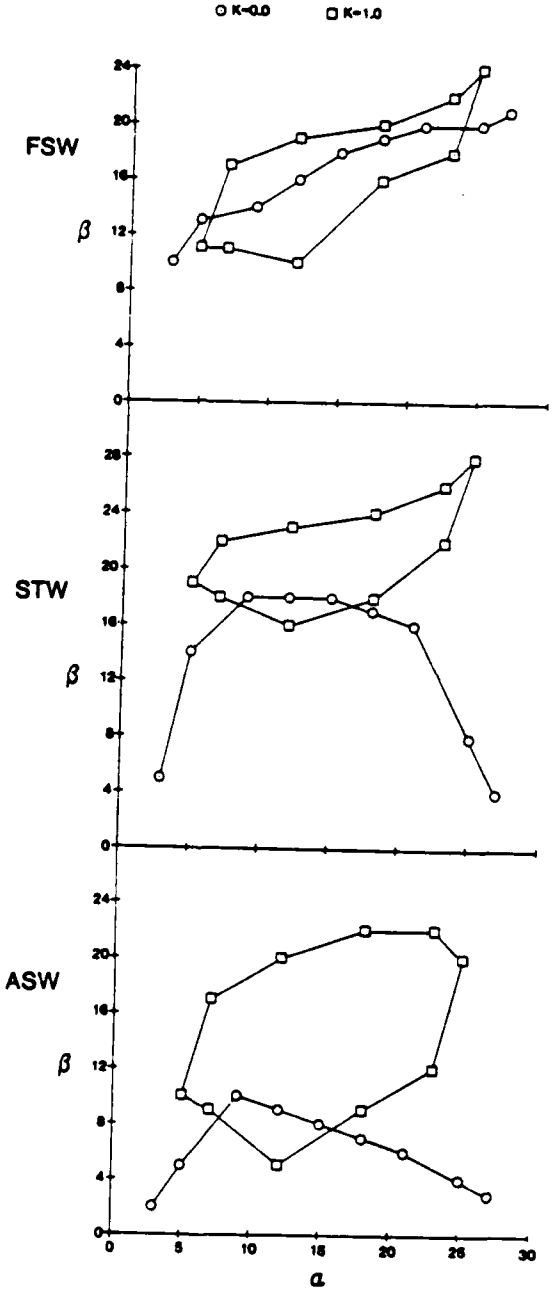

Fig. 19 Dynamic to static β comparisons, K = 0.0 and 1.0.

upstroke of the pitching cycles. The hysteresis loop of dynamic data collected for the FSW is centered about the static α measurements. In contrast, both average STW and ASW hysteresis loops show β values that are consistently above those measured in comparable α, non-pitching cases. The highest average magnitude of β was recorded for the STW. The pitching ASW showed a hysteresis loop for β values that contained the widest excursions between those occurring during the downstroke and those of the upstroke of the pitching cycle. An increase in K value during all wingtip observations produced downstroke and upstroke β values that formed more closed hysteresis loops.

Leading edge vortex on the wing surface. Direct comparisons between the different wing configurations in the initiation of leading edge vortices were achieved using visualizations based on smoke sheets introduced at span locations of S = 0.00, 0.17, 0.33, 0.50, 0.67, 1.00 and 1.33c. Ten sideview, multiple exposure photographs were prepared representing equal time increments throughout the oscillation cycles for K = 0.6, 1.0 and 1.4. Where and when a leading edge vortex was produced depended both on wing configuration and spanwise proximity to the wingtip. A comparative analysis of apparent leading edge vortex size and chord position over the wing top surface was done for all dynamic test conditions.

A comparison of the flow fields produced about each wing

configuration at S = 0.67c and K = 1.0 is depicted in Fig. 20, for one complete oscillation cycle. Each photographic series shows the formation of a vortex near the leading edge as the wings approach maximum angle of attack, $\alpha = 25°$ (phase angle $\phi =$ 0.0). Despite the similarity in vortex initiation, each wing configuration differs in leading edge vortex growth, development and traversing characteristics. These differences can be seen in side-by-side comparisons in Fig. 20.

The FSW, left column, shows the formation of a small leading edge vortex as well as a second vortex, near midchord, during the early portions of the pitching cycle. The leading edge vortex remains stationary near the leading edge showing little growth while the second vortex both traverses toward the wing trailing edge and appears to grow in size. Coincident with the second vortex shedding from the trailing edge, $\phi = 0.4$, the leading edge vortex can no longer be visually resolved in an apparent shear layer which covers the entire top surface. No leading edge vortical structure is evident until the wing again approaches the maximum angle of attack in the next oscillation cycle. The STW, center column, also forms both a leading edge vortex and second downstream vortex structure at maximum α. The leading edge vortical structure grows and seems to become turbulent when the second vortex is shed, $\phi = 0.4$. The ASW, right column, initially forms a much larger definite leading edge structure. This structure continues to increase in size as it

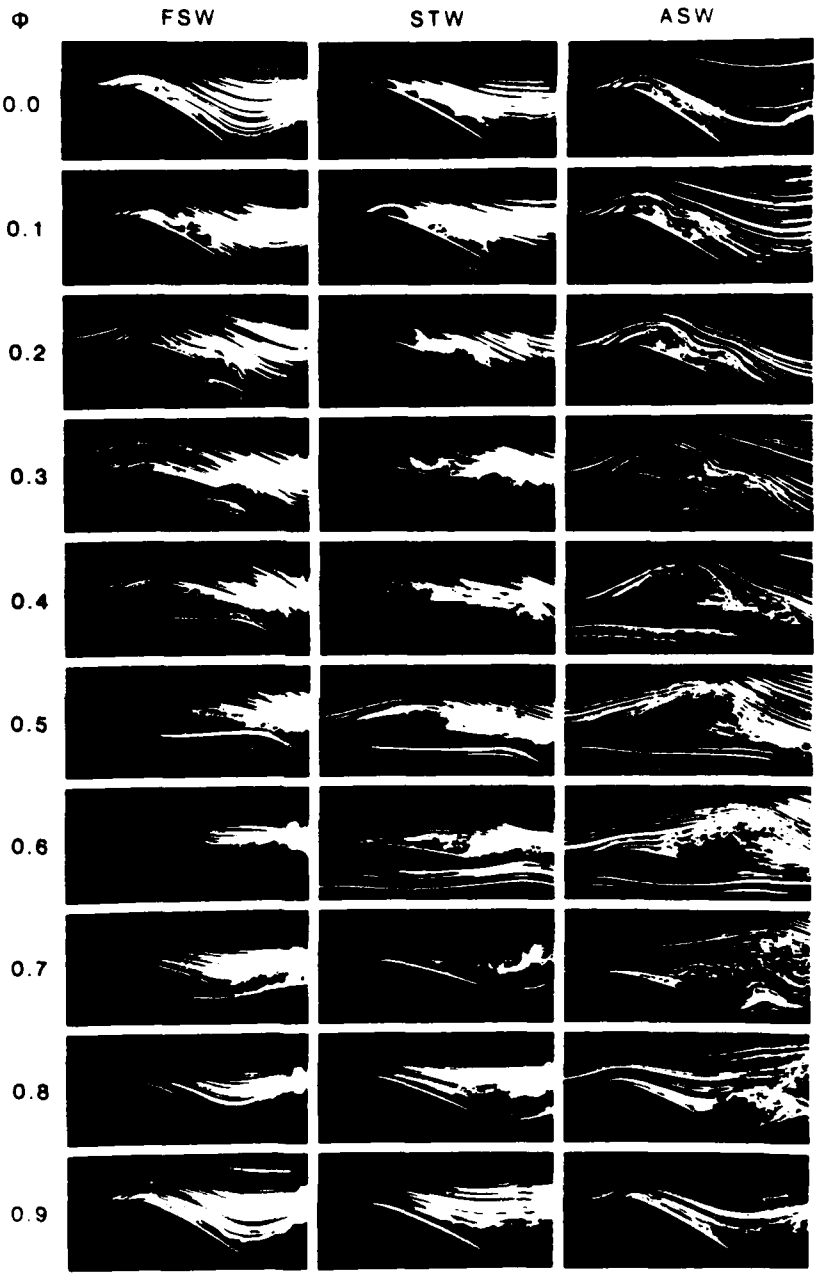

Fig. 20 Photographs of one pitching cycle, S = 0.67c, K = 1.0, ϕ = 0.0: α = 25°, ϕ = 0.5: α = 5°.

convects over the wing surface.

The relations between apparent leading edge vortex positions along the top surface of each wing are summarized in Figs. 21, 22 and 23 for different phases of the oscillation cycle. These planform diagrams depict the leading edge vortex position across the wingspan for one half of a pitching cycle, ϕ = 0.0 to 0.5, using K = 1.0. A shear layer was present on the aft portion of the FSW (Fig. 21). It extended from the wingtip to a span location of nearly S = 1.00c inboard. This layer appeared to prevent the formation of a discernible leading edge vortex near the wingtip. It also appeared to inhibit the downstream convection of the leading edge vortex even at span locations more inboard than S = 1.0c. Near midspan, this shear layer engulfed the leading edge vortex when the second vortex (formed near midchord) was shed from the trailing edge. The STW (Fig. 22) produced more conventional vortex growth and convection characteristics. The fastest convection of the leading edge vortex occurred at S = 1.0c. A distinct leading edge vortex was present on the ASW (Fig. 23) even at a location, S = 0.17c, very near the wingtip. Quite proximal to the tip, the wingtip vortex seemed to cause the leading edge vortex to become turbulent and to move upward, away from the top surface of the wing. A shear layer apparently was present near the ASW root position, S = 1.33c, resembling that observed near the wingtip in the FSW tests. For all wing configurations, the convection velocities of

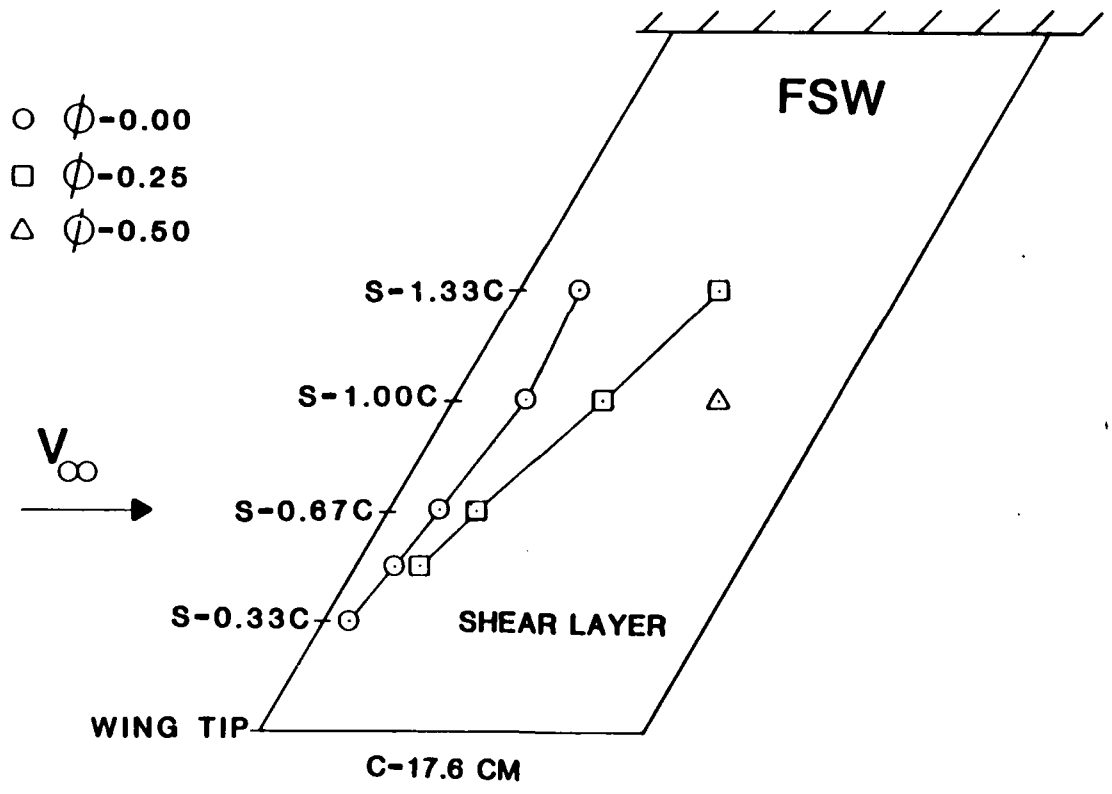

Fig. 21 Planform of leading edge vortex position, FSW, K = 1.0, ϕ = 0.0: α = 25°, ϕ = 0.5: α = 5°.

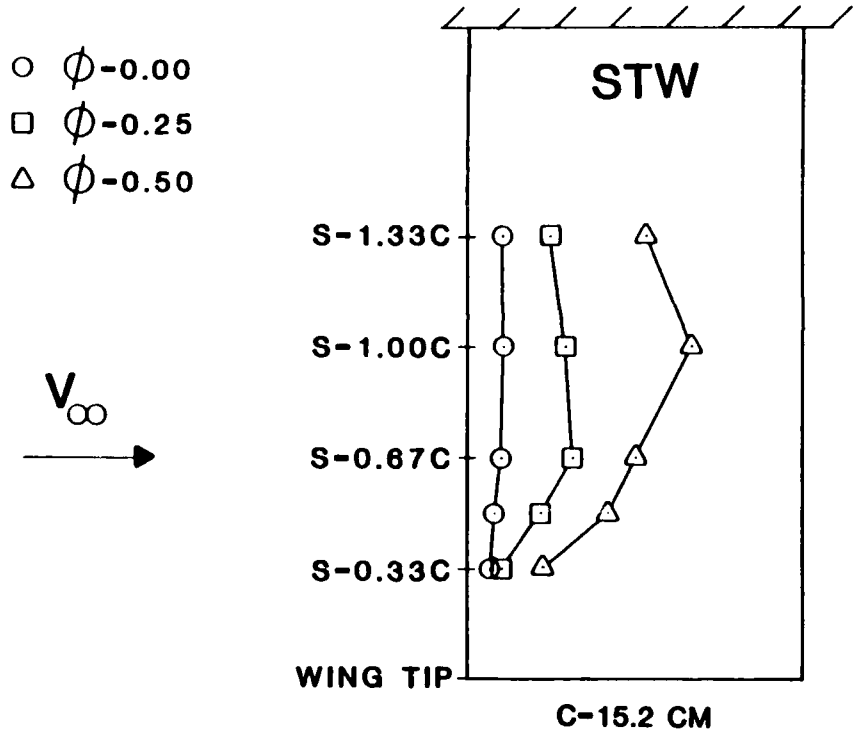

Fig. 22 Planform of leading edge vortex position, STW, K = 1.0, ϕ = 0.0: α = 25°, ϕ = 0.5: α = 5°.

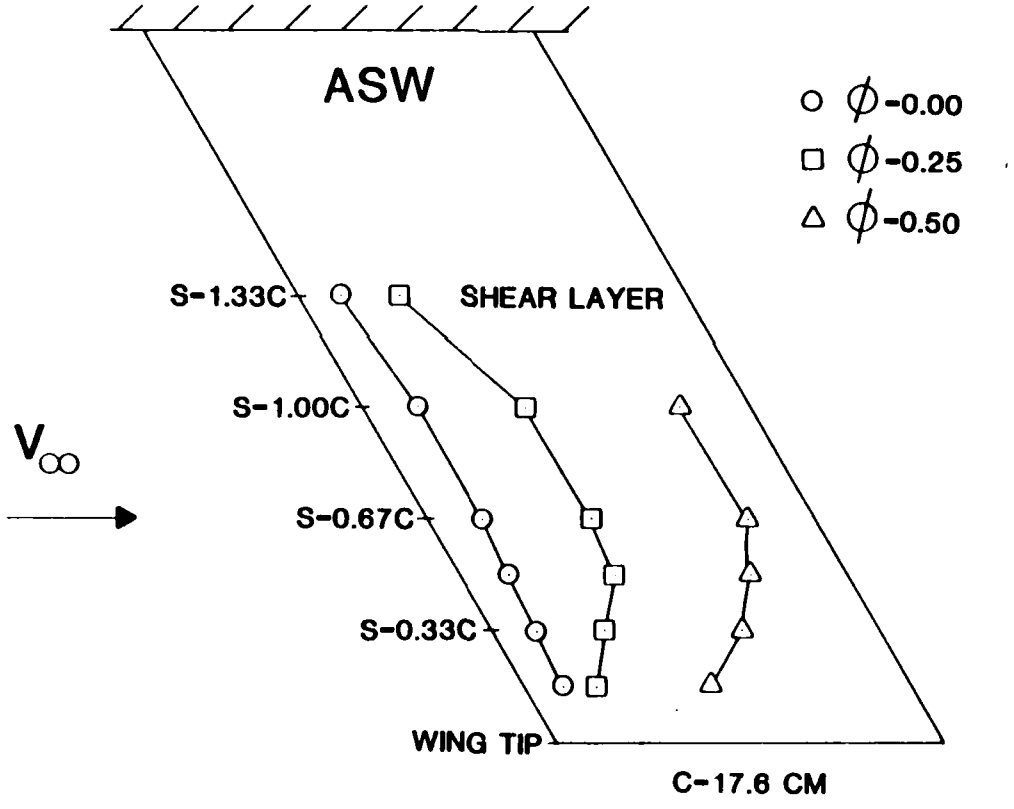

Fig. 23 Planform of leading edge vortex position, ASW, K = 1.0, ϕ = 0.0: α = 25°, ϕ = 0.5: α = 5°.

the leading edge vortex across the upper wing surface were slower near the wingtip than the more inboard locations investigated.

Leading edge vortex size was dependent on span location and wing configuration. Plots of vortex size are shown in Fig. 24, for K = 1.0. The leading edge vortex size was, on an average, consistently smaller for the FSW than for the other two wings. A shear layer dominated the FSW for S = 0.33c and 0.67c. Farther inboard, S = 1.0c and 1.33c, the leading edge vortex is well developed but remains small in size compared to vortices of the STW and ASW.

The largest leading edge vortical structures were observed for the STW at S = 1.0c. The leading edge vortex structures for the STW were small near the wingtip, S = 0.33c and S = 0.67c, and were somewhat larger near the root test position, S = 1.33c.

The ASW leading edge vortex size varies most for different spanwise test locations. Near the wingtip, S = 0.33c and S = 0.67c, the leading edge structures for the ASW developed to a larger relative size than observed using the other two wings. As spanwise test location was increased to more inboard sites, an apparent shear layer began to form and dominate the flow field as the second vortex was shed off the trailing edge.

Altered K values of 0.6, 1.0 and 1.4 caused variations in leading edge vortex size and chord location for each wing tested. The variations produced by different K values, however, were

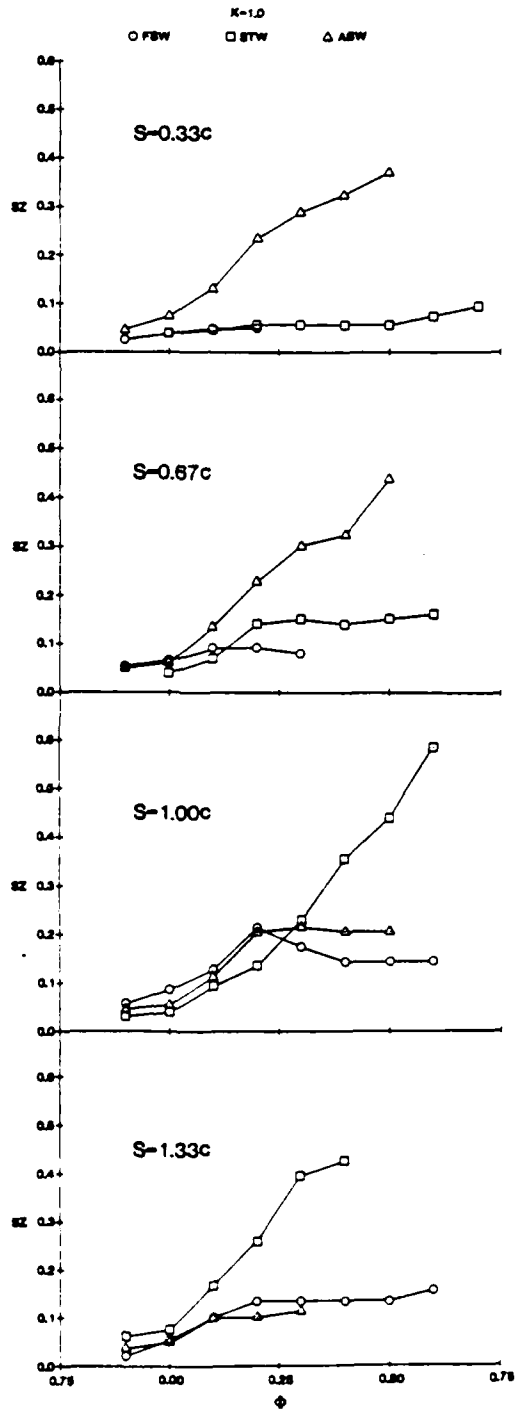

Fig. 24 Leading edge vortex size, K = 1.0, S = 0.33c to 1.33c.

similar to those reported earlier. No qualitative changes occurred and the flow fields were characteristic of the sweep effects noted above. Thus, the higher K values yielded more cohesive leading edge structures. For the STW, the structures appeared energetic enough to cause splitting of the initial leading edge vortex structure into separate vortices.

Other observed phenomenon. On the surface of the STW using K = 1.4, the leading edge vortex was observed to split into two separate vortical structures. One complete pitching cycle is displayed in Fig. 25, for a span location of S = 0.67c. At or near the top of the pitching cycle (A, where $\alpha = 25°$), multiple vortex structures can be seen forming along the top wing surface. As the pitching cycle carries the wing downward (B, C, and D), primary and second vortices are clearly formed and are beginning to convect toward the trailing edge of the wing. The primary vortex then appears to divide into two components (E & F): (1) a smaller, upstream leading edge vortex, and (2) a larger, downstream vortex comprised of a considerable amount of turbulence. Each structure then convects and is shed in tandem from the trailing edge (G through J).

Additional details of the dividing of the leading edge vortex across the wingspan are depicted in Fig. 26. Near $\phi = 0.0$, a distinct vortex is seen to form nearly parallel to the leading edge at all span locations inboard of the wingtip. At approximately $\phi = 0.25$ on the downward part of the pitching

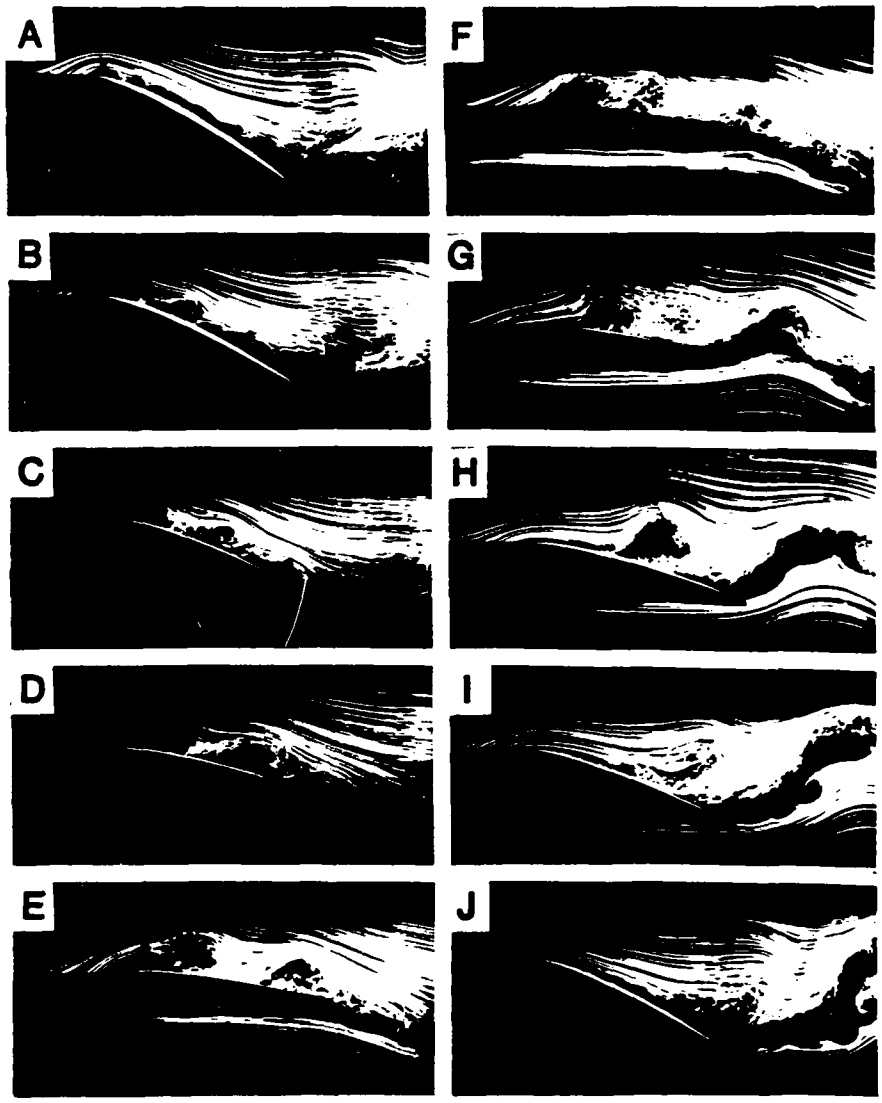

Fig. 25 Leading edge vortex dividing over one pitching cycle, STW, S = 0.67c, K = 1.4.

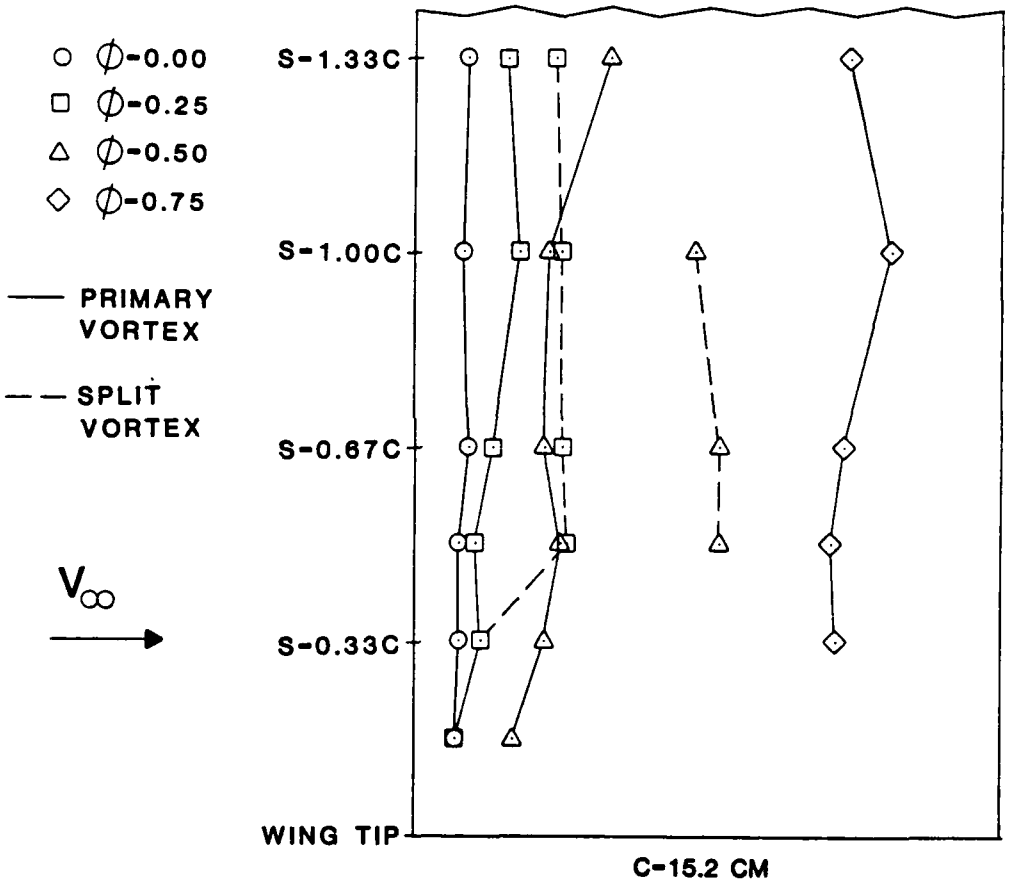

Fig. 26 Planform of leading edge vortex dividing and traversing, STW, K = 1.4.

cycle, the primary vortex has divided into two vortical structures, each with separate positions on the wing surface. Halfway through the pitching cycle, $\phi = 0.5$, the distance between the two vortex centers has increased and at $\phi = 0.75$ the more turbulent vortex core has shed from the trailing edge. The primary leading edge vortex continues to convect toward the trailing edge. This vortex dividing phenomenon also was observed for the ASW but the magnitudes of the primary leading edge vortices were very small. No vortex dividing was observed for the FSW.

CHAPTER VI

ANEMOMETRY AND VISUALIZATION COMPARISONS

Flow visualization techniques provide documentation of fundamental unsteady flow characteristics elicited by the three geometrically distinct wings. Quantification and comparison of flow characteristics such as vortex size, position, temporal development, and convective tendencies can be achieved visually. However, any further quantification of the three-dimensional unsteady flow field about these wings must include other data collection techniques. So, to further verify hypotheses initiated by flow visualization studies, velocity data were collected using hot wire anemometry. The hot wire recorded the absolute velocity of the flow field during the cyclic motion history of the three wings. The anemometric measurements were taken at spanwise locations coincidental with previously acquired flow visualization data for each wing geometry. Seven chordwise locations were examined; 0.00c (leading edge), 0.17c, 0.33c, 0.50c, 0.67c, 0.83c and 1.00c (trailing edge). Velocity data were computer collected and ten phase-locked samplings (over 200 points per run) were averaged for two complete oscillation cycles. Chordwise and spanwise effects of wing sweep angle for identical test conditions (Re, K, α_m and α_ω) are recorded by

visualization and anemometry techniques.

A flow visualization versus velocity comparison is shown in Figs. 27 and 28 for the STW at K = 1.0 and S = 0.67c. The hot wire probe positions from leading edge (A) to trailing edge (G) can be seen in the left column for ϕ = 0.2 in the oscillation cycle. The right column contains coincidental probe position velocity measurements computer plotted over two complete oscillation cycles. The ϕ = 0.2 point of each cycle is marked with dashed lines and are plotted in Fig. 28. The velocity comparisons at ϕ = 0.2 illustrate the unsteady fluid dynamic variations across the chord of the wing. The probe at the leading edge, Fig. 27 A, is positioned in the high velocity region of potential flow as it passes over the leading edge of the wing. Here at ϕ = 0.2 the local velocity is nearly 1.5 V_∞. At C = 0.17c, Fig. 27 B, the probe records the much lower velocity of the apparent interior of the dynamic stall vortex. When the probe is near the aft circumference of the vortex, Fig. 27 C, the velocity is near freestream value. As the probe moves further aft, C = 0.50c to 1.00c, shown in Fig. 27 D-G, the velocity measurements are taken aft of the leading edge vortex and above the midchord structure at this phase angle. Analysis of velocity fluctuations for all probe positions indicates, as with all other test conditions on all wings, the greatest velocity variations at C = 0.17c along the chordlength.

Since greatest velocity fluctuations over an oscillation

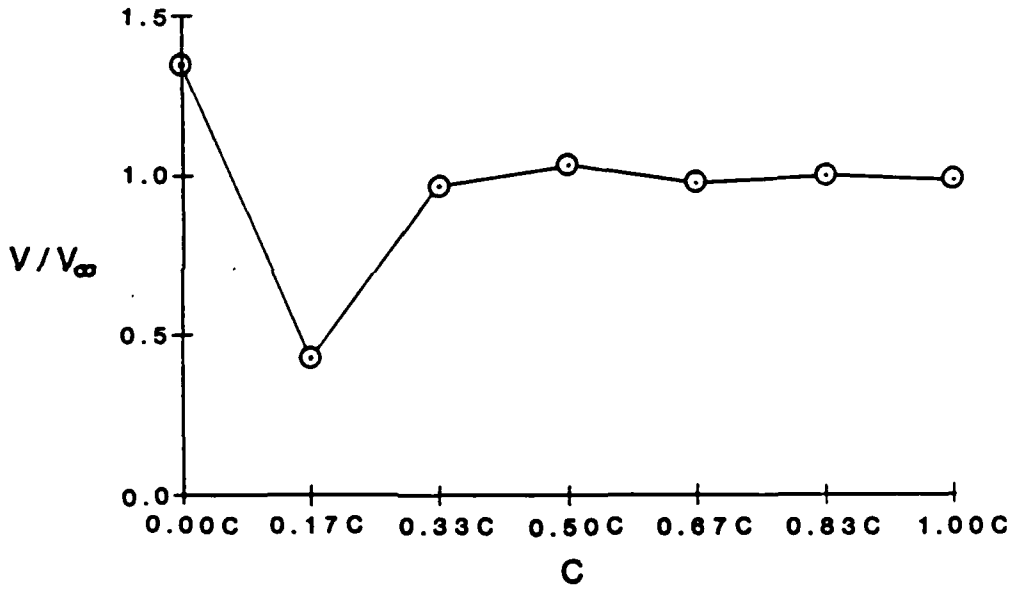

Fig. 28 Velocity comparison along chordlength, STW, K = 1.0, Z = S = 0.67c, ϕ = 0.2.

cycle occur at C = 0.17c, a comparison of flow visualization and hot wire data for the STW at S = 0.67c and K = 1.0 are made at this chord location, Fig. 29. The hot wire probe is seen in the photographs in A through J as the oscillation cycle varies in ten equal increments from ϕ = 0.0 to 0.9, respectively. The averaged velocity data and coincidental standard deviation are plotted for two complete cycles. Instantaneous local velocities coinciding with each photograph are labeled. At the start of the pitching cycle, α = 25 degrees and ϕ = 0.0, shown in Fig. 29 A, the hot wire is located near the high velocity circumference of a forming leading edge vortex and the local velocity is more than twice freestream value. As the downward pitching continues to ϕ = 0.1, shown in B, the vortex is larger and the probe is now approaching the vortex core. A corresponding decrease in velocity at point B is observed. At point C, ϕ = 0.2, the hot wire probe is visualized inside the vortex core and a velocity less than half freestream is recorded. Point D shows the probe still inside the vortex and indicates a correspondingly low velocity. The probe at point E is entering the higher velocity region near the forward edge of the vortex as aft convection of the vortex continues. Points F-I show a seemingly non-cohesive, turbulent vortex traversing the surface aft of the probe position. The velocity continues to increase from F to I as the potential flow reattaches to the wing surface after passage of the leading edge vortex. Point J shows vorticity coalescing

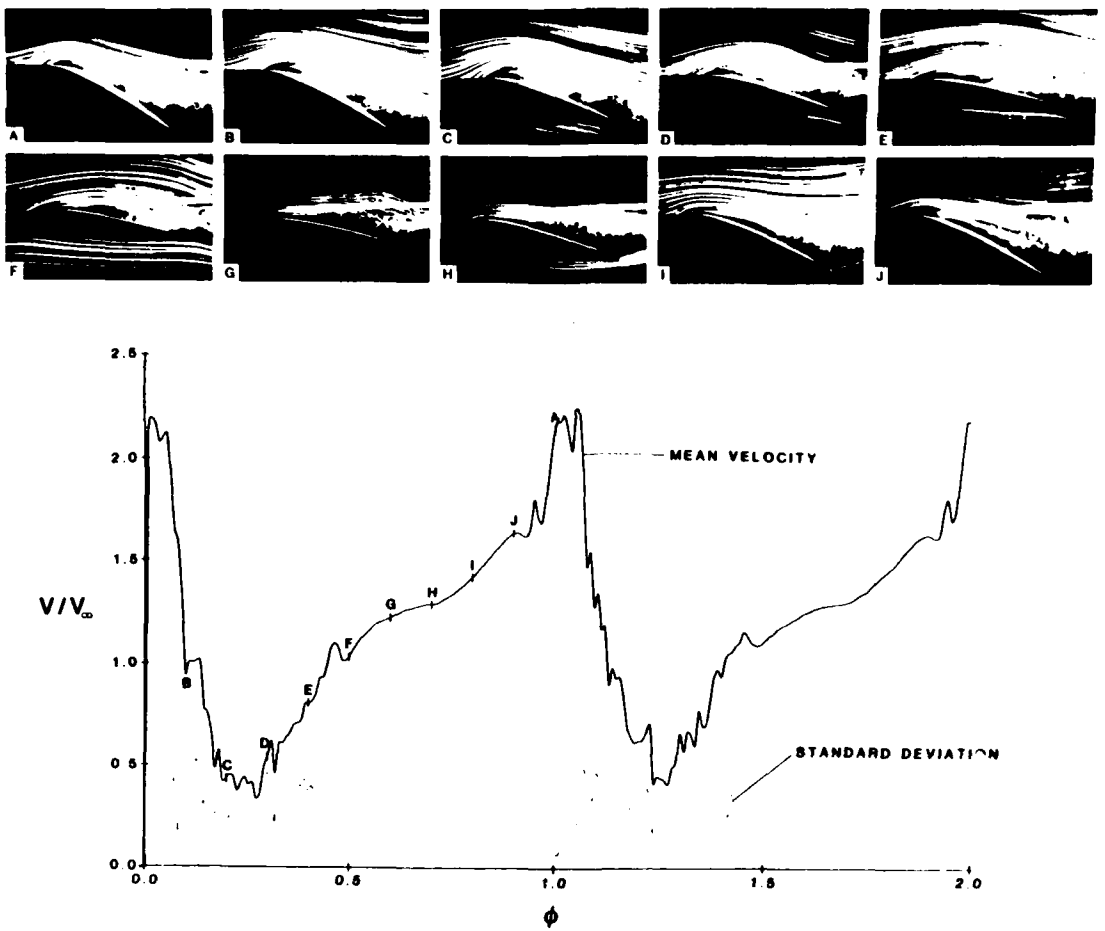

Fig. 29 Flow visualization and hot wire comparison, STW, K = 1.0, C = 0.17c, S = 0.67c.

toward the initiation of a new, large scale vortex near the leading edge of the wing.

The hot wire probe location at the trailing edge of the wing records velocities as the dynamic stall vortex passes through this chord location. A flow visualization versus velocity comparison at C = 1.00c for the STW at S = 1.00c and K = 1.0 is shown in Fig. 30. The peak velocities at this chord position do not attain magnitudes as great as data taken at C = 0.17c. Passage of the leading edge vortex is recorded by decreased velocity values. During vortex initiation, growth and early convection, the probe is not encountering vortical flow and the recorded velocities are near freestream values. When the leading edge vortex is shed, Fig. 30 H, I and J, the shedding of free vorticity from the lower surface can be seen at the trailing edge.

The standard deviations of velocity fluctuations for the ten averaged data runs are also plotted for two oscillation cycles in Figs. 29 and 30. In both figures, the standard deviation increases when the probe is inside the leading edge vortical structure. This increase indicates more local velocity fluctuations in the interior of the vortex. The standard deviation plots begin to increase as soon as the hot wire probe records the velocities interior to the vortex and decrease when the probe begins to sense the more structured, high speed velocities of the vortex circumference. When the probe is not

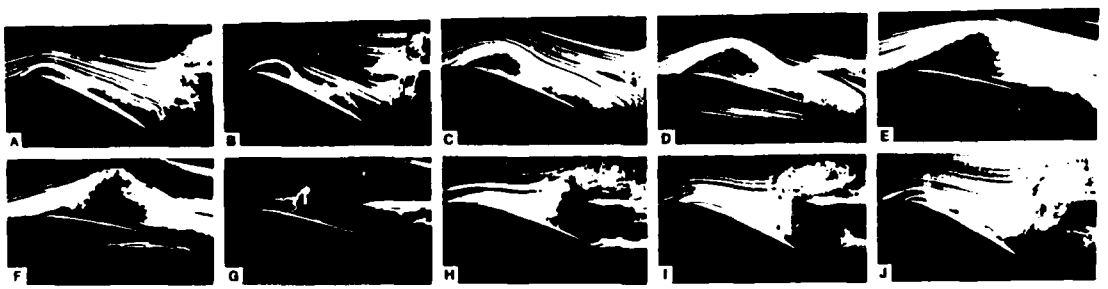

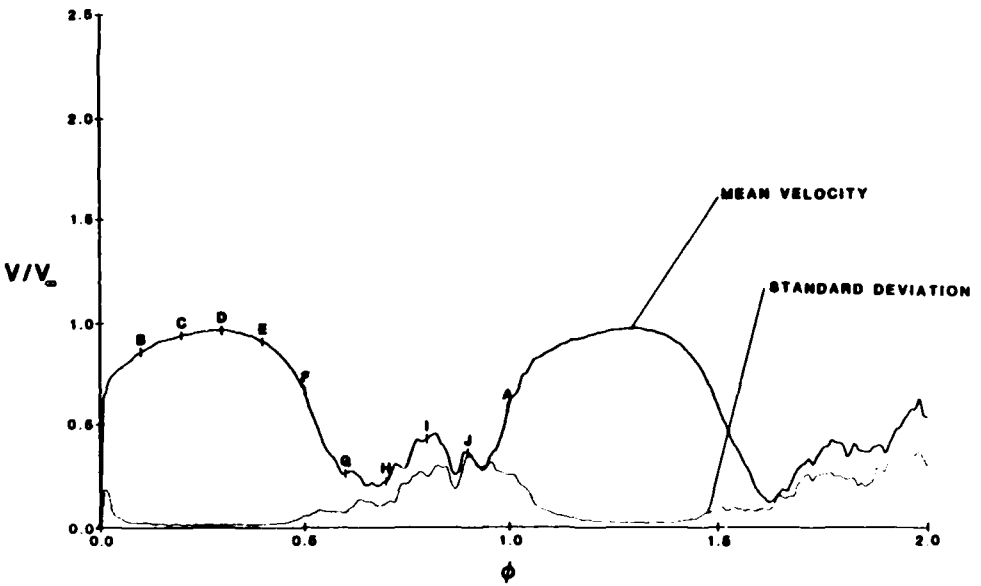

Fig. 30 Flow visualization and hot wire comparison, STW, K = 1.0, C = 1.00c, S = 1.00c.

encountering interior vortex flows, the standard deviations are very small.

The spanwise deflection angle, β , of the flow at the wingtip was recorded from top view flow visualization. Phase-dependent comparisons of these β angles with anemometric velocity measurements at the wingtip are shown on Figs. 31, 32 and 33. The velocity data points were plotted for chord location C = 0.17c, however, identical velocity trends were noted at all chord locations from leading to trailing edge. The FSW data, shown in Fig. 31, illustrates similar trends in velocity and β measurements throughout one complete pitching cycle (ϕ= 0.0 to 1.0). The high velocity and β magnitudes occur during high angle of attack portions of the pitching cycle while the minimum values are recorded near minimum α portions. This velocity profile was also observed inboard along the span until nearly midspan, S = 0.67c, where effects of leading edge vortex development altered the shape of the velocity curve. Similar comparative velocity and β angle results are noted for the STW in Fig. 32. Spanwise observations reveal that this wingtip velocity profile exists inboard along the span only to the S = 0.33c location. The ASW data, shown in Fig. 33, again, shows similar trends in velocity and β angle. These profiles display the highest magnitudes on both plots during the downstroke of the cycle after passage of maximum angle of attack. The minimums are also shifted until the upstroke of the cycle after minimum is

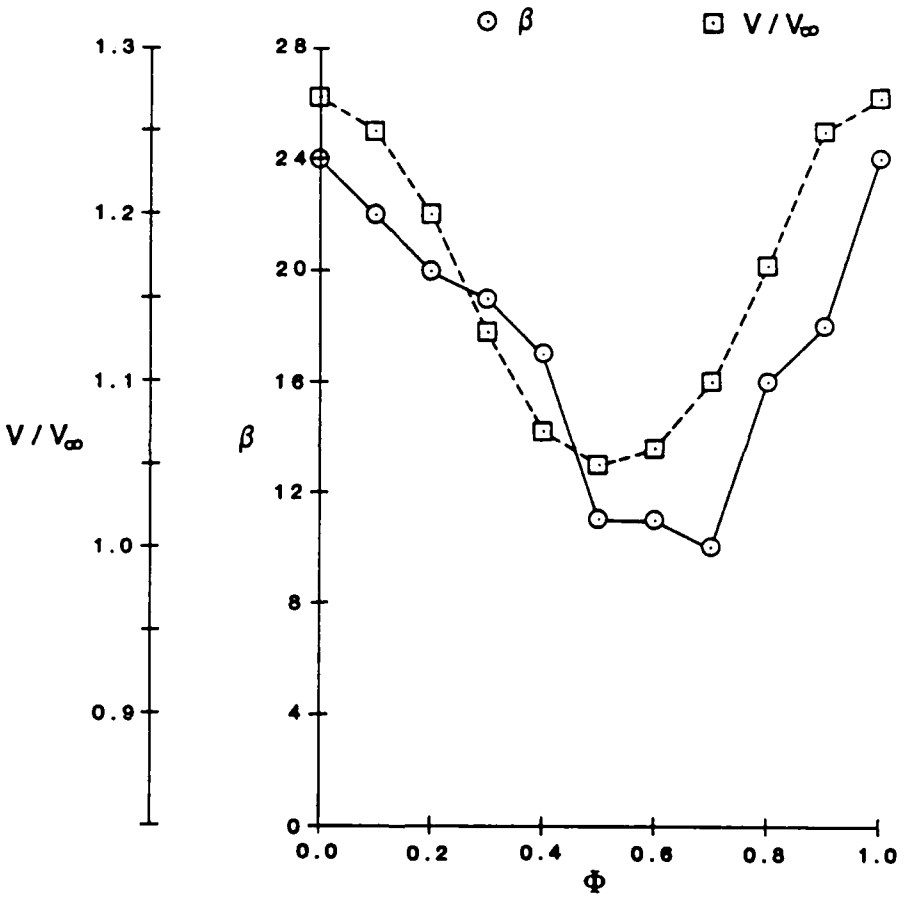

Fig. 31 Velocity and β angle comparisons, FSW, K = 1.0, C = 0.17c, S = 0.00c.

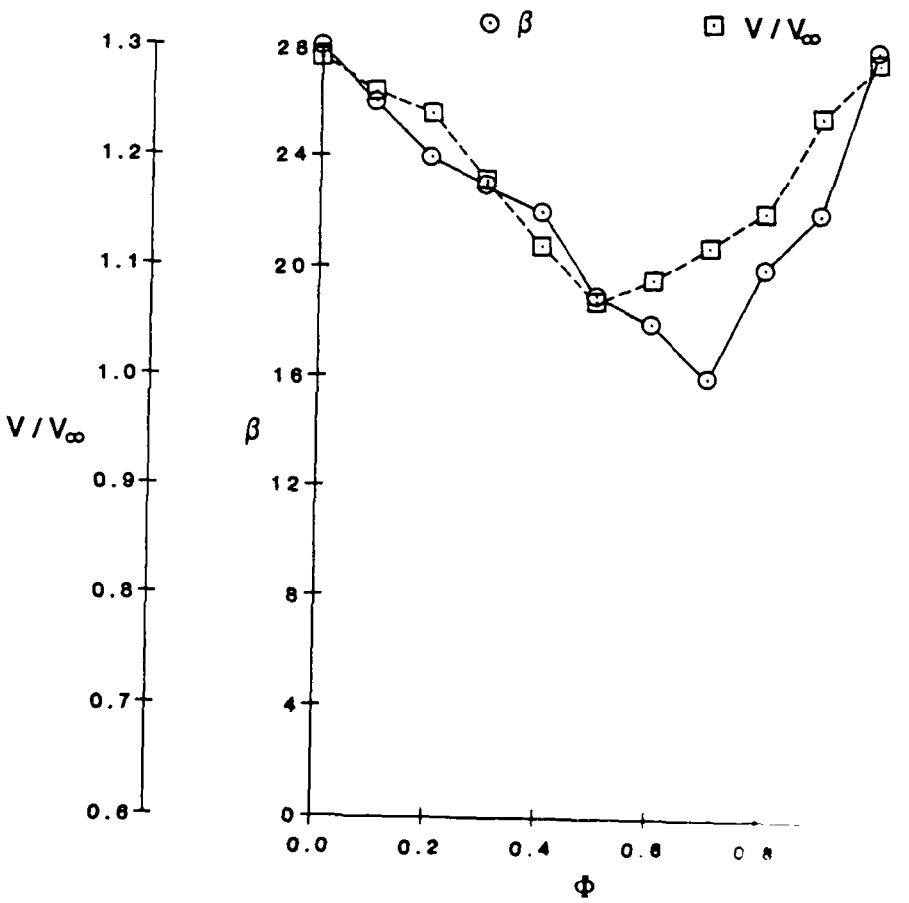

Fig. 32 Velocity and β angle [illegible]
C = 0.17c, S = 0.00c

AD-A186 464 THREE-DIMENSIONAL UNSTEADY FLOW ELICITED BY FINITE WINGS AND COMPLEX CONFIGURATIONS(U) AIR FORCE INST OF TECH WRIGHT-PATTERSON AFB OH J C ASHWORTH 1987 2/2

UNCLASSIFIED AFIT/CI/NR-87-142D F/G 1/1 NL

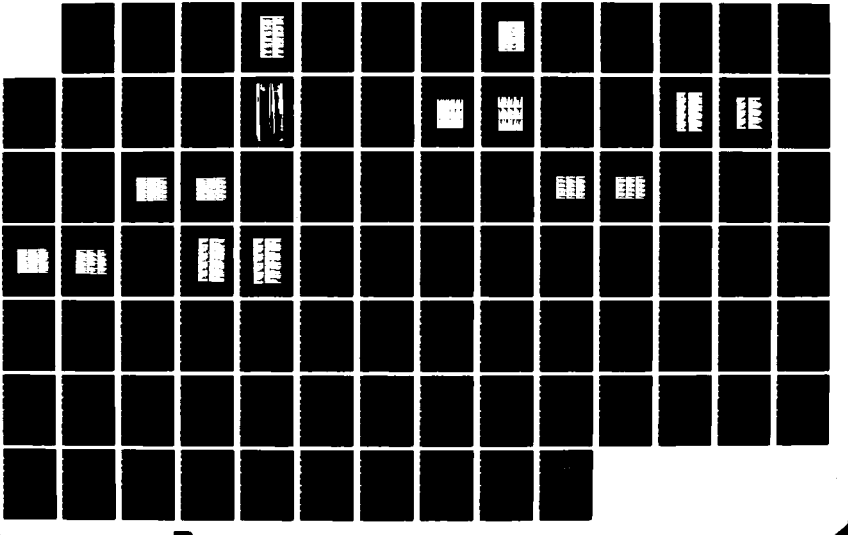

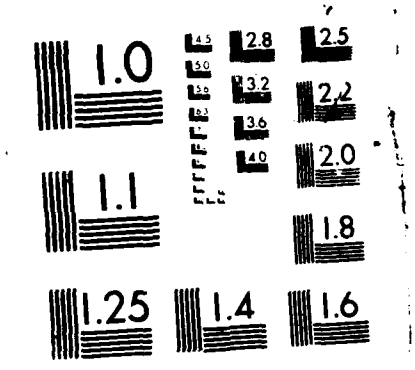

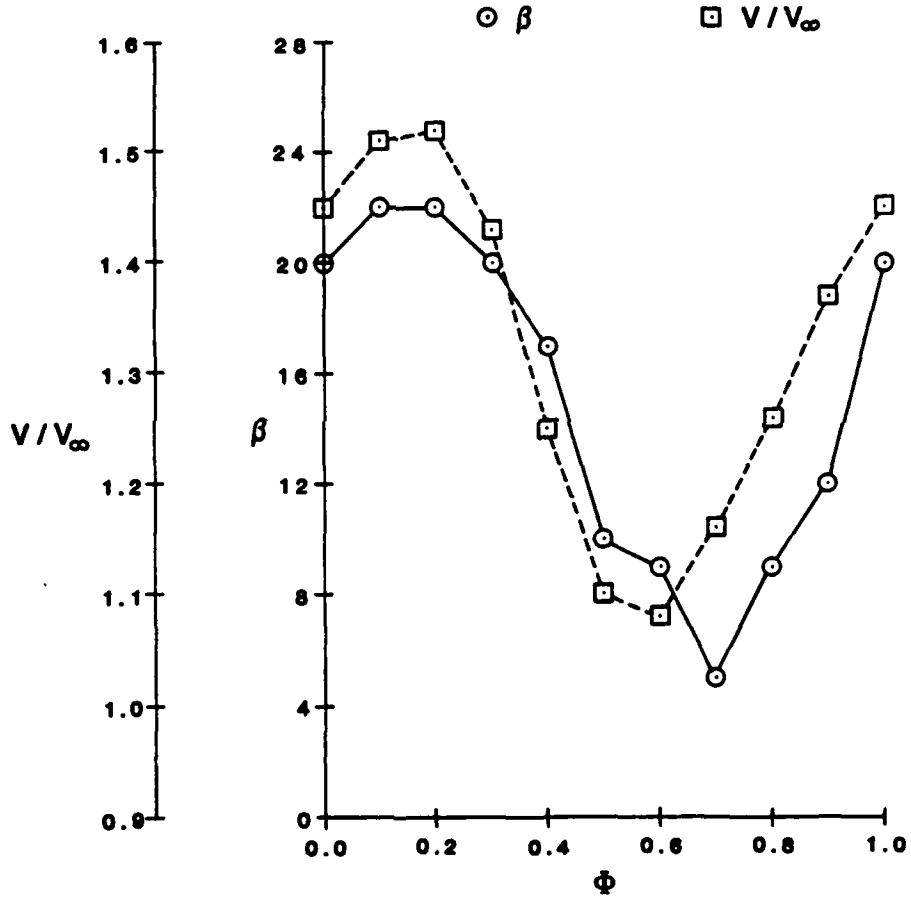

Fig. 33 Velocity and β angle comparisons, ASW, K = 1.0, C = 0.17c, S = 0.00c.

passed. The leading edge vortex effect is observed over the aft portion of the ASW even at the wingtip location. The previously observed wingtip profiles for the FSW and STW were not observed for the ASW at any span location inboard from the tip.

Flow visualization has revealed large temporal and spatial differences in leading edge vortex structures for each of the three wings when various span locations are examined. A spanwise sideview of the streaklines as seen for two points in the oscillation cycle, ϕ = 0.0 and 0.3, is depicted in Fig. 34 for the STW. At or near the wingtip (S = 0.00c and 0.17c), a strong wingtip vortex is traced out by the smoke. A leading edge vortex, multiple vortices and shear layer are observed at more inboard span locations, S = 0.33c to 1.33c.

Spanwise comparisons for each wing geometry at C = 0.17c and at instantaneous phase angles of ϕ= 0.0 and 0.3 are shown in Fig. 35. The flow visualization photographs in Fig. 34 can be matched to the velocity profiles in Fig. 35 B. The velocity data of Fig. 35 for ϕ = 0.0 show a steadily increasing V/V_∞ as inboard distance from the wingtip increases. Flow visualizations for this phase angle indicate the probe position is located in the high velocity circumference of a small, newly forming leading edge vortex. The velocity profile at ϕ = 0.3 increases for S = 0.0c to 0.33c where visualization shows a dominant wingtip flow and a dominant leading edge vortex, respectively. At S = 0.50c to 1.00c, the leading edge vortex has become progressively larger

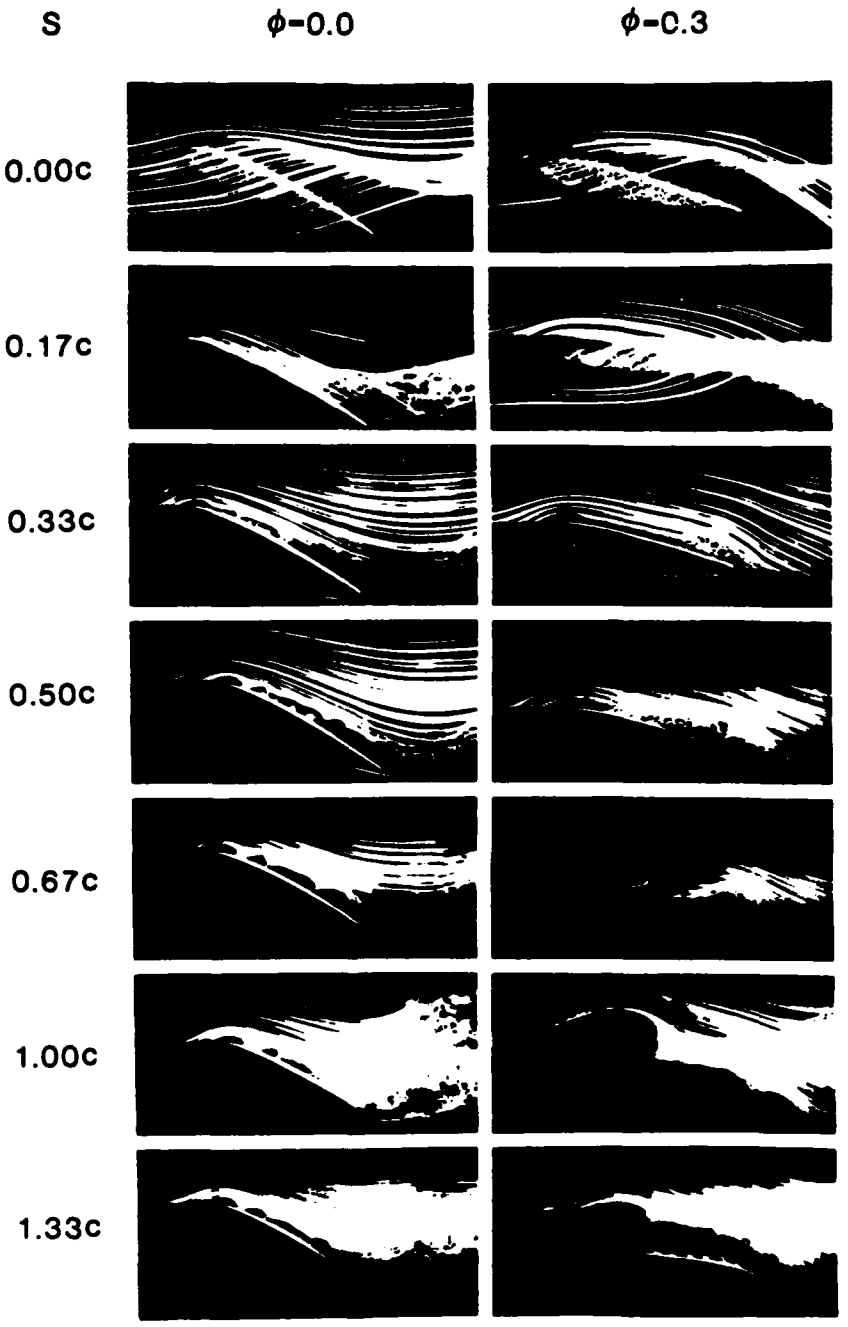

Fig. 34 Photographic depiction along span, STW, K = 1.0, ϕ = 0.0 and 0.3.

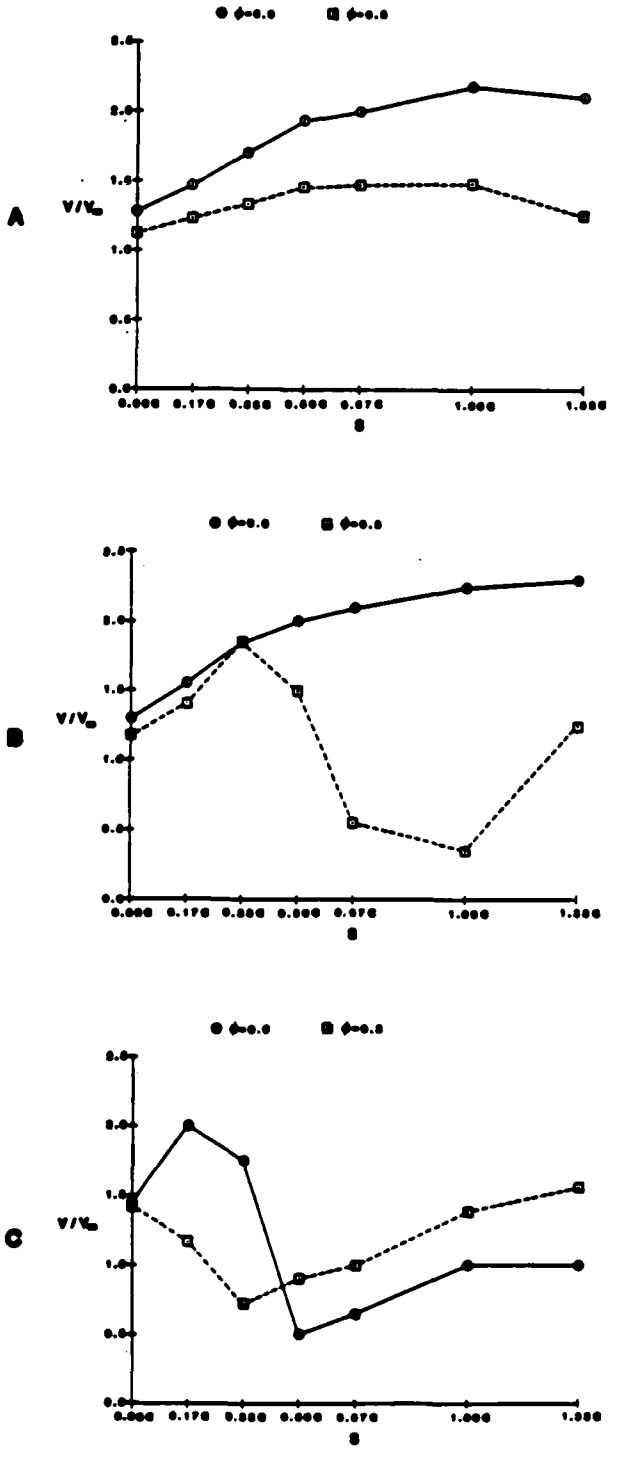

Fig. 35 Velocity comparison along span, K = 1.0, C = 0.17c, A - FSW, B - STW, C - ASW.

such that the probe at C = 0.17c is located inside the apparent vortex core. Accordingly, a large velocity decrease is measured. A velocity increase at S = 1.33c is correlated visually with a leading edge vortex of decreasing size. The probe position is again near the higher velocity circumference of the vortex.

Wing sweep angle effects are apparent when comparing spanwise velocity data across the three wing geometries. Fig. 35 A, B and C show these comparisons. Velocity profiles for the FSW at $\phi = 0.0$ and 0.3 maintain characteristics similar to the STW at $\phi = 0.0$ since at both FSW phase angles the probe position is near the upper circumference of a forming leading edge vortex. The velocity magnitudes for $\phi = 0.3$ are smaller. This is coincidental with an apparent shear layer visualized forming on the FSW at this phase angle. The shear layer both prevents distinct leading edge vortex development outboard of the 0.50c span location and leads to smaller, less cohesive structures inboard.

Comparatively larger velocity gradients are observed for the ASW in Fig. 35 C. These velocity differences reflect the more cohesive leading edge vortical structures visualized by photography. At $\phi = 0.0$, the upper circumference of a leading edge vortex is encountered by the probe near the wingtip, and the lower velocities of the vortex core are sensed as the probe is moved inboard. A similar trend is noted at $\phi = 0.3$, however, the vortex core velocity minima are sensed by the probe at span

locations nearer the wingtip.

A spanwise visualization comparison for each wing at K = 1.0 and ϕ = 0.2 is shown in Fig. 36. These photographs depict the wingtip flow dominated regions and the leading edge vortical development as the span location varies from wingtip (S = 0.0c) to far inboard (S = 1.33c). Helical wingtip vortices are seen for all three wings at the wingtip. Even when the vertical smoke sheet impinges the wings at 0.17c inboard, smoke is pulled around the wingtip from the pressure to the suction surface indicating a strong wingtip effect. Near the leading edge of the ASW at this span position, a leading edge vortex is forming inboard of the wingtip flow. The FSW and STW show no indications of a leading edge vortex formation at this location. At S = 0.33c, the FSW and STW evince a shear layer across the wing surfaces with only a slight flow disturbance near the leading edge to indicate early coalescence of vorticity into a large scale vortex. The ASW at this span location elicits a large leading edge vortex structure which covers nearly half the wing top surface. As the smoke sheet is moved inboard, S = 0.50c, a leading edge vortex and second vortical structure are visible on all three wings. The size of the leading edge structure increases for the FSW, STW and ASW, respectively. Progressing further inboard, the size of the leading edge vortex on the FSW and STW increases until, at S = 1.00c, the leading edge vortices on all three wings appear similar in size. At this span location, the three-dimensional

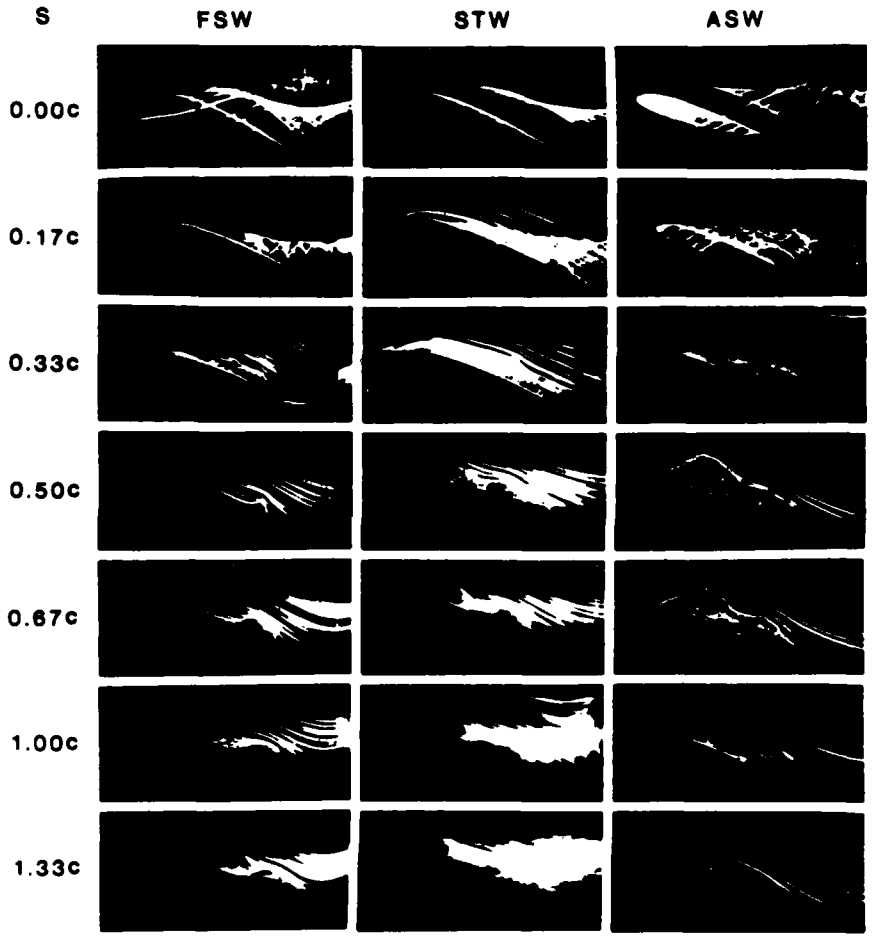

Fig. 36 Spanwise visualization comparisons, K = 1.0, ϕ = 0.2.

effects for each wing may reduce to nearly two-dimensional phenomenon. Further inboard, S = 1.33c, the leading edge vortex on the FSW continues to increase in size while the ASW structure decreases.

A comparison of local velocity profiles across the wingspan at C = 0.17c is shown in Figs. 37, 38 and 39 for the FSW, STW and ASW, respectively. The FSW and STW show very little leading edge vortex effect at the wingtip, S = 0.00c. However, the local velocity of the ASW increases at the wingtip during the pitching cycle, ϕ = 0.0 to 0.3, when a strong leading edge vortex is forming on the top surface immediately inboard of the wingtip. At S = 0.33c, the FSW local velocity profile indicates the presence of the visualized small, nearly nondiscernible leading edge vortex. The STW at this span location is visually observed to produce more cohesive leading edge structures, reflected by the velocity curves. The ASW curve at S = 0.33c graphically represents the visualized formation and convection of a leading edge vortex. For this wing, at ϕ = 0.0 to 0.6, the probe at C = 0.17c is inside the forming and developing leading edge vortex. From ϕ = 0.6 to 0.8 the leading edge structure convects aft of the probe position and the overall flow adheres to the contour of the upper wing surface near the probe. At ϕ = 0.9, a new leading edge vortex is visualized to be forming and the probe is in the high velocity flow near the forward edge of this leading edge structure.

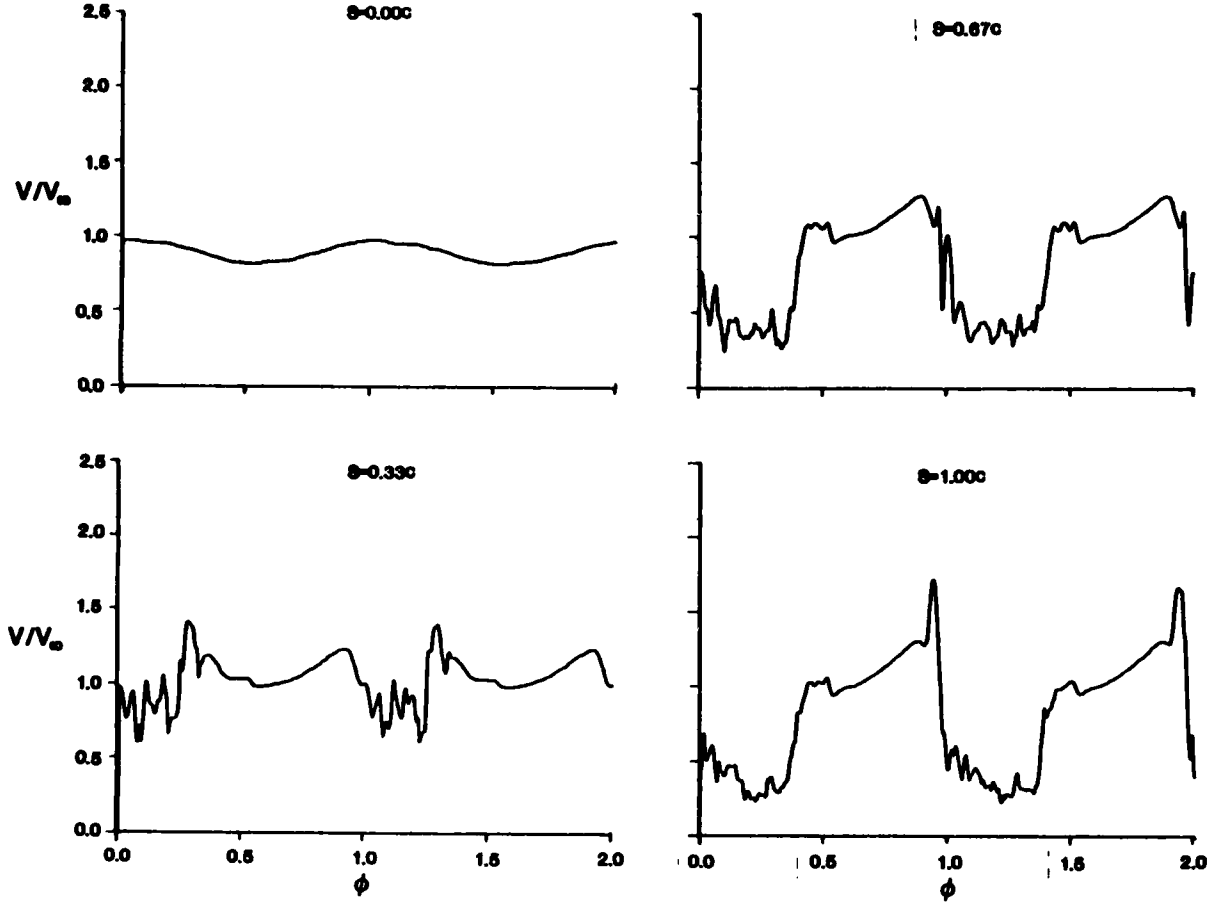

Fig. 37 Velocity profiles across span, FSW, C = 0.17c.

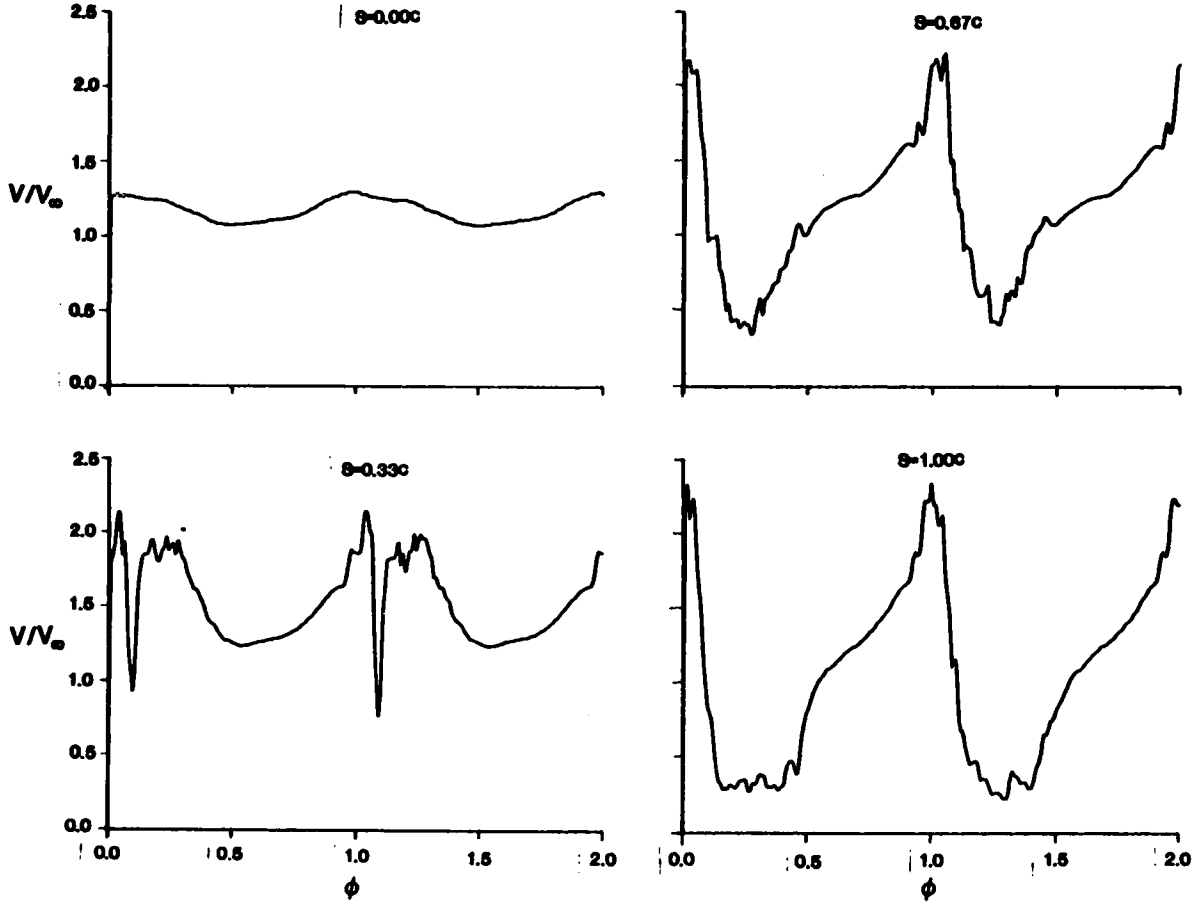

Fig. 38 Velocity profiles across span, STW, C = 0.17c.

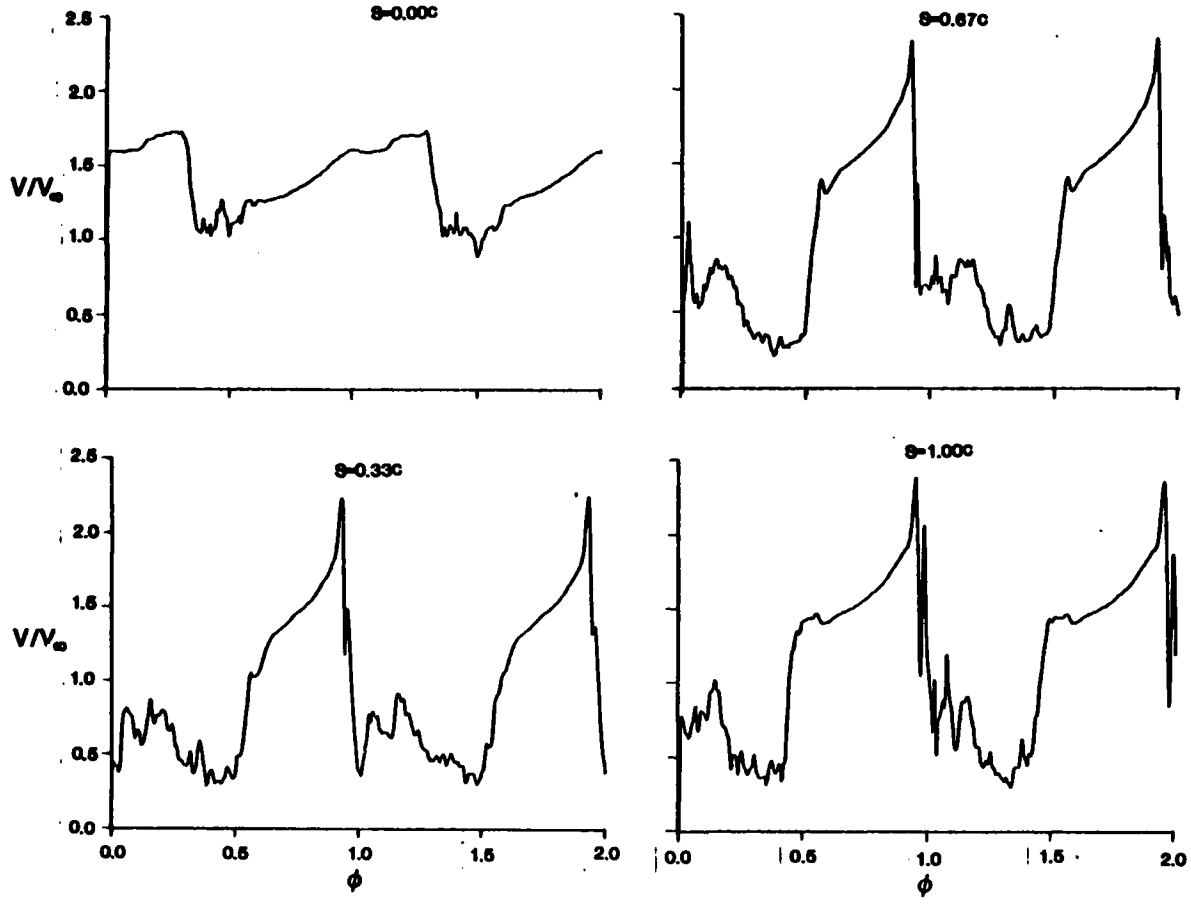

Fig. 39 Velocity profiles across span, ASW, C = 0.17c.

Flow visualization photographs depict more cohesive leading edge structures at S = 0.67c and S = 1.00c than near the wingtip for all three wings. This coincides with the more succinctly perturbed local velocity measurements shown for these span locations in Figs. 37, 38 and 39. The overall magnitude of the FSW velocity curves is not as high as the STW or ASW. This seems to reflect the smaller size and shorter convective paths observed during flow visualization. A visualization comparison of the three wings over one complete pitching cycle at S = 0.67c is shown in Fig. 20.

The effects of changing reduced frequency values can be seen in Fig. 40. These velocity profiles for the STW at S = 0.67c are shown for K = 0.6, 1.0 and 1.4. The velocity trends are similar with small fluctuations in absolute velocity magnitudes noted between different K value data.

Each wing geometry was tested at identical chordwise and spanwise locations for three K values, 0.6, 1.0 and 1.4. Since temporal leading edge vortex formation is K value dependent, a K value change shifted the velocity peaks to different phase points in the oscillation cycle for all three wings. Overall velocity peak fluctuations were compared for each wing at each K value. Changes in K value produced insignificant magnitude changes in the FSW velocity profiles. The STW profiles show little fluctuation with K value change except in the span region from S = 0.67c inboard. In this region, higher K values produced larger

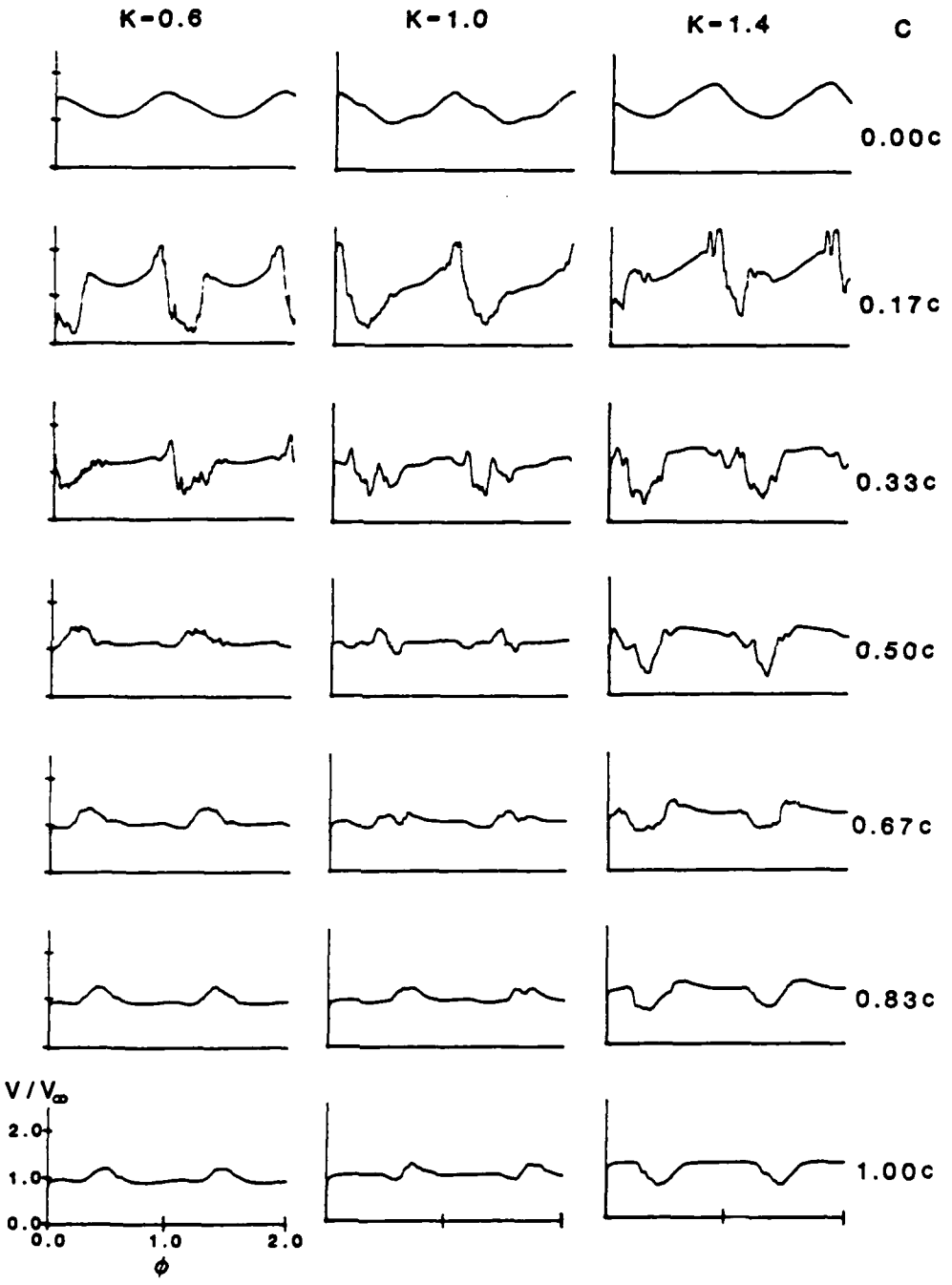

Fig. 40 Reduced frequency effects, STW, S = 0.67c.

variations in the velocity peaks. The ASW velocity profiles show greater velocity variations for smaller K values across the entire wing span.

A special note must be made in regard to velocity sampling of the three-dimensional flows. In almost all of the above velocity characterizations, the angles at which the flows intercept the hot wire probes were constant. In many cases, the incidence angles were not orthogonal to the hot wire sensor. But, the angles were consistent from one test condition to the next across most span and chord sites. Thus, although overall absolute velocities were undoubtedly less accurate than desired, comparative variations or fluctuations in local velocities were likely to be very reliable.

CHAPTER VII

UNSTEADY APPLICATION TO AN ADVANCED PROTOTYPE

Initial investigations on a one-tenth scale, reflection-plane model of the X-29 Forward Swept Wing Demonstrator Aircraft were conducted to provide insight into the complexity of flow interactions likely to be produced by such complex aircraft configurations in an unsteady separated flow environment. Possible aerodynamic benefits yielded by forced unsteady flows must be evaluated using such aircraft models. These tests were designed to give insight into the feasibility of using unsteady flows to enhance aircraft aerodynamics and to evaluate the flight mechanics needs of bringing such technology to fruition.

Low speed aircraft handling characteristics may be enhanced by the careful control of unsteady flows. In canard-configured aircraft, for example, flight qualities at low speeds and high angles of attack (AOA) are dependent on flow separation characteristics about both the canard and wing. The subsonic flow about either of these tandem surfaces affects the overall flow patterns within which the aircraft must perform. Unsteady oscillation of the canard may enhance lift and delay separation over it. The steady or unsteady downwash from the canard may also reduce the effective angle of attack of the trailing wing.

Since the forward swept wing stalls from root-to-tip, this canard-induced effective angle reduction may delay root stall and provide for higher aircraft angle of attack operation. To examine these and other possible effects, flow visualization comparisons between both static and dynamic (oscillating canard) configurations of the X-29 were accomplished for various AOA's and reduced frequency parameter values.

Visualization techniques applied to the in situ X-29 model show the complex geometric structure of this aircraft model configuration. A side view photo of this model is shown in Fig. 41. For these experiments, the model angle of attack (AOA) was varied in 5° increments from 0° to 10°. The canard angle of attack (α) was measured relative to the model centerline and could be varied between ±40°. Both static and dynamic experiments were done with this unique canard/forward-swept-wing configuration. The large interactive flow area produced between the canard and the trailing wing, showed intricate vortical structures during single plane wing tests. These are somewhat difficult to capture visually. Consequently, the detailed vortical flow development is sometimes sacrificed to enhance the clarity of general flow characteristics about the tandem surfaces as viewed from both side and rear camera perspectives.

Both the canard and wing planforms elicit complex three-dimensional flow patterns. The model geometry was similarly complex. The vertical plane of smoke streaklines were

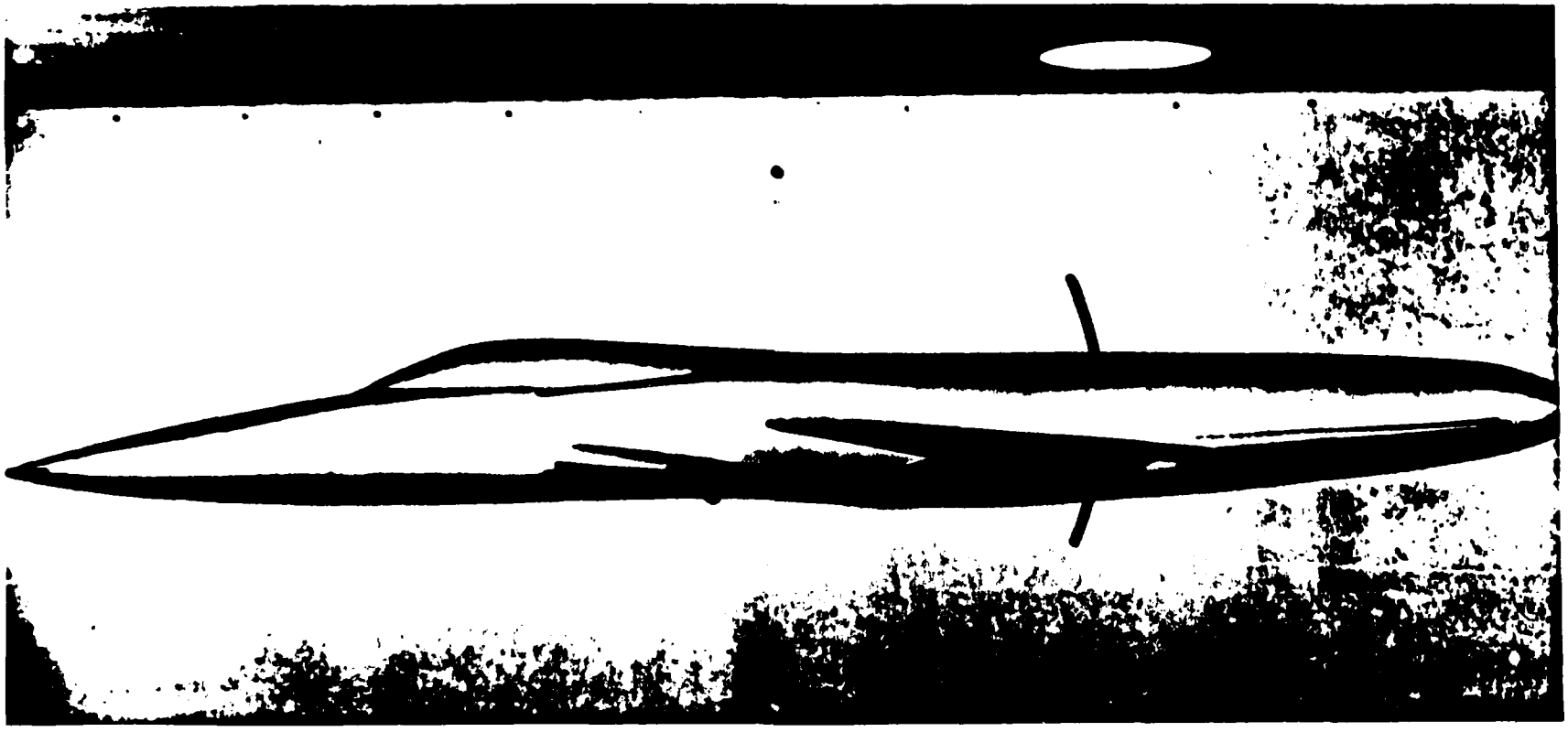

Fig. 41 Tunnel side view of 1/10-scale, reflection-plane model of the X-29 Forward-Swept Wing Demonstrator Aircraft.

positioned to intercept the canard at midspan. At this midspan site the chordlength is six inches and the overall canard taper ratio is 2.86. The canard planform consists of a 42° aft swept leading edge. The trailing edge swept aft very near the root then 28° forward across the outer span. The resulting tip chord was 2.8 inches. Although general finite wing flow characteristics were observed, this tapered configuration and small thickness ratio prevent exact comparisons with the oscillating wing data of the previous experiments. The wing leading edge planform also contains both a forward and aft swept profile. The predominant forward swept span intercepts the aft swept region near the root location where the smoke impinges the surface. This aft-swept/forward-swept planform has been observed (Griffin, et al., 1983) to produce inboard and then outboard spanwise flows which converge and create a leading edge crank disturbance. This effect is quite predominant at higher model angles of attack than used in the present studies. Exact flow characteristics attributed to the crank are not investigated.

Static Tests

To facilitate unsteady flow comparisons, the model was first tested under static AOA and α conditions. Flow visualization techniques can only illustrate possible aerodynamic benefits of forced unsteady flows when static and dynamic comparisons are accomplished at similar test conditions. However,

since the possible flight advantages of unsteady flows appear to be the reduction of cataclysmic canard stall and the delay of forward swept wing root stall, the static test parameters were chosen to establish geometric conditions where such adverse effects were likely to be produced. Three model angles of attack of 0, 5, and 10 degrees were tested each with nine canard angles of 0 to 40 degrees (Fig. 42A/B). The following figures have been divided into two parts (A/B) of the photographic series to better illustrate flow pattern detail.

When the model centerline is aligned with the freestream velocity (0° AOA), the canard flow characteristics are as shown in column one of Fig. 42A/B. At canard angles of 0° and 5° the flow streaklines appear attached to both canard and wing surfaces. At $\alpha = 10°$ a separation bubble occurs near the leading edge of the canard and the canard wake is more turbulent than at lower α values. The smoke lines show a decreased (approximately 3° to 4°) effective angle of attack on the wing due to the downwash from the canard. As α increases to 15°, the separation region over the canard increases in size, but the overall flow remains attached and the downwash angle increases 2° -3° for a 5°-7° total. The adverse pressure gradient finally causes complete flow separation over the canard at $\alpha = 20°$. This separation is accompanied by an apparent increase in effective angle of attack of the wing. Streaklines passing over the upper surface of the canard clearly convect under the wing.

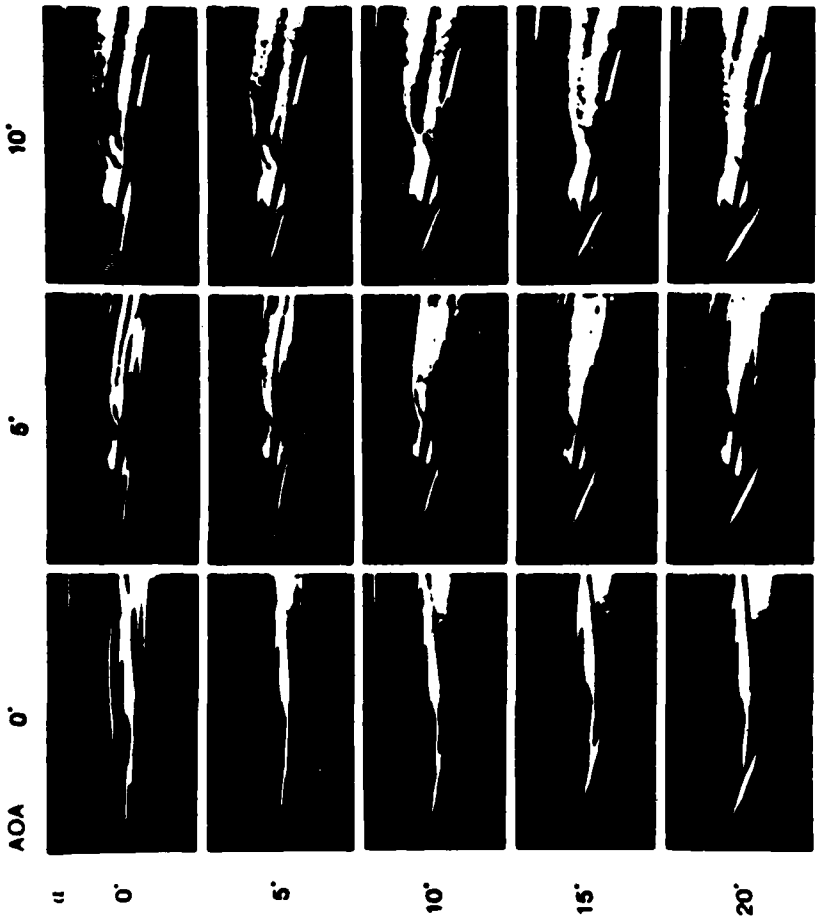

Fig. 42A Static side view photos, AOA = 0° to 10°, α = 0° to 20°.

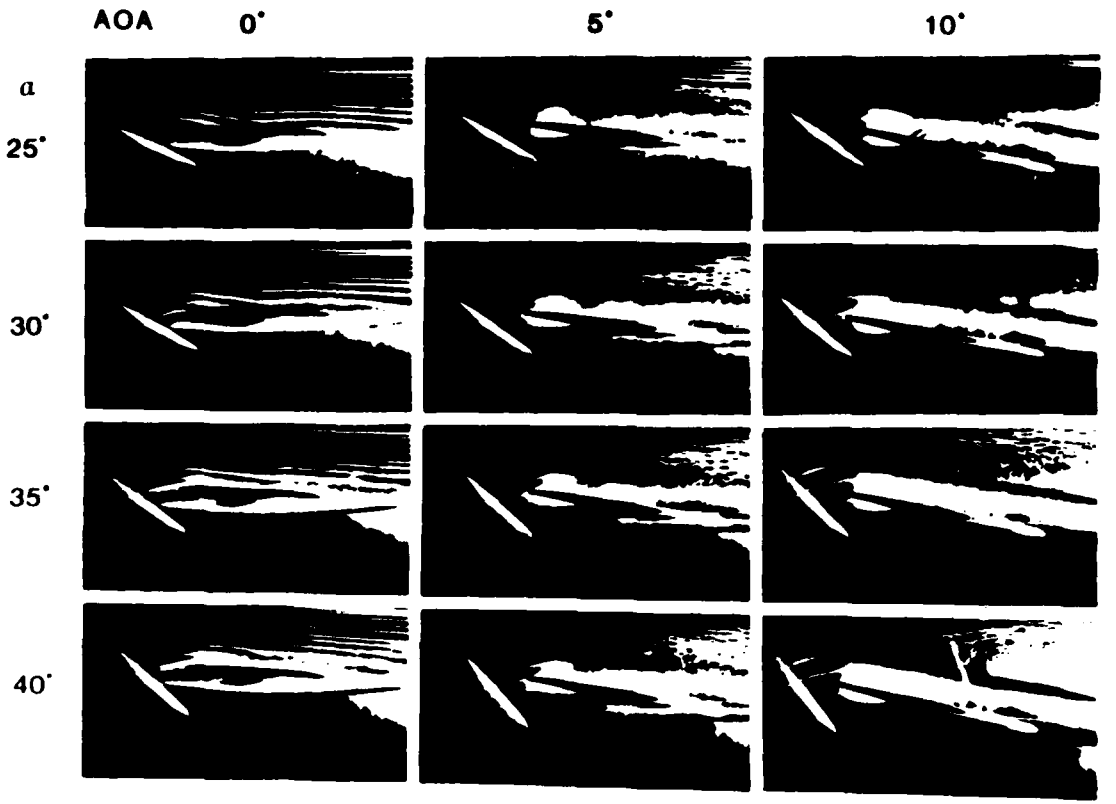

Fig. 42B Static side view photos, AOA = 0° to 10°, α = 25° to 40°.

The smooth, cohesive flow lines over the top of the wing appear attached to the surface and exhibit little apparent turbulence (as might have been shown by numerous, random streaklines and diffuse smoke in the multiple exposure photographs) for canard angles of 0° to 20°. As canard angle increases through 25° and up to 40°, the wake behind the canard increases in size and this turbulent, random streakline region is observed on both top and bottom surfaces of the wing.

Column 2 of Fig. 42A/B shows smoke line patterns about the model at 5° AOA. The wing is at a higher angle of attack and circulation has apparently increased. This increase is demonstrated by flow line differences about both the wing and canard. At 0° canard angle of attack, the geometric canard angle with respect to the freestream is 5°. At this angular position, the top surface flow across both canard and wing appears attached. Flow lines passing under the canard are observed moving upward and over the top surface of the wing. The very low pressure region created on the lifting wing upper surface produces an upwash effect in front of the leading edge. This wing upwash is also shown as an effective angle of attack increase on the canard. Since the model angle is increased 5° from column one, the stall characteristics of the canard would be expected to shift by 5°. This shift , however, is greater than expected and nearly identical canard separation observed in column one at $\alpha = 20°$ occurs in column two at $\alpha = 10°$. As the

canard α continues to increase, the separation region grows and this separated wake completely engulfs the wing at higher α values. At canard angles above 25°, the smoke lines flow around the canard tip. No apparent tip vortex forms suggestive of an absence of any effective pressure difference from one to the other side of the canard.

The photographs in column three of Fig. 42A/B are for model AOA of 10°. Flow separation over the canard initiates even at $\alpha = 0°$. This earlier-than-expected separation again is due to the increased effective angle of attack of the canard produced by wing upwash. The flow over the wing top surface appears more turbulent than in the lower AOA cases. The canard wake flow at high α appears somewhat similar to the 5° AOA case. Flow passing under the canard is again drawn upward over the upper surface of the wing. Similar to the AOA of 5° test, two distinct flow patterns appear over the top surface of the wing. One passes under the canard near the tip and protrudes well above the flow pattern near the upper wing surface. A second, seemingly more inboard flow, passes over the top of the canard and then follows the contour of the upper surface of the wing. Analysis of this three-dimensional behavior is best accomplished with rear view photography.

The complex, three-dimensional flow patterns about the model at 5° AOA are shown from both side and rear views in Fig. 43A/B. Spanwise flow characteristics which produce the

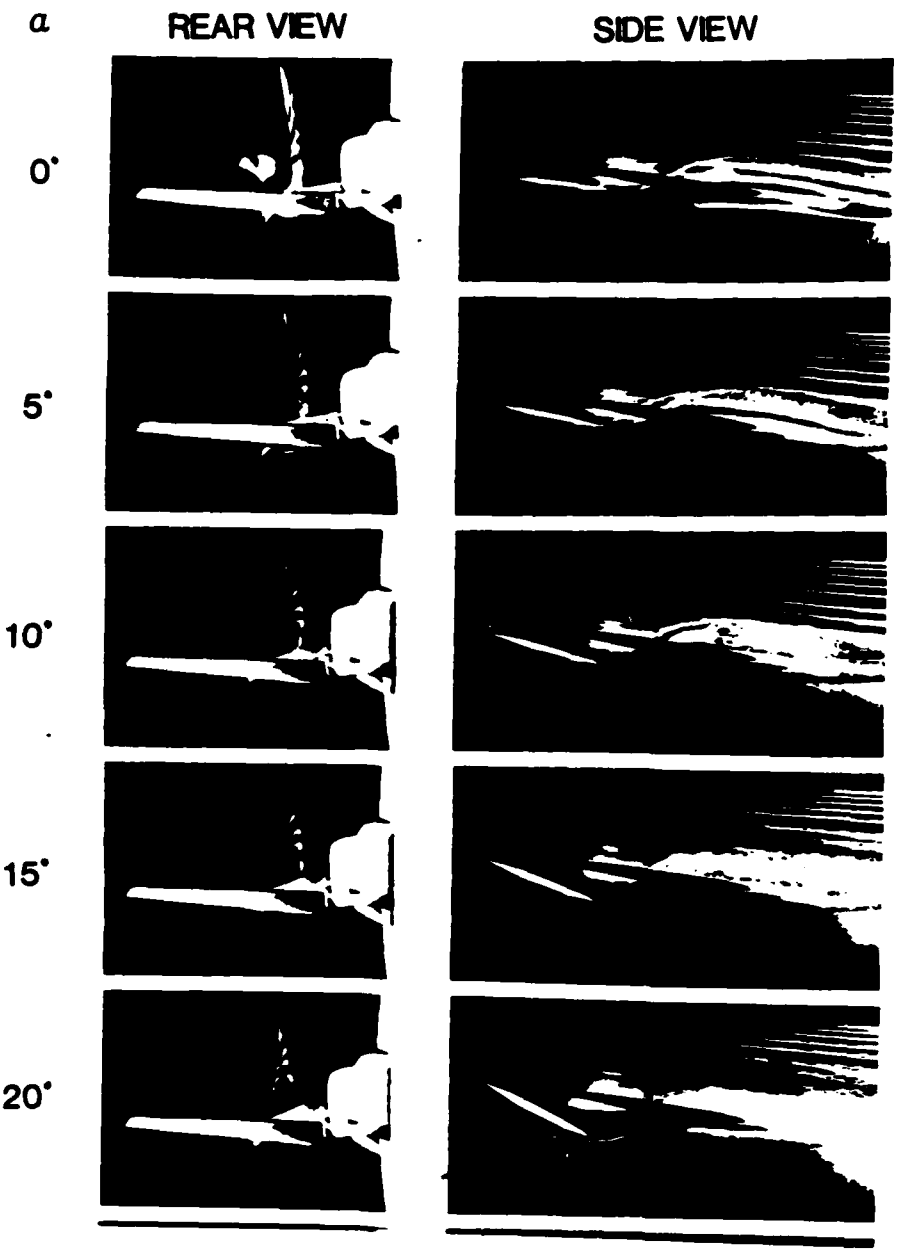

Fig. 43A Static rear and side view photos, AOA = 5°, α = 0° to 20°.

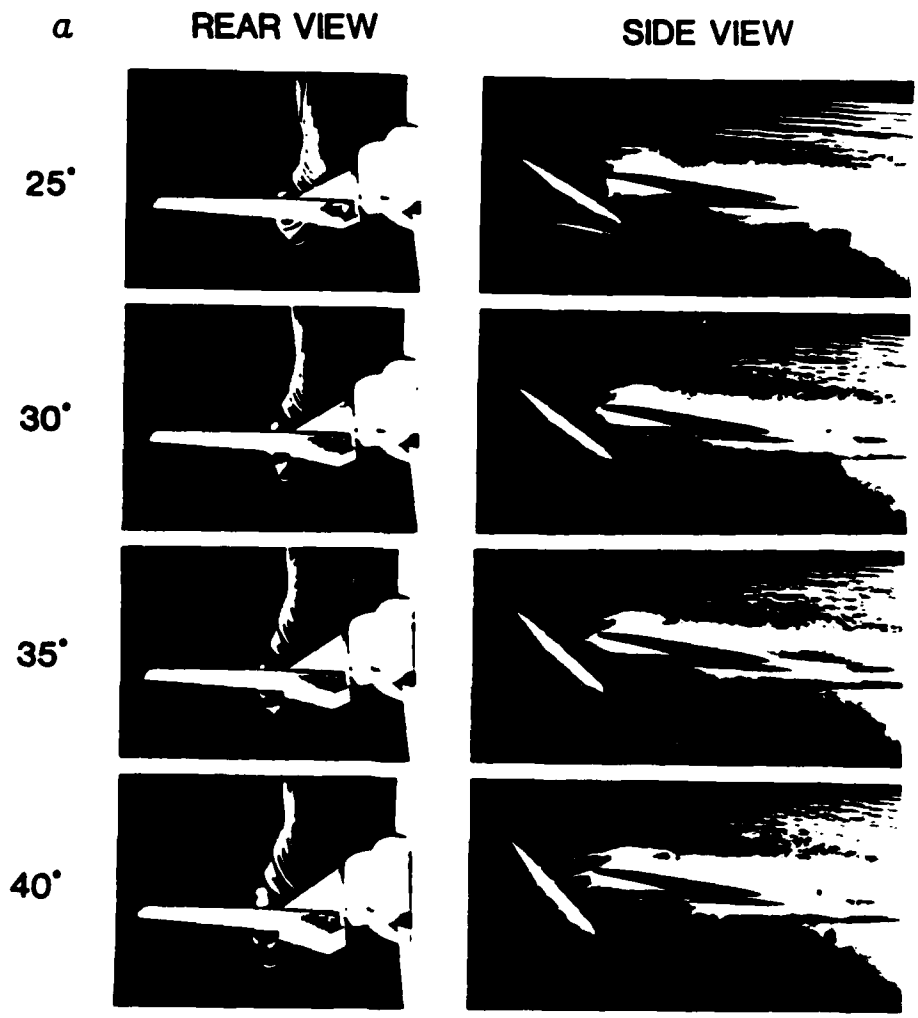

Fig. 43B Static rear and side view photos, AOA = 5°, α = 25° to 40°.

distinctive patterns observed in previous side view visualizations can be seen in the rear view photos for canard angles of 0° to 40°. The horizontal smoke lines which pass with the freestream flow from left to right in the side view photographs are seen as vertically stacked lines flowing toward the camera in the rear view visualizations. At $\alpha = 0°$, the two overlapping side view patterns are caused by spanwise flow differences over top and bottom surfaces of the canard. The smoke lines intercept the canard at midspan. The lower surface flow is drawn outboard by the tip vortex. The smoke is captured into the tip vortex and traces a rotational flow well above the top surface of the wing. Thus, an outboard to inboard rotational pattern is viewed over the wing top surface. The smoke lines passing over the top of the canard remain nearly two-dimensional as they pass over the surface of the canard and wing. At $\alpha = 5°$, a separation bubble begins to form on the canard top surface and the tip vortex appears more turbulent in side view and less distinct in rear view photos. Lower streaklines, not engulfed by the tip vortex, are pulled outboard under the canard and then move upward against the wing lower surface as they traverse under the wing. Similar flow structures exist at $\alpha = 10°$ with a more turbulent tip vortex (shown by a diffused smoke pattern). As α increases to 15°, the canard stall is complete and the tip vortex is nearly undiscernible. Flow passing under the canard is still drawn up toward the wing lower surface. From $\alpha = 20°$ to 40°,

the separation is exaggerated and flow lines can be traced around the canard surface in the rear view photos. The smoke lines are observed to loop outward around the canard and are drawn back toward the wing surface before turbulence dissipates the distinct smoke patterns.

These static investigations illustrate numerous three-dimensional flow characteristics observed in the multiple exposure photographs as changes in smoke line direction and cohesion. Increasing model AOA increased apparent circulation of the wing up to AOA = 10° where the flow shows weak separation tendencies near the root. This increase in AOA also created upwash (approximately 5°) which increased the effective canard angle of attack. Increasing the canard angle of attack from 0° to 40° established canard stall onset angles for each model AOA. Also, increasing canard α increased the canard downwash and decreased effective angle of attack of the wing until canard stall occurred. Before canard stall was complete, the canard tip vortex intensity increased with increasing canard α. These observations establish desired parameter ranges for the dynamic investigations.

Dynamic Tests

Previous experiments have demonstrated lift enhancement characteristics when wing surfaces are oscillated through sinusoidal motions which project the wing above and below normal stall angles. The unsteady flow fields produced by sinusoidally

oscillating the canard of the X-29 model not only influence the immediately adjacent canard flow but also change the dynamic characteristics about the trailing wing. The static model experiments demonstrate flow fluctuations as model AOA and canard α vary. These flow alterations are shown as changes in stall angles, upwash and downwash, effective angles of attack, canard tip vortex appearance, and turbulence levels. To thoroughly comprehend dynamic flow patterns, these variations were examined throughout a complete oscillation cycle. Changes in these flow characteristics and other unique phenomenon are noted as the dynamic pitching cycle varies from $\phi = 0.0$ to 1.0. Where applicable, comparisons are made between static and dynamic results as well as between various dynamic configurations. Flow visualization techniques were employed at different model angles, canard mean angles, canard oscillation amplitudes and reduced frequencies to attempt possible prediction of dynamically beneficial patterns.

Initial experiments were concerned with small amplitude oscillations that might be applicable to the computer controlled canard angular deflections of the X-29 aircraft. Dynamic flow visualizations of small amplitude ($\pm 5°$) oscillations at constant nondimensional reduced frequency, $K = 1.0$, are illustrated in Fig. 44A/B. Since model AOA changes the static stall angle of the canard, the mean angle of attack for oscillation was varied for each AOA during dynamic tests in order to project the wing

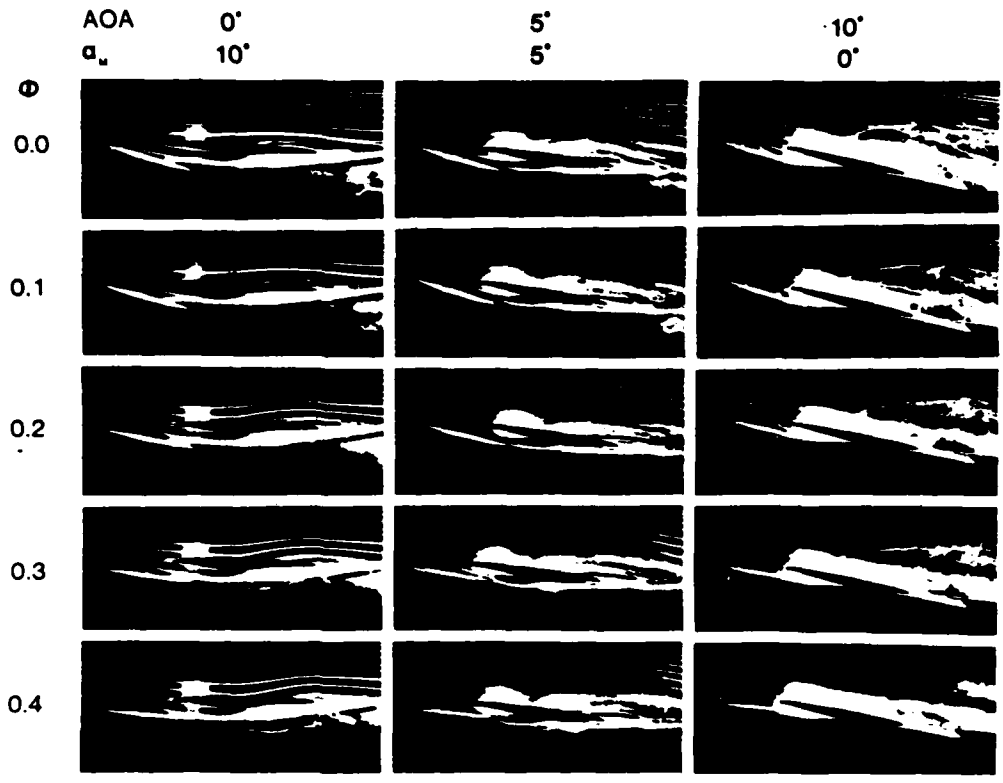

Fig. 44A Dynamic side view photos, K = 1.0, AOA = 0° to 10°, α_m = 10° to 0°, α_ω = ±5°, ϕ = 0.0 to 0.4.

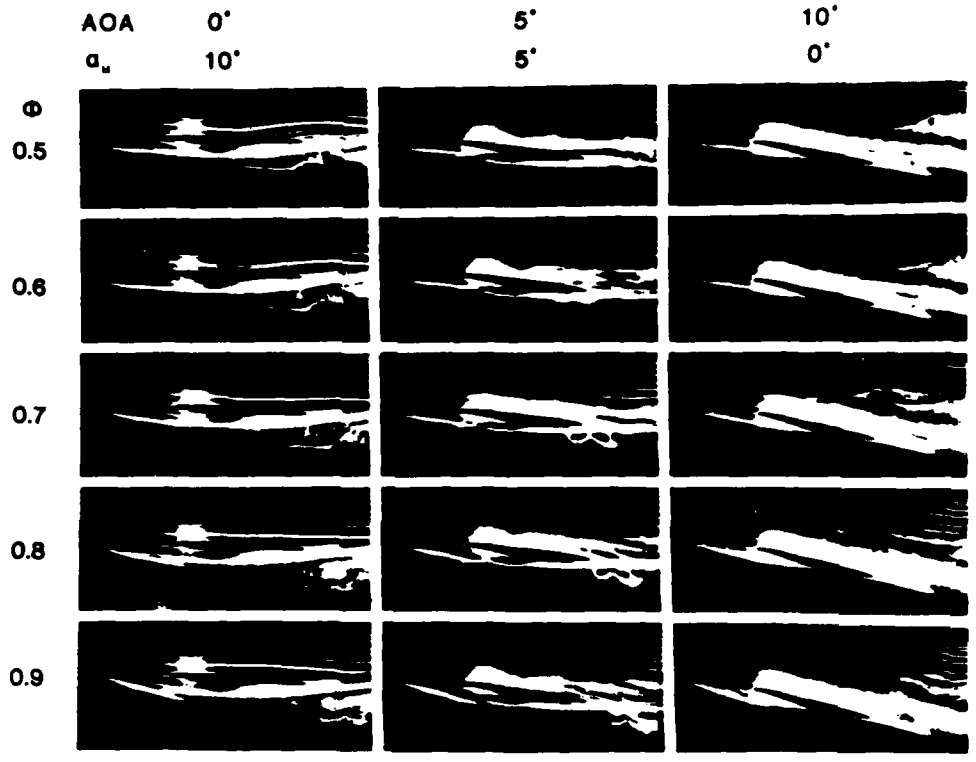

Fig. 44B Dynamic side view photos, K = 1.0, AOA = 0° to 10°, α_m = 10° to 0°, α_ω = ±5°, ϕ = 0.5 to 0.9.

above and below the static stall. As AOA increased by 5° for each test, the mean angle about which oscillations occurred decreased by 5°. Thus, the canard oscillation angles remained constant with respect to the freestream flow.

Column one of Fig. 44A/B shows one complete oscillation cycle for model AOA of 0° and mean angle of 10°. At maximum canard angle of attack, $\phi = 0.0$, the flow lines are attached to both the canard and wing. This same angle of attack used during static tests produced a separation bubble which engulfed the entire upper surface of the canard. At $\phi = 0.1$, a leading edge vortex is discernible on the upper surface of the canard. The canard wake appears more turbulent and downwash from the canard reduces the effective angle of attack of the wing root, possibly even to negative values. As ϕ increases through 0.2 and 0.3, the leading edge vortex increases in size and the turbulence in the canard wake under the wing surface increases. The downwash from the canard and attached flow over the wing are verified by the bending of those smoke streaklines well above and remote to each surface. These streaklines bend upward reflecting disturbances in the mean flow created by the two control surfaces and bend downward between the two surfaces when the greatest downwash is observed. This bending of the streaklines located well above the X-29 surfaces was also seen to be correlated with downwash during the static tests.

At $\phi = 0.4$, the canard leading edge vortex appears to

have traversed slightly aft of the leading edge. Wake flow behind the canard has formed a downward protruding region under the surface of the wing. This flow moves downward, away from the wing, at the leading edge and, moves back up toward the wings surface near the trailing edge. When compared with the freestream velocity and temporal angular motion of the canard, the horizontal length of this protruding region is that which the airflow travels in one-half cycle of the canard oscillation. Therefore, this region appears formed by the canard wake during the portion of the cycle when the trailing edge of the canard is lowest and the canard downwash is greatest. When the minimum canard angle of attack is reached, the downward protruding region terminates and the forward edge of this region begins to traverse aft under the wing.

At ϕ = 0.5, the leading edge vortex is dissipating on the canard surface much like the three-dimensional vortex dissipation observed during other finite wing experiments. From ϕ = 0.6 to 0.9, the canard is pitching upward toward maximum angle of attack. The leading edge vortex has dissipated into a viscous shear layer. The canard downwash decreases during this portion of the cycle and is evidenced by the straighter, more horizontal flow lines seen well above the canard and wing surfaces. Although the downwash fluctuated during the pitching cycle, the flow remained attached to the canard surface throughout with disturbances only for the high energy leading

edge vortex structure. Similar to static tests at this AOA, smoke from the midspan region was not drawn outboard to mark the canard tip vortex.

Column two of Fig. 44A/B shows one oscillation cycle for model AOA of 5° and mean angle set at 5°. The wing increased circulation is verified by the upwash affecting the smoke flow over the canard and wing surfaces. Much like static tests at this AOA, the canard tip vortex flow is marked by smoke from the midspan region and is being pulled up over the top surface of the wing. This indicates three-dimensional effects on the canard which cause the lower surface smoke flow to be trapped by the tip vortex and trace this swirling pattern about the wing surface. The canard downwash does not appear as dominate as in the lower AOA test.

A distinct leading edge vortex is observed on the canard at $\phi = 0.0$. The static data at similar instantaneous model and canard angles shows a stalled region over the entire canard top surface. Through $\phi = 0.3$, the leading edge structure remains fixed near the canard leading edge and the flow is attached to the surface aft of the vortex. At $\phi = 0.4$, the leading edge vortex decreases in size and begins to traverse aft. When ϕ is 0.7, the leading edge vortex is a small, more turbulent structure near the trailing edge of the canard. At $\phi = 0.8$, a new leading edge vortex is beginning to form and the previous structure is visible only as a diminutive streakline disturbance at the

trailing edge of the canard. Near the end of the pitching cycle, ϕ = 0.9, a new canard leading edge vortex is forming while the previous vortex has shed from the trailing edge. Canard leading edge vortex passage about the wing surface is not observed at this test condition.

The downwash from the canard that passes under the wing at this AOA appears spatially and temporally influenced by the upwash from the wing. The downward protruding region of flow under the wing surface is clipped shorter in streamwise length and has less downward spatial depth than lower AOA data. A three-dimensional spanwise effect has been imparted to this region causing a lobe-like formation seen clearly at ϕ = 0.7. This lobe-forming characteristic is less pronounced at lower AOA values.

An increase in model AOA to 10°, column three of Fig. 44A/B, increases dynamic spatial characteristics of the flow about the canard and wing. The wing upwash has increased. This is evidenced by the streakline smoke flow well above the surfaces, the early formation of the leading edge vortex in the pitching cycle and the continuous three-dimensional canard tip flow up over the top surface of the wing. The smoke streamlines passing well above the surfaces show canard downwash by bending down toward the canard trailing edge only during maximum α values. A leading edge vortex structure is observed on the canard surface throughout the pitching cycle. A strong leading

edge vortex is forming and enlarging from ϕ values of 0.0 to 0.3. From ϕ = 0.4 to 0.6, this vortical structure appears to move slightly aft on the canard surface. At ϕ = 0.7, the vortex is shed from the trailing edge and the flow collapses toward the top surface of the canard. A new leading edge vortex is forming at ϕ values of 0.8 and 0.9. Similar to unstalled canard flows seen in static tests, the canard tip vortex creates a three-dimensional swirl flow passing well over the top surface of the wing throughout the pitching cycle. Disturbances on the top surface of the wing are cyclic and exact analysis of their cause is difficult due to a possible near stall condition of the wing at this high AOA. As observed in previous static tests of this model, most flow passing immediately around the canard traverses over and not under the wing at this high AOA value. Further analysis of dynamic flow characteristics at these AOA values is accomplished by increasing the oscillation amplitude from ±5° to ±10.°

Fig. 45A/B mirrors Fig. 44A/B in all dynamic conditions except oscillation amplitude. In Fig. 45A/B, the canard pitching angle of attack varies ±10° from the mean angle. Column one at 0° AOA demonstrates characteristics similar to equivalent AOA data from the previous figure. The smoke streaklines well above the surfaces indicate the canard downwash. This canard downwash creates a downward protrusion under the wing with slightly greater spatial depth below the wing surface due to the larger

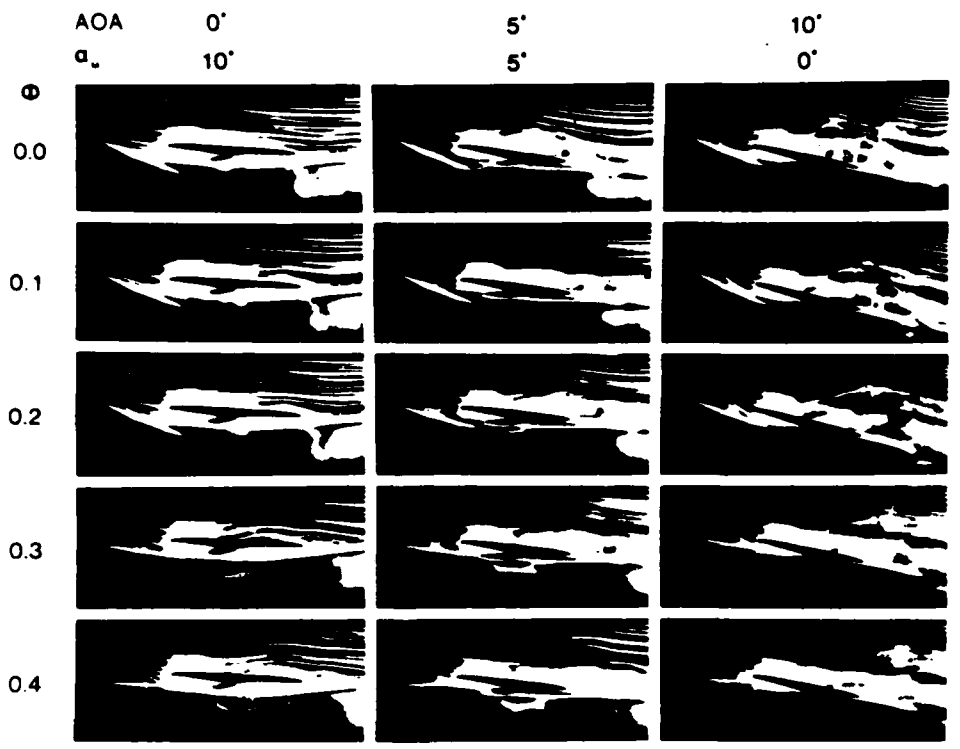

Fig. 45A Dynamic side view photos, K = 1.0, AOA = 0° to 10°, α_m = 10° to 0°, α_ω = ±10°, ϕ = 0.0 to 0.4.

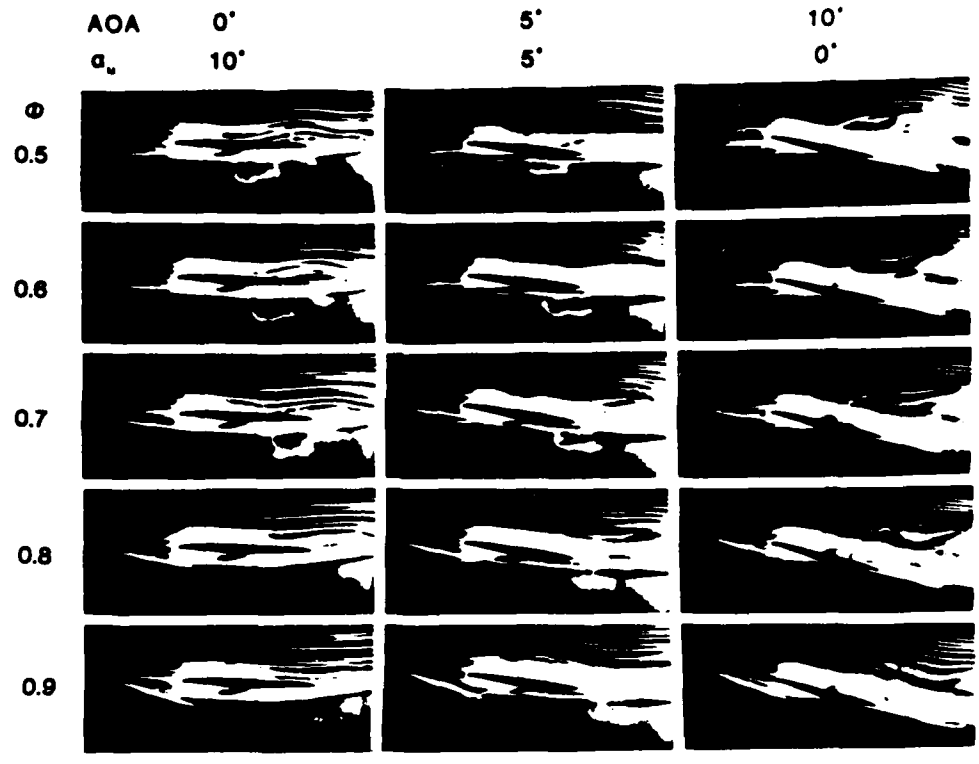

Fig. 45B Dynamic side view photos, K = 1.0, AOA = 0° to 10°, α_m = 10° to 0°, α_ω = ±10°, ϕ = 0.5 to 0.9.

downward motion of the trailing edge of the canard. The leading edge vortex forms at ϕ values identical to those showing vortex formation at lower amplitude oscillations. However, these vortex structures exhibit more rapid convection as evidenced by the shedding from the trailing edge during the latter portion of the pitching cycle. A cyclic disturbance can be seen passing over the top surface of the wing and is more easily observed in higher AOA tests.

The oscillation motion recorded in column two carries the canard through a maximum geometric angle of 15° and a minimum angle of -5°. Again, the smoke streaklines well above the surfaces show canard downwash and wing upwash. The significant differences noted between this column and column two from the previous figure are the top and bottom surface flows over the wing. The bottom surface protrusion forms under the wing as before, however, the forward portion is drawn into a three-dimensional, clockwise-rotating vortex (ϕ= 0.6). This vortex is formed when the protrusion is clipped by the upward motion of the canard trailing edge.

The top surface flow over the wing appears to be influenced by both a leading edge vortex from the canard and an upward protrusion caused by upwash from the canard at minimun angle of attack. At ϕ = 0.6, the canard has begun the increasing angle of attack phase of the oscillation cycle and a diminished-size leading edge vortex has traversed to near

midchord. As increased α progresses to $\phi = 0.7$, the leading edge vortex is nearly shed from the trailing edge of the canard and an upward disturbance is forming near the wing leading edge. At $\phi = 0.8$ and 0.9, the leading edge vortex is completely shed from the canard and the upward disturbance is traversing the wing. When maximum α is reached at $\phi = 0.0$, the flow is reversing from under-the-canard/over-the-wing to over-the-canard/under-the-wing. This switch clips the upward protrusion. From $\phi = 0.0$ to 0.2, a nearly circular vortex with upstream elongation is observed traversing the wing upper surface.

Column three of Fig. 45A/B depicts canard angular motions of $\pm 10°$. The flow characteristics shown here are temporally identical and spatially of somewhat greater magnitude than data for the lower amplitude oscillations. Leading edge vortex formation, size and convection appear unchanged from column three of Fig. 44A/B. The three-dimensional canard tip vortex swirl over the wing top surface, seen only at high α in column two, is observed throughout the pitching cycle. The wing upper surface flow is visually more prominent than in column two. At $\phi = 0.7$, the leading edge vortex is shedding from the canard trailing edge and an upward disturbance is beginning near the leading edge of the wing. When $\phi = 0.9$ and 0.0, the vortex/protrusion is fully developed on the top surface of the wing. As in other high AOA tests, nearly all smoke flow about the canard traverses above the wing. However, at $\phi = 0.9$, 0.0 and 0.1, a lower surface

protrusion is observed indicating this flow characteristic occurs at high AOA.

The effects of reducing K value from 1.0 to 0.5 can be seen by comparing the previous data with photos in Fig. 46A/B. In Fig. 46A/B, the model AOA and mean angle of attack are both set at 5°. The oscillation amplitude is ±5°, ±10° and ±20° in columns one, two and three, respectively. An initial analysis of this data reveals four overall observations. First, the smoke lines passing near any control surface are more turbulent than for the higher K value cases. There also appears to be little if any canard tip vortex flow up over the top surface of the wing. The leading edge vortices formed on the canard surface cyclically grow in size then dissipate, with no apparent effect on the flow over the top surface of the wing. And finally, all the unsteady flow patterns seem directly related only to the cyclic upwash and downwash created by the canard oscillating motion.

Column three of Fig. 46A/B provides a pictorial summary of the upper and lower wing surface protrusions caused by the cyclic canard upwash and downwash. A leading edge vortex forms during the increasing α phase at $\phi = 0.9$. This vortex grows during the decreasing α phase from $\phi = 0.0$ to 0.2. The leading edge vortex, however, decreases in size and dissipates without showing convective tendencies as ϕ goes from 0.3 to 0.5. The upper and lower protrusions are caused only by the cyclic upwash and downwash changes. From $\phi = 0.0$ to 0.3, the wing surface is

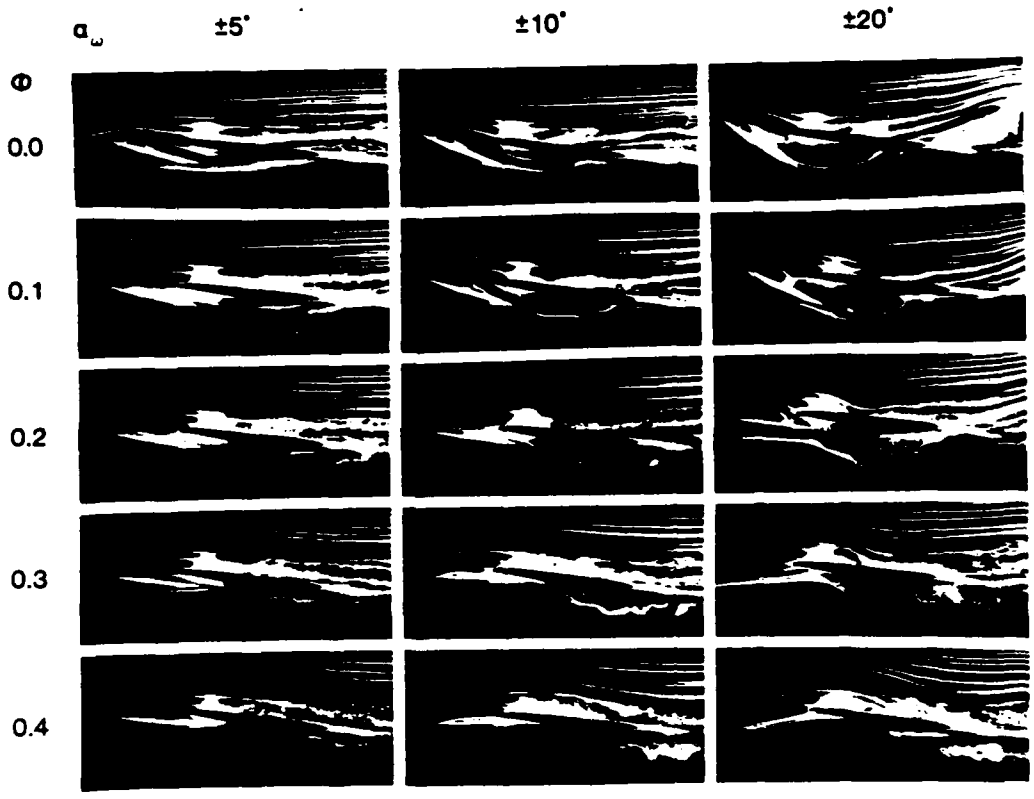

Fig. 46A Dynamic side view photos, K = 0.5, AOA = 5°, α_m = 5°, α_ω = ±5°, ±10° and ±20°, ϕ = 0.0 to 0.4.

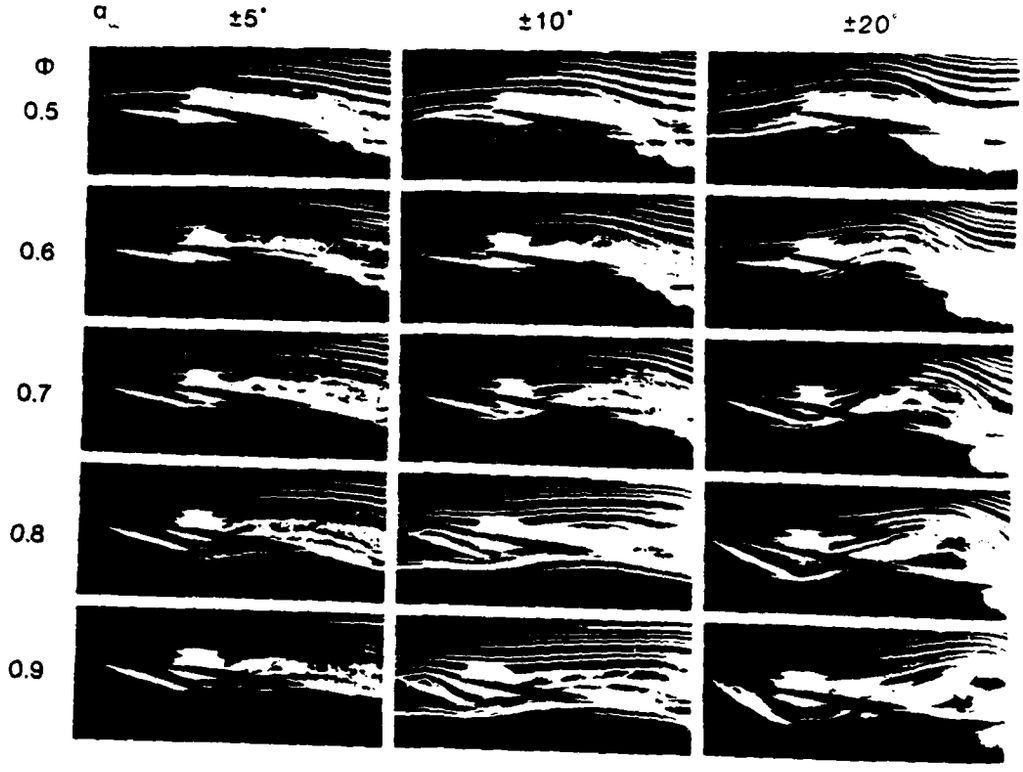

Fig. 46B Dynamic side view photos, K = 0.5, AOA = 5°, α_m = 5°, α_ω = ±5°, ±10° and ±20°, ϕ = 0.5 to 0.9.

dominated by the lower surface protrusion. The maximum angle of attack of the canard during this phase causes maximum downwash and under-the-wing flow. The ϕ = 0.5 to 0.8 phase immediately follows the minimum angle of attack in the cycle and, with allowances for streamwise smoke travel, shows domination of the wing flow by the upper surface protrusion.

Nearly all data analyzed thus far has been described as containing various degrees of three-dimensionality. To facilitate analysis of the three-dimensional effects, rear view photographs were taken at K = 1.0, AOA = 5°, mean angle = 5° and oscillation amplitude of ±10°. The rear and side views at identical dynamic conditions are shown in Fig. 47A/B. The rear view photographs do not contain the entire flow pattern over the surfaces due to lighting and camera focal length restrictions. Since the area of significant flow description is just forward and aft of the canard trailing edge, this horizontal surface is used for camera focus. The smoke flow patterns proximal to the canard trailing edge will appear most prominent in the photographs.

At ϕ = 0.0, the smoke lines passing about the canard and wing surfaces demonstrate the complex three-dimensionality of this flow. Similar to static rear view data, the smoke is pulled out of the original vertical plane by dynamic spanwise pressure gradients and downwash and upwash effects. The smoke flow over the canard appears reasonably two-dimensional as it convects

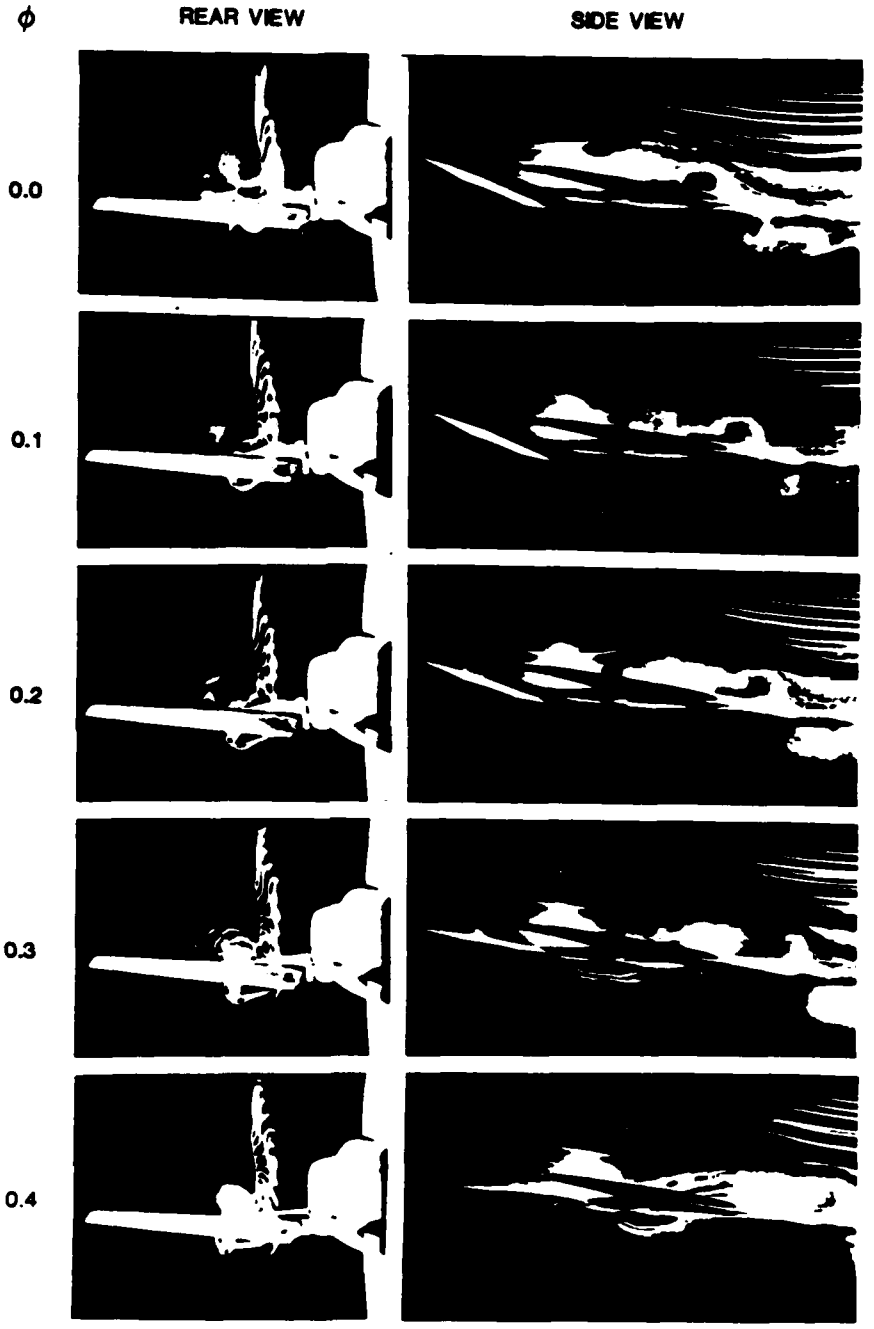

Fig. 47A Dynamic rear and side view photos, K = 1.0, AOA = 5°, $\alpha_m = 5°$, $\alpha_\omega = \pm 10°$, ϕ = 0.0 to 0.4.

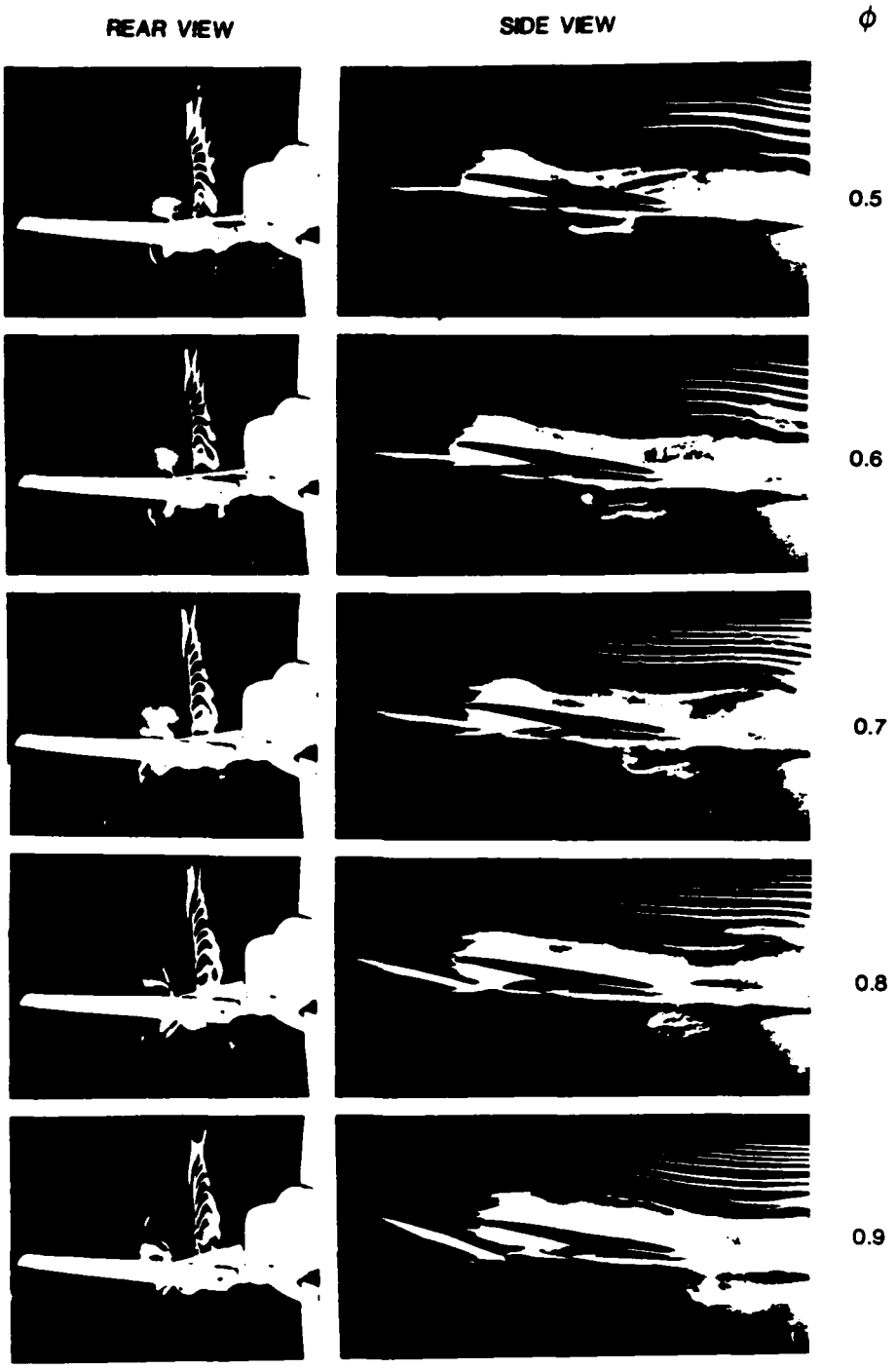

Fig. 47B Dynamic rear and side view photos, K = 1.0, AOA = 5°, $\alpha_m = 5°$, $\alpha_\omega = \pm 10°$, ϕ = 0.5 to 0.9.

across the canard and wing surfaces. The smoke flow under the canard is pulled from left to right toward the canard tip. This smoke is entrained in the canard tip vortex and traces the swirling pattern upward and well above the wing upper surface. The rear view visualization shows this vortex pattern as a vertical line extending upward from the canard tip with a circular smoke pattern above the wing.

For ϕ = 0.1 and 0.2, the rear view flow patterns are similar to that observed at ϕ = 0.0. The flow under the canard is drawn farther away from the lower surface as left-to-right flow toward the tip continues. A canard tip vortex is still observed with the vortex center moving closer to the surface of the wing as ϕ increases. A slightly three-dimensional leading edge vortex can be seen from the rear as a vertical disturbance on the canard surface.

As ϕ increases through 0.3 to 0.6, the rear view canard tip vortex moves even closer to the wing surface and a decrease in apparent strength is indicated by a decreasing smoke diameter around the vortex center. The left-to-right spanwise smoke flow under the canard moves farther away and then closer to the canard lower surface. This characteristic, accounting for flow temporal delay for traversing velocity, is the flow moving around the canard surface at the high α portion of the pitching cycle then moving closer during low α. Another smoke trace is also now observed under the wing surface in vertical line with the

original smoke flow. This trace originates above the canard and indicates the spanwise location of the lower surface protrusion. At $\phi = 0.6$, this trace near the wing root position becomes very clear. The corresponding side view shows a distinct rotating vortex at this position. The remaining cycle, $\phi = 0.7$ to 0.9, illustrates an increase in canard tip vortex strength and dissipation of the under-wing vortex core.

Similar to static tests, the visualized flow characteristics of stall angles, of upwash and downwash, of effective angles of attack, of canard tip vortices and of turbulence levels were documented for the cyclic dynamic flow tests. Unique dynamic characteristics of canard leading edge vortex development and wing protrusions were also recorded. Changes in dynamic test parameters precipitated distinct alterations in these flow characteristics. Increases in model AOA stimulated an increase in wing circulation which lead to higher effective angles of attack of the canard. This angular increase is demonstrated by more spanwise flow toward the canard tip and earlier formation and larger size of the canard leading edge vortex. Increases in canard mean angle of attack increased overall downwash from the canard which decreased the effective angle of attack of the wing root. Changes in oscillation amplitude created the protrusion effect over the wing by changing the upwash and downwash patterns. Reducing the nondimensional reduced frequency, K, produced more turbulent flows and virtually

eliminated any convective tendencies of the canard leading edge vortex. These overall dynamic characteristic changes when viewed simultaneously may illustrate beneficial flow patterns.

CHAPTER VIII

DISCUSSION

Throughout the studies discussed in this text, many unique observations concerning unsteady flow behavior have been made. Some confirm hypotheses generated by previous investigations and others, such as the X-29 results, are unparalleled in experimental research. Unsteady flow characteristics about three-dimensional, finite wings are not fully understood. Therefore, a systematic approach has been undertaken in the present analysis to comprehend the finite wing interactions as well as the effects of swept surfaces. This basic finite, swept wing analysis is essential in unsteady flow application attempts with models like the X-29. Since different experimental investigations produced distinct levels of comprehension, each will be discussed separately.

Forward Swept Wing

The initial finite wing studies began with flow visualization experiments on a forward swept wing. The three-dimensional flow field dynamics about a finite wing cannot be completely described using flow visualization techniques alone, however, these investigations provide comprehensive qualitative

insight into spatial and temporal flow characteristics. The swept forward wing yielded unsteady separated flow fields that in many ways were reminiscent of those three-dimensional flows elicited by a symmetric wing (Adler and Luttges, 1985). Of critical comparative importance was the failure of tip vortices to decrease in apparent strength at very high angles of attack. The stalling characteristics were similarly critical. The inboard regions of the span stall at lower angles of attack than the tip regions. These static angle of attack dependencies undoubtedly contributed to the dynamic pitching characteristics exacted on the flow field.

The effects of K values and mean angles of attack on inboard, leading edge vortices were well behaved. With increased K these vortices formed later in the upward pitching motion and with increased mean angles of attack the vortices were formed earlier. Vortex initiation point was correlated with V_c in that earlier initiation invariably led to lower V_c values and later initiation, to higher V_c values. Apparent vortex size was inversely related to the V_c values.

At the wingtip, the curvature of flow inboard was determined both by angle of attack and by the presence or absence of a leading edge vortex. As the wing pitched through a complete cycle, the wingtip flow curvature showed significant amounts of hysteresis and significantly more magnitude than observed during static angle of attack tests. The hysteresis was most

clear during low K value tests and the overall magnitude of curvature was most obvious using high K values.

The interaction between these flow patterns was spatially dependent upon span location and temporally dependent upon pitching characteristics of the wing. In the former case, flows near the tip over the wing developed more slowly than inboard flows. The resulting vortices were more capricious, the apparent V_c values smaller, and vortices disappeared before reaching the trailing edge. As a result of higher K values, vortex flows near the tip were delayed in the pitching cycle to initiation at higher angles of attack and the apparent vortex size (small in comparison to inboard vortices) was increased. At high K values, the primary vortex was joined by additional vortices during a single pitching motion. Planform plots reveal two disparate regions on the upper surface of the wing that are the domains of leading edge vortices or tip vortices, respectively. The leading edge vortex domain consists of a triangular wedge with the base far inboard and the apex near the leading edge of the wingtip. One side of the wedge is outlined by the leading edge of the wing and the other side is generally bounded by a line beginning at the trailing edge inboard and running toward the front of the wingtip. In contrast, the domain of the tip flow structures is a wedge shaped area bounded by the tip and by a line beginning from the leading edge of the tip and passing to the trailing edge of

the wing where a base is formed. Between these domains remains a place on the wing where flow field structures arise from the interactions of the leading edge and wingtip vortices. The most predominant of these structures are shear layers both with and without distinct embedded multiple vortices. Interactions occur between the domains outlined but such interactions appear to affect the magnitude of existing flow field structures rather than the qualitative nature of the flow fields. Thus, the wingtip domain is characteristically that of the wingtip vortex where inboard flow changes the β angle but not the overall flow field. And, the leading edge vortex domain shows a vortex that responds to tip flow but this vortex is not lost to the tip flow effects.

The specific contributions of the swept forward wing to the three-dimensionality of the flow field during pitching appear to arise from a combination of the inboard stalling characteristics of the wing at high angles of attack and the reluctance of the tip to show stall at such high angles. In addition, the two flow field domains described above interact in a non-orthogonal fashion due to the forward sweep of the wing.

The result of these swept forward wing interactions is most evident in the growth of the leading edge vortex near the wingtip. Unlike previously reported instances in which increases in K value result in decreased vortex sizes, the vortex size near the wingtip actually increases with increased K values. In fact,

this relationship only exits in flow regions near the wingtip and further inboard the size of the leading edge vortex behaves as it does using airfoils. Coupled with this observation is the alteration in the character of the helical tip vortex. The vortex shows exaggerated β angles across all dynamic test conditions but the exaggeration is neither as large nor as influenced by hysteresis as in tests using a straight symmetrical wing.

Swept and Straight Wings

When tested under identical static and dynamic conditions, the FSW, STW and ASW yield different flow separation characteristics. Major differences between these wings appear to derive from spatial variations in the static separation and from the spatial and temporal distribution of vorticity related to forced dynamic separation conditions. In static testing, the FSW first began to indicate flow separation characteristics near the wing root as angle of attack was increased. Similar separation tendencies developed near midspan locations only as higher α values were tested. This stall characteristic was shared by the tip flow deflection angle, β, which increased steadily with increasing α signifying little stall influence at the wingtip.

The STW shows stall across most of the wingspan at values near 12°. Above this α, the β values drop off reflecting the influence of the stalled wing region inboard.

Separation characteristics were first noted on the ASW near the wingtip as α was increased. This is reflected as steadily decreasing β values as α is increased even more and as inboard stall becomes more fully developed.

These differences in static tests appear to provide the basis for most of the differences between the wings when subjected to dynamic pitching tests. A spanwise comparison of static and dynamic results indicates a direct relation between static stall magnitude and dynamic leading edge vortex size. The FSW stalls first near the wing root and this region shows the largest leading edge vortical structures during dynamic testing. The ASW, however, stalls more readily near the wingtip. Accordingly, this area develops the largest dynamic vortex.

Except for the FSW, the average dynamic β values are consistently higher than the static α counterparts. This is due to the leading edge vortex influence at the wingtip. When a leading edge vortex is present on the wing upper surface, the low pressure vortex and overall attached flow cause higher average β angles at the tip. All β hysteresis loops for $K = 1.0$ are at minimum values at instantaneous $\alpha = 12°$ during the upstroke of the pitching cycle. This point in the pitching cycle coincides with the shedding of the inboard leading edge vortices into the wake. At $\alpha = 12°$, no major leading edge vortical structures are evident on the top surface of the wing.

The wing sweep effects are most dramatically illustrated

in the spatial distribution of the leading edge vortices. As the wing sweep angle progresses from forward to aft, the leading edge vortex dynamics are clearly less dominated by the wingtip flow effects. A strong leading edge structure is observed on the ASW at span locations very near the wingtip, but in the FSW tests these vortices are spatially supported only at quite inboard span locations. These vortex initiation site differences suggest that as the wing sweep increases aft, more vorticity may be generated on the wing top surface to resist the wingtip effect. The vorticity accumulation sites are predicted by the static data. The static cataclysmic stall characteristics near the wingtip for the ASW identify this area as producing the pressure gradient, shear layer and potential flow interaction which produces large scale leading edge vortex structures during dynamic oscillation. The FSW, however, demonstrates minimal stall characteristics near the wingtip during static tests and little, if any, vorticity accumulation in this area during dynamic tests. The resulting vortices reflect differences both in the sites of vortex formation and in the apparent development of the vortices.

A comparison of spanwise centers of leading edge vortex cores can also be made to those observed for linearly accelerated flow tests. The spanwise vortical structures form nearly parallel to the leading edge of each wing and convect in a pattern dependent on wing geometry. These patterns are

reminiscent of those in the stained boundary layer flows in accelerated flow tests (Freymuth, et. all, 1986). Under these conditions, the structures originate at the leading edge of the wingtip and extend across the span of the wing.

Of particular note in the characteristic formation and convection of the leading edge vortex are the dynamic consequences related to the second vortex shedding from the wing trailing edge. In numerous test cases, when the second vortex that formed near midchord sheds from the top surface, the leading edge vortex decreases in apparent size and a dominant shear layer develops on the top wing surface. This shear layer sometimes completely engulfs the leading edge structure. The loss of focused vorticity from the wing top surface that apparently occurs with second vortex shedding, causes the remaining leading edge structure to dissipate into the strengthened distributed shear layer. In cases where larger, more developed leading edge vortices exist, the shear layer is not evident and the leading edge structure successfully traverses the whole wing chord. These latter characteristics are much like those demonstrated in two-dimensional airfoil tests.

An increase in K seems to deposit more or more focused vorticity to the top surface of the wing. At K = 1.4, not only leading edge vortices but also second and sometimes multiple vortices are formed on the top surface at the beginning of the pitching cycle. When multiple structures are formed, the

leading edge and second vortex structures often coalesce early in the downstroke of the pitching cycle. When only two structures exist on the surface, a division occurs: the leading edge vortex divides into a smaller leading edge structure and a larger, more turbulent downstream vortex. The three distinct vortices then separately convect over the wing chord and shed from the trailing edge.

Anemometry Comparisons

Since size, strength and position of vortical structures are somewhat difficult to precisely measure using visualization alone, hot wire anemometry was used to verify and extend the visualization results. The chordwise and spanwise hot wire investigations reveal predictable velocity distributions which correlate well with flow visualization analysis of the unsteady flow field. Previous anemometric measurements obtained by Robinson and Luttges, 1984, for velocity perturbations in and about leading edge vortices formed on airfoils show reliable spatial velocity fluctuations consistent with passage of the vortex. Maximum velocities were observed with the hot wire probe tangent to the vortex circumference. Probe positions localized within the vortex center or core show velocity minimums. Identical fluctuation characteristics of vortex passage signatures were observed and documented in these experiments. A chordwise investigation depicts high local velocities when the

probe is positioned tangential to the edge of the leading edge vortex. As the probe is positioned near the center of the vortex core, measured velocity decreases to a minimum. The local velocity plots verify leading edge vortex relative strength at the measured positions.

The complete velocity profiles show very high repeatability of the velocity fluctuations. Each of the two complete oscillation cycles across ten consecutive trials show very similar velocity characteristics. These profiles confirm the occurrence of high peak velocities when the anemometer probe is nearly tangent to the vortex circumference. When the leading edge vortex center and hot wire probe position spatially coincide, minimum velocities are observed. As the leading edge vortex grows larger and convects downstream, the magnitude of the velocity peaks recorded at aft hot wire probe positions decreases. This trend is verified by previous observations and by potential and viscous flow theory (Schlichting, 1968). Thus, the observed local velocity profiles graphically illustrate the time history of leading edge vortex development and convection as observed during previous flow visualization tests.

The velocity and β angle comparisons over one complete oscillation cycle illustrate flow field dynamics near the wingtip for each wing sweep test configuration. In all cases, the velocity and β angle trends are coincidental throughout the pitching cycle. The wing-geometry-dependent continuation of

these wingtip velocity trends to inboard sites along the span is quite consistent. The FSW wingtip velocity trends are observed inboard as far as S = 0.67c. Flow visualizations, similar to column one of Fig. 36, show a viscous layer in this area by random streaklines in a very thick turbulent boundary layer. This shear layer prevents vorticity from accumulating near the leading edge into a large scale, rotational leading edge vortex. This characteristic may be due to the strong spanwise flow from wingtip to wingroot for a FSW. This span-directional flow may prevent the chordwise reverse flow of vorticity toward the leading edge. Therefore, the coalescence of small, possibly turbulent, vortices into the large scale leading edge structure apparently is disrupted.

Wingtip velocity trends were observed for the STW inboard only until S = 0.33c, and for the ASW only at the forward chord positions even at the wingtip location. The flow over the STW shows little, if any, span-directional flow perseverance inboard from the wingtip vortex dominated region, S = 0.00c to 0.33c. Flow visualizations document the formation of a small leading edge vortex at S = 0.33c but no chordwise convection of this structure occurs. At phase angles approaching the minimum angle of attack, this structured leading edge vortex dissipates into a shear layer that dominates the entire STW chordlength. The ASW exhibits spanwise flow from the wingroot toward the wingtip. This fluid motion resists the inboard flow produced near the

wingtip by the wingtip vortex. Vorticity appears to be accumulated into a structured leading edge vortex on the ASW surface at spanwise points proximal to the wingtip. These structures are observed by both anemometry and flow visualization.

As mentioned previously, the FSW and ASW geometries produce spanwise fluid motion along the top surface. The minimum pressure line for each wing runs roughly parallel to the wing leading edge. Since the airflow is not orthogonal to this line, some span-directional velocities are produced. This characteristic can be verified using incompressible, constant viscosity, Navier-Stokes equations of motion (White, 1974). The spanwise flow promotes different stall characteristics for the FSW and ASW. These regional separation characteristics visualized for each wing during static tests predict spanwise areas of large scale vorticity when oscillating pitch motions are applied to the wings.

The spanwise investigations depicted photographically and graphically show sweep angle effects as well as wingtip and leading edge vortex interactions. Local velocities near the wingtip are normally lower than those recorded at more inboard locations at the same chord position. This verifies the suppression of vortex-structured vorticity near the wingtip. The fluid flow near the wingtip for the ASW quite effectively resists wingtip effects and higher local velocities are observed in this

region. The complete velocity profiles over two oscillation cycles accurately show wingtip effect and leading edge vortex position and strength at any observed span location.

Changes in vortex structure and velocity strength caused by different K values are nominal when compared to wing geometry effects. The range of K values investigated, K = 0.6 to 1.4, produced predictable gradients in leading edge vortex position and strength related to pitch cycle. The velocity maxima and minima for the K = 1.4 experimentr were only noticeable larger than those for other K values at chord locations of approximately midchord.

The extensive flow visualization and hot wire anemometry data together with two-dimensional flow characterizations may now be used to analyze the three-dimensional fluid dynamics about unsteady wings with varying sweep geometries. Analysis of the dynamic stall process on unsteady two-dimensional airfoils has been documented (Reynolds and Carr, 1985). The process begins with the increasing angle of attack of the wing. During this portion of the oscillation cycle, a viscous, high-vorticity boundary layer is formed on the upper surface of the wing. This layer initiates due to viscous diffusion and the pressure gradients formed by the wing dynamics. The low-momentum, high-vorticity layer near the leading edge resists external velocities and moves forward on the wing. As the sinusoidal cycle progresses toward maximum angle of attack, the geometric α

change diminishes while the effective α continues to increase. Even during the decreasing α downstroke of the cycle, the effective α remains high creating high potential flow velocities which cause the outer flow forces to overcome the inner, viscous, reverse flow resistance. In this cyclic region, the surface vorticity coalesces into a large scale dynamic stall vortex. This vortex continues to grow and disturb the potential flow as α decreases. As α decreases toward minimum, the potential flow forces the rotating vortex to traverse the wing surface toward the trailing edge. This dynamic stall process is observed for wing geometries far inboard from the wingtip effect.

The initiation and growth of a large scale vortex is isolated forward and aft of the minimum pressure point on the chord of the wing. Under most dynamic conditions, a second seemingly same rotational, large scale vortex, smaller than the leading edge structure, is formed aft of this minimum pressure location. This second vortex also traverses the wing during the downstroke of the cycle. As this aft structure sheds from the trailing edge of the wing, the leading edge vortex decreases in size and, in some dynamic cases, dissipates into a shear layer and is no longer discernible on the upper surface. This phenomenon is observed by flow visualization and documented by anemometry techniques.

The explicit roles of three-dimensional sweep geometry in vorticity formation, transport and accumulation can now be

discussed further. The unsteady fluid motion elicited by the oscillating FSW illustrates more diverse flow characteristics than the other two wing geometries. The wingtip effect and natural inboard spanwise flow presumably cause the distinct vorticity localizations. The wingtip flow from pressure to suction side of the wing remained strong throughout the pitching cycle. Top view photography recorded inboard spanwise flow aft of the minimum pressure chord position as far inboard along the span as S = 1.00c. The spanwise pressure gradients which cause this flow seem responsible for preventing the traversing of the leading edge vortex through this aft chord region. Vorticity accumulation near the leading edge was suppressed at span locations proximal to the wingtip. A small, weaker (shown by anemometry) dynamic stall vortex formed near the leading edge. The size and strength of this vortex increased with inboard span location. As convection began, this leading edge structure decreased in size and dissipated into the shear layer. This leading edge dissipation and shear layer formation coincided with shedding of the midchord vortex. The potential flow above the viscous region did remain somewhat contoured to the wing upper surface and no full, cataclysmic stall was noted even at high α values. This phenomenon may enhance lift characteristics when compared to non-pitching wings.

The flow characteristics about the unsteady STW also illustrated three-dimensional wingtip effects but not as far

inboard as for the FSW. Again, the leading edge vortex size increased as distance from the wingtip increased. The dissipative effect on the leading edge vortex was noted until an inboard span location of S = 0.33c was reached. The dynamic stall vortex size decrease coinciding with midchord vortex shedding continued until S = 0.67c. At S = 1.00c, the large scale vortex increased in size when the midchord vortex was shed into the wake. Farther inboard, the transient separation phenomena behaved nearly identical to the S = 0.67c location. The STW unsteady flow dynamics may provide greater lift enhancement advantages than those observed for the FSW.

The ASW geometry provided nearly complete spanwise sites for vorticity transport and accumulation into large scale dynamic stall vortices. The disturbance of the potential flow by the leading edge vortex was recorded even at the wingtip location. Presumably, the natural root-to-tip spanwise flow across the ASW stimulates vorticity accumulation and dynamic stall near the leading edge. The leading edge vortex continued to enlarge throughout the pitching cycle, and in some dynamic cases enveloped the entire upper surface of the wing before shedding into the wake. A decrease in dynamic stall vortex size and a shear layer effect were noted for the ASW near the wingroot. Since the wing surface area covered by the vortical structure is significantly larger for the ASW, this geometry may provide the ideal fluid dynamic characteristics for unsteady lift

enhancement.

Application to Advanced Prototype

The complex geometry of the X-29 model precipitates unique three-dimensional airflow patterns during both static and dynamic tests. Flow visualization techniques were used to record these patterns and demonstrate flow characteristics. The multiple-exposure, stroboscopic photography utilized during both static and dynamic tests verified flow field reproducibility and illustrated turbulence levels. Smooth, cohesive smoke line contours indicated completely superimposed streaklines and consistant flow patterns throughout the multiple exposure. The random, multi-streaklined appearances contrast the more turbulent flows. Some highly turbulent regions appear as faint, white areas due to the smoke diffusion and light illumination. The vertical smoke plane was introduced only at the canard midspan, however, crossing streakline patterns demonstrate overlapping three-dimensional flows seen from the side view. This three-dimensionality is confirmed by the rear view photographs.

The bending of cohesive streaklines in front of, behind and well above the canard and wing surfaces depicts flow alterations caused by parameter changes. Angular deflections of the smoke lines in front of the canard, when compared with model centerline, indicate upwash and effective angle of attack increase of the canard. The flow lines passing near the surface of the canard and then about the wing surface show canard

downwash and w ng effective angle of attack. This pattern of upwash and downwash can also be seen in the bending of flow lines far above the surfaces. The up-down-up-down pattern observed above the surfaces is caused by the canard upwash then downwash followed by the wing upwash then downwash. All of these flow patterns are utilized in the comparative analysis between parametric effects on static and dynamic data.

Variations in canard angle of attack during static tests caused upwash, downwash, wingtip and turbulence level changes in the overall flow field. As α increased, the canard downwash increased and wing effective angle of attack decreased until complete canard stall occurred. This fully developed stall also eliminated the tip vortex and created a large turbulent wake region behind the canard. Useful flight characteristics may be to be lost when the canard angle reaches that of full stall. The three-dimensional flow traces around the canard tip at very high angles of attack indicate a high drag, low lift condition. The wing root may still be generating lift at higher AOA values. This attached, lift-producing wing flow is evidenced in the rear view photographs by the flow lines passing around the canard and then moving back toward the wing surface. Flow patterns outboard of the root area of the wing were not investigated during these tests.

Variations in model AOA caused similar flow differences in both static and dynamic tests. Since the model centerline was

varied in 5° increments, the wing geometric angle of attack also changed by this amount. An increase in model AOA caused upwash and effective angle of attack increase. This increase produced earlier static canard stall and larger dynamic canard leading edge vortices. A three-dimensional effect is seen at AOA of 5°and 10° that was not observed when the model centerline was aligned with the freestream flow. AT 5° and 10° AOA, the smoke flow under the wing is pulled outboard and entrained in the canard tip vortex. This marked tip vortex is observed under most high AOA test conditions to pass well above the wing top surface. This canard tip vortex appears pulled up and over the wing by the upwash created in front of the wing leading edge by the increased circulation about the wing root. The rear view photographs show flow patterns passing over the canard and then being drawn spanwise inboard toward the wing root. Since tip-to-root spanwise flow is characteristic for a forward swept wing, this spanwise effect, felt upstream, may be somewhat responsible for the increased three-dimensional flow about the canard. Since the smoke flow impinges the wing near the root location, the increased turbulence seen at 10° AOA exemplifies the root-to-tip stall characteristics observed previously on the forward swept wing configuration.

In the small amplitude (±5°) oscillation tests, model AOA and mean angle of attack changes kept the angular oscillations constant with respect to the tunnel freestream. As model AOA

increased, the mean angle was decreased. Therefore, the observed effects resulted principally from the flow field changes due to the model and wing angle of attack. The canard leading edge vortices were larger in size and initiated only slightly earlier for the higher model AOA test condition. Canard leading edge vortex formation and convection tendencies were identical at each AOA for this oscillation amplitude. When the leading edge vortex began to traverse across the top surface of the canard, convection occurred very quickly and the vortex progress from the leading edge to shedding into the wake took less than one third of the pitching cycle. As shedding was complete, the flow collapsed toward the canard surface and a new vortex began to form. Identical unsteady flow characteristics were observed for higher amplitude (±10°) oscillations with increased angular travel producing flow alterations of slightly larger magnitude.

The sinusoidal pitching motion of the canard produced cyclic wing effective angle of attack changes and upper and lower wing surface protrusions. When the canard begins the increasing angle of attack phase of the cycle, the downwash from the canard begins to increase and this decreases the effective angle of attack of the wing. This downwash, recorded by the smoke flow, extends well beneath the lower surface of the wing. When the canard sinusoidally reverses angular direction and begins the decreasing α portion of the cycle, the downwash decreases and the wing effective angle of attack increases. This increase then

decrease in downward flow near the leading edge of the wing causes a downward protrusion under the wing surface. The protrusion is caused temporally and spatially by the cyclic upwash and downwash. The horizontal lenght of the protrusion is the distance the freestream flow travels in one half of a pitching cycle. The spatial distance beneath the wing surface is proportional to the downwash from the canard. This vertical distance, like the downwash angle, increases with mean angle and oscillation amplitude. The under-wing protrusion contains three-dimensional overlapping patterns seen from side view photographs. Exact flow description of this area can only be achieved using measured flow properties such as pressure and velocity.

Similar to the under-wing protrusion caused by downwash, an over-wing protrusion is seem at high amplitude canard oscillations which cyclically produce upwash at the wing leading edge. The cyclic disturbance passing over the top surface of the wing appears to be caused by a combined effect of traversing leading edge vortex and upward protrusion similar to lower surface flow. The upward protrusion is forming on the wing upper surface while the leading edge vortex is near the trailing edge of the canard. The canard trailing edge downward motion which terminates the upward protrusion also occurs at the cycle position where the leading edge vortex is shed from the canard trailing edge. Therefore, the upstream edge of the protrusion contains the rotational vortex shed from the canard and passing

over the wing surface.

The lower surface protrusion contains three-dimensional rotating flow which causes spanwise vortical structure formation. This can be seen in side and rear view photographs as overlapping flow patterns, lobbing effects and under-wing vortex development. This phenomenon appears due to rotational flow imparted to the under wing area by the canard tip vortex and a very high cyclic angle of incidence at the wing leading edge. Under certain dynamic conditions, a clockwise-rotating vortex is formed when the protrusion is clipped by the upward motion of the canard trailing edge. The immediate canard wake during upward motion of the trailing edge creates an extremely high angular incidence at the wing leading edge. This high angular flow slapping the lower surface of the wing deflects from the surface and rolls into the observed vortex. This lobbing and concentrated vortex flow is observed clearly in the plane of smoke introduction and, also, farther outboard as a smaller replica closer to the wing lower surface. The concentrated vorticity expands and dissipates in the viscous flow as the pitching cycle progresses.

Reducing K value had the effect of increasing turbulence levels and decreasing any traversing tendencies of the canard leading edge vortex. The turbulence levels of the flow aft of the canard increased for all oscillation amplitudes tested. Flow patterns in front of the canard seemed nearly unchanged by the K value reduction. The canard leading edge vortex cyclically

developed then dissipated into a shear layer with no convective tendencies observed. The canard tip vortex was not marked by the smoke drawn outboard along the lower canard surface. These characteristics indicate possible reduced pressure intensities during the lower frequency oscillations.

In summary, the experiments discussed here attempted to provide a logical progression toward comprehension of unsteady flow characteristics about finite wings of varying sweep geometry. The initial flow visualizations of the smoke patterns about the oscillating forward swept wing illustrated spatial and temporal variations in vorticity accumulation and development. Since the initial data had no comparative base, the next logical investigation included three sweep geometries at identical static and dynamic test conditions. Quantitative comparisons of distinct flow characteristics were accomplished throughout oscillation cycles for the entire surface areas of the three wings. Since the flow field dynamics cannot be completely described using flow visualization techniques alone, hot wire anemometry measurements were recorded for test conditions identical to the visualized data. A concluding effort to this unsteady flow research is an attempt at realizing possible application of this still not fully understood technology. The investigations conducted on the complex geometry X-29 model demonstrate flow characteristics which may verify unsteady flow benefits to the aerodynamics of future aircraft.

CHAPTER IX

CONCLUSIONS

Three-dimensional effects are indispensable in the application of aerodynamic technology to tangible aircraft. Finite wings produce flow fields with differential flow characteristics as various spanwise positions are investigated. Since three-dimensional unsteady fluid dynamics is still in somewhat of an inception phase, little is known about finite wing, unsteady aerodynamics. To expand comprehension of these unsteady effects, flow characteristics were investigated at various span locations using both visualization and anemometry techniques. Because high performance aircraft must incorporate swept wings, unsteady flow over various sweep geometries were tested. Each experiment provided greater insight into the behavior of unsteady flow and further conclusions about possible utility of this phenomenon.

The studies of finite wings have for many years investigated the effects of the wingtip vortex along the span of the wing. Two-dimensional, unsteady aerodynamic studies have predicted the formation and development of leading edge vortices produced by sinusoidal airfoil motions. The application of this possibly beneficial technology to finite wings must realize the

effects of the wingtip vortex in this unsteady flow. Initial unsteady investigations on a straight, symmetrical finite wing (Adler and Luttges, 1985) show that complex interactive regions exist between unsteady wingtip and leading edge vortices. For the straight wing, three distinctive characteristic regions were observed: (1) the wingtip region dominated by the wingtip vortex; (2) the midspan region where wingtip and leading edge vortices interacted; and (3) the wingroot region dominated by the leading edge vortex much like two-dimensional unsteady flows. These initial finite wing studies also noted a direct correlation between spanwise deflection of airflow at the wingtip and the apparent circulation about the wing in this region.

The forward swept wing tests discussed in this text statically and dynamically produced flow fields that differed significantly from those reported for the straight, symmetric wing. In the static tests, the inboard span of the FSW stalled at lower angles of attack than outboard span areas. The flow about the wingtip did not separate even at angles of attack approaching 30°. In dynamic pitching tests, the swept forward wing differed from the symmetric wing primarily in regard to the manner in which the leading edge vortex developed along the span. The development of inboard vortices occurred at lower angles of attack than that of tipward vortices across all K values and mean angles of attack. The wingtip effect suppressed dynamic stall vortex formation, size and convective tendencies at span

locations within 1.0c of the wingtip. Areas along the span of interacting tip and leading edge vortices show more flow field capriciousness than was evident using a symmetric wing.

Since the straight, symmetric wing and the FSW wingtip geometries were not identical, spanwise deflection angles at the tip could not be directly compared. The FSW static and instantaneous dynamic β angle measurements correlate, however, with inboard flow visualizations to confirm wing circulation near the wingtip. Comparisons of β angles for identical geometry wingtips were accomplished in later experiments.

As observed in experiments using two-dimensional airfoils, plates, and a three-dimensional wing, increases in K value result in leading edge vortex appearance at higher angles of attack in the upward pitching motion. This delay is invariably matched by a higher V_c value. Opposite effects are seen for increases in the mean angles of attack around which pitching occurs. However, within approximately 0.5c of the FSW wingtip the relationships appear to reverse in that higher K values result in larger vortex size and slower apparent V_c. At these span locations, increases in mean angle do not ameliorate the effects of K value.

It is interesting to note that previous studies have shown that airfoils and plates across a variety of Re numbers elicit quite similar dynamic flow field changes. The upward motion generates a leading edge vortex that passes over the chord

to the trailing edge. Depending upon K value, a trailing edge vortex is elicited with opposite sign. This trailing edge vortex often causes a rapid separation of the flow from the airfoil surface. Such conditions are associated with cataclysmic stall. In the forward swept wing studies there was little evidence for the presence of a trailing edge vortex. This large scale, trailing edge vortex absence seems a characteristic of the finite wing. Dynamic flow separation was not coincidental with the passage of the leading edge vortex into the wake.

The work of Gad-el-Hak and his colleagues, 1984-86, and that of Carta, 1984, shows that the swept back and delta wings also seem to have little evidence of a trailing edge vortex. Both series of investigations suggest that vortices form over the upper surfaces at high angles of attack and that these vortices simply increase or decrease in size as pitching is introduced. In these instances it is easy to imagine that an induced leading edge vortex simply adds to the existing vortices over the two different test surfaces.

Recent work by Freymuth and his colleagues (1986) gives a rather suggestive view of the three-dimensional vorticity that supports some of the flow field structures observed here and previously using swept forward and symmetric wings. In a recent study, a symmetric wing was marked with $TiCl_4$ just prior to initiating a flow that accelerated linearly from rest to approximately 40 feet per second. The vorticity of both the

wingtip and the leading edge was evident. Across a wide range of angles of attack the vorticity accumulated across the leading edge in a pattern like that described for the area that supports the pitch-induced vortices. The tip vorticity showed a pattern reminiscent of that described for the helical pattern of the tip vortex. Between these two areas there was no apparent accumulation of vorticity. Higher angles of attack in the acceleration experiments resulted in areas of vorticity that converge over the surface of the wing, but these two areas do not ever exhibit complete convergence. It seems possible that the upward pitching swept forward wing brings underlying areas of vorticity close together as in Freymuth's experiments.

The comparative spanwise flow visualization tests on the FSW, STW and ASW indicate that sweep angles can have a major influence on the static stall characteristics of the wings and in turn, the generation and development of unsteady separated flows on pitching wings. The spanwise static stall characteristics for each wing configuration enhance predictability of dynamic responses. At span locations where static stall is known to be fully developed, the leading edge vortex structure is seen to be larger and more resistant to other flow influences. This is indicated by inboard locations on the FSW, most spanwise positions on the STW and by regions adjacent to the wingtip on the ASW. At span positions where static stall occurs only at very high α, near the wingtip for the FSW and far inboard for

the ASW, the dynamic leading edge vortex development is suppressed. Also, these leading edge structures are likely to be lost to the distributed vorticity of a shear layer.

Dynamic responses to sweep angles show characteristics that depend on both wing configuration and wing span location. In some cases, the leading edge vortex growth and convection were reminiscent of airfoil tests or previous wing tests where results were collected at sites distal to the wingtip. Other conditions show additional wingtip and leading edge vortex interactive effects.

At the wingtip for each wing, the dynamic β hysteresis loops show direct relationships to the presence or absence of a leading edge vortex on the wing surface. When a fully developed leading edge vortex is formed on the inboard surface, the dynamic β is highest and goes to a minimum when the leading edge structure has shed or is no longer discernible on the top surface. The overall higher average β hysteresis loops verses the static β values indicate that dynamic pitching may enhance lift production more for the STW and ASW than for a FSW which already demonstrates favorable high angle of attack lift characteristics.

The effect of wing sweep at different span locations can also be quantified by leading edge vortex size as well as vortex position on the wing surface. For the FSW, as span positions closer to the wingtip are examined, the leading edge vortex

decreases in size and resists convection. This characteristic is observed, to a lesser extent, for the STW. The ASW, however, shows a tendency toward larger leading edge vortical structures near the wingtip and smaller leading edge vortices far away from the wingtip. These overall characteristics, as noted earlier, seem related to static stall areas. The FSW leading edge vortex development and convection are influenced farther inboard along the wing span by the wingtip effect than STW and ASW counterparts. The leading edge vortex convection for the FSW is suppressed and even eliminated by a shear layer for span locations near S = 1.0c. This suppression is observed for the STW for a distance of only S = 0.33c inboard and little effect is seen for the ASW. The larger leading edge structures formed near the wingtip on the ASW seem to be able to resist the wingtip effect and to convect in a manner more like that observed on airfoils.

Increasing K causes what appears to be more energetic vortex development seen on the top surface of the STW. This leads to the formation of multiple vortices during early portions of the downstroke of the pitching cycle. A splitting of the highly energetic leading edge vortex occurs midway through the downward pitching cycle. A smaller, primary leading edge vortex remains near the leading edge while a larger, seemingly more turbulent vortex splits from the downstream side of the flow structure. These distinct structures then separately traverse

the wing and shed from the trailing edge. This splitting may indicate a high level of vorticity present on the top wing surface capable of supporting three distinct vortices. Or, the available vorticity may be quite differently distributed on the wing surface. In any event, higher K values for the STW may imply more vorticity and possibly greater lift enhancement when utilized.

Both flow visualization and anemometry techniques verify the dynamic spatial and temporal differences in the unsteady flow fields produced about the three sinusoidally oscillating wings differing in sweep angles. Flow visualization techniques were used to record the leading edge vortex size, position and convective tendencies. This procedure elucidates and documents comparative sweep angle effects since flow visualization photographs for each of the three wing geometries were compared for the same dynamic, chordwise and spanwise locations. The hot wire anemometry data, although not precise because of flow angularity, provide comparative corroboration of flow visualization results. The measured local velocity fluctuations revealed and documented position, size and relative velocities of the flow field structures.

Chordwise anemometric investigations conducted over the complete pitching cycle verified the formation, development and convection of the visualized leading edge vortex structure. The largest velocity peaks always occurred at C = 0.17c where

vorticity was accumulating into a very cohesive leading edge structure. As this structure enlarged and convected, rotational energy dissipated and measurements in the vortex circumference indicated reduced V/V_∞ values. Chordwise investigations, when applied at identical span locations for all three wings defined significant differences in the unsteady flow field characteristics of each wing.

The spanwise comparison of flow visualization and anemometry data shows that wing sweep angles produced major changes in vortex initiation, development and convection velocity. The different interaction regions between wingtip and leading edge vortices are dramatically resolved by comparing visualized flow with recorded anemometric data. The wingtip effect suppresses the leading edge vortex near the wingtip. This effect increasingly influences the transient vorticity accumulation regions of the wing for the ASW, STW and FSW respectively. The dynamic stall characteristics of the ASW allow resistance of the wingtip effect to span positions proximal to the wingtip.

During most dynamic tests, a primary leading edge vortex and a second vortex formed near midchord were observed on the wing surface away from the wingtip effect. Flow field influences exist on the FSW and STW which decrease the size and dissipate the dynamic stall vortex when the midchord vortex sheds into the wake. As the midchord or primary vortex is shed into the wake,

no counter-rotating trailing edge vortex is observed. The three-dimensional effect elicits free-vorticity shedding from the trailing edge but inhibits accumulation into a large scale trailing edge vortex.

The above noted differences in wing sweep angle effects on unsteady flow structures will undoubtedly affect ultimate utilization schemes on new technology aircraft. This work shows that unsteady flow three-dimensionality can be made to vary in different but reliable fashion. For example, wing sweep angle can reliably dictate the flow structures likely to pass over downstream aircraft control surfaces. These are important facets to integrate into future methodologies devised for controlling unsteady flow structures use on aircraft such as the X-29.

The very complex geometry of the X-29 model makes analysis of variations caused by a single parameter change eminently difficult. Static and dynamic flow visualization photography serves to minimize comparative difficulties and to examine flow characteristics which may disclose beneficial unsteady flight conditions. This technique is limited to comparative analysis and a complete flow field investigation must include both velocity and pressure measurements. Visualized elicited flow patterns, when analyzed using known physical flow properties such as stall, upwash, downwash and tip effect, can be extrapolated as possibly useful phenomenon.

Slow airspeed, high angle of attack flight of the static

model substantiates adverse flow conditions where some type of aerodynamic flow control device may be beneficial. Increased model AOA caused early canard stall and possibly disruptive wing lifting conditions in the wake of the stalled canard. Higher AOA values also seemingly created exorbitant three-dimensional effects shown by increased spanwise flow on the canard and overlapping flow patterns about the wing. The advantages of applied unsteady flow producing devices seem to be in maintaining attached flow at high AOA values over both the canard and wing surfaces.

Dynamic sinusoidal oscillations of the canard produce cyclic unsteady flow fields about the canard and wing which may be beneficial in delaying separation. Airflow in the immediate vicinity of the canard remains attached to the surface throughout the pitching cycle. The only disturbance of the airflow is the formation and development of the leading edge vortex. This dynamic vortex formation has been shown in numerous airfoil and wing tests to be beneficial in enhancing lift characteristics. Therefore, the increased overall flow attachment and the high energy leading edge vortex development on the surface of the canard may increase lift production well above the static high angle of attack values.

Increased flow attachment on the canard surface causes a nearly continuous downwash aft of the canard. This decreases the effective angle of attack of the wing in the root area. The

stall characteristics of the forward swept wing have been shown in experiments discussed in this text to be from root-to-tip. Therefore, this decrease in effective angle of attack near the root area may delay the overall onset of separation on the wing. Further investigations at multiple span locations across the wing span should evidence the exact spanwise separation tendencies and the contribution of the unsteady flow from the canard.

The protrusions on the surface of the wing are caused mainly by the cyclic upwash and downwash changes from the canard. Such complex flow patterns cannot be fully described with flow visualization data alone. These areas must be examined using other flow measuring techniques such as hot wire anemometry and surface pressure. Under certain dynamic conditions, the protrusions exhibit embedded, three-dimensional vortex structures which may produce very complex flow field variations across the wing surface.

Summary

This research has focused on the three-dimensional, forced unsteady flow characteristics elicited about finite wings with distinct sweep geometries. Wing spatial and temporal variations in vorticity transport and accumulation sites are recorded by both flow visualization and anemometry techniques. Dissimilar flow characteristics were observed at disparate spanwise and chordwise locations on the FSW, STW and ASW when tested under identical dynamic conditions. Cyclic temporal flow

behavior also evinces contrasting characteristics when compared at spatially identical wing locations. These fluctuations are attributed to the variable wingtip influence for each finite wing geometry. Wing sweep geometry and span location were the dominant flow-changing parameters. Vorticity accumulation into the wingtip vortex cyclically varied in intensity (shown by β angle and velocity measurements) for each wing. The ASW produced flow fields which caused the greatest fluctuations in the wingtip vortex dynamic qualities. Proximity to the wingtip precipitated leading edge vortex suppression in both size and convective tendencies. This wingtip effect prevents distributed vorticity in the shear layer from accumulating into a large scale vortex structure. In some instances, vorticity accumulates into the large scale leading edge vortex only to dissipate back into distributed form during later portions of the pitching cycle. The FSW geometry created upper surface flows which spanwise perpetuated the wingtip effect to nearly one chordlength inboard. This effect existed spanwise on the STW until nearly midchord and was observed on the ASW only very near the wingtip. This cyclic leading edge vortex formation then dissipation was also observed on the oscillating canard of the X-29 model. Flow over the wings distal to the wingtip effect reveals vorticity accumulation, vortex development and convection characteristics similar to two-dimensional airfoil data. Variations in dynamic parameters caused differing spatial and temporal effects on each wing

geometry. Increasing K value from 0.6 to 1.4 causes smaller leading edge vortex structures and higher convecting velocities at span locations away from the wingtip effect. This K value increase also produced slightly greater velocity fluctuations and leading edge vortex dividing on the STW. In general, increasing mean angle of attack for the FSW provoked earlier vortex formation and higher convective velocities. A comprehensive analysis of the data presented here provides insight into the time-dependent generation and use of vorticity on the surface of the three finite wing geometries.

To ultimately comprehend the three-dimensional, finite wing effects in unsteady aerodynamics, the time-dependent generation of vorticity into the wingtip vortex, leading edge vortex and the interactions of these phenomenon must be understood. Several approaches to this realization may culminate in feasible application of this technology to modern and future aircraft. The studies discussed in this text were accomplished to provide a beginning into comprehension of a relatively novel area. These tests depict unsteady flow characteristics about three wing geometries over a moderate parameter range. Other experiments must continue to explore the parameter envelope throughout multiple test media. Future work should focus on the exact magnitudes of the spatial and temporal generation and use of elicited vorticity. A vast data base must be established in this very complex three-dimensional area of finite wing unsteady

aerodynamics. Without a comprehensive data base, attempts at modelling and application of this technology seem premature.

BIBLIOGRAPHY

Adler, J.N. and Luttges, M.W.,"Three-Dimensionality In Unsteady Flow About a Wing," AIAA-85-0132, AIAA 23rd Aerospace Sciences Meeting, Reno, Nevada, Jan. 1985.

Adler, J.N., Robinson, M.C., Luttges, M.W. and Kennedy, D.A., "Visualizing Unsteady Seperated Flows," Third International Symposium on Flow Visualization, Proceedings, Vol. III, Ann Arbor, Michigan, Sept. 1983, pp. 806-811.

Anderson, J.D., Jr., Introduction to Flight, McGraw-Hill Book Company, New York, 1978.

Ashworth, J. and Luttges, M.,"Comparisons in Three-Dimensionality in the Unsteady Flows Elicited by Straight and Swept Wings," AIAA-86-2280CP, AIAA Atmospheric Flight Mechanics Conference, Williamsburg, Virginia, August 1986.

Ashworth, J., Waltrip, M. and Luttges, M.,"Three-Dimensional Unsteady Flow Fields Elicited by a Pitching Forward Swept Wing," AIAA-86-1104, AIAA 4th Joint Fluid Mechanics, Plasma Dynamics and Lasers Conference, Atlanta, Georgia, May 1986.

Batina, J.T., "Unsteady Transonic Flow Calculations for Two-Dimensional Canard-Wing Configurations," Journal of Aircraft, Vol. 23, No. 4, April 1986.

Busemann, A., "Compressible Flow in the Thirties," Annual Review of Fluid Mechanics, Vol. 3, 1971.

Carr, L.W., "Dynamic Stall Progress in Analysis and Prediction," AIAA-85-1769CP, AIAA Atmospheric Flight Mechanics Conference, Snowmass, Colorado, Aug. 1985.

Carta, F.O.," Unsteady Stall Penetration of an Oscillating Swept Wing," Workshop on Unsteady Separated Flows, Francis, M. and Luttges, M. (eds.), University of Colorado: 1984, pp. 28-37.

Chow, C.Y.,An Introduction to Computational Fluid Mechanics, Seminole Publishing Company, Boulder, Colorado, 1983.

Duke, E.L., Jones, F.P. and Roncoli, R.B., "Development and Flight Test of an Experimental Maneuver Autopilot for a Highly Maneuverable Aircraft," NASA Technical Paper 2618, Sept. 1986.

Freymuth, P., Bank, W. and Palmer, M., "Vortices Around Airfoils," American Scientist, Vol. 72, May-June 1984, pp. 242-248.

Freymuth, P., Finaish, F. and Bank, W., "Three-Dimensional Vortex Patterns in a Starting Flow," Journal of Fluid Mechanics," Vol. 161, 1985, pp. 235-248.

Freymuth, P., Finaish, F. and Bank, W., "Visualization of Wing Tip Vortices in Accelerating and Steady Flow," Journal of Aircraft, Vol. 23, No. 9, Sept. 1986, pp. 730-733.

Freymuth, P., "The Vortex Patterns of Dynamic Separation: A Parametric and Comparative Study," Progress in Aerospace Sciences, Vol. 22, 1985, pp. 161-288.

Gad-el-Hak, M. and Ho, C., "Three-Dimensional Effects on a Pitching Lifting Surface," AIAA-85-0041, AIAA 23rd Aerospace Sciences Meeting, Reno, Nevada, Jan. 1985.

Gad-el-Hak, M. and Ho, C.," Unsteady Vortical Flow Around Three-Dimensional Lifting Surfaces," AIAA Journal, Vol. 24, No. 5, pp. 713-721, May 1986.

Gad-el-Hak, M., Ho, C. and Blackwelder, R.F., "A Visual Study of a Delta Wing in Steady and Unsteady Motion," Workshop on Unsteady Separated Flows, Francis, M. and Luttges, M. (eds.), University of Colorado: 1984, pp. 45-51.

Griffin, K.E., Haerter, E.C. and Smith, B.R., "Wake Characteristics and Interactions of the Canard/Wing Lifting Surface Configuration of the X-29 Forward-Swept Wing Flight Demonstrator," USAFA-TN-83-7, 15 Aug. 1983.

Helin, H.E. and Walker, J.M., "Interrelated Effects of Pitch Rate and Pivot Point on Airfoil Dynamic Stall," AIAA-85-0130, AIAA 23rd Aerospace Sciences Meeting, Reno, Nevada, Jan. 1985.

Helin, H.E., Robinson, M.C. and Luttges, M.W., "Visualization of Dynamic Stall Controlled by Large Amplitude Pitching Motions," AIAA-86-2281-CP, AIAA Atmospheric Flight Mechanics Conference, Williamsburg, Virginia, Aug. 1986.

Herbst, W.B., "Supermaneuverability," Workshop on Unsteady Separated Flows, Francis, M. and Luttges, M. (eds.), University of Colorado: 1984, pp. 1-9.

Hoey, B., "Experimental: As in X-29A," AIRMAN, Vol. XXIX, No. 4, AFRP 30-15, pp. 28-34, April 1985.

Karamcheti, K., Principles of Ideal-Fluid Aerodynamics, John Wiley and Sons, New York, 1966.

Kuethe, A.M. and Chow, C.Y., Foundations of Aerodynamics: Bases of Aerodynamic Design, Third Edition, John Wiley and Sons, New York, 1976.

Landfield, J.P. and Rajkovic D., "Canard/Tail Comparison for an Advanced Variable-Sweep-Wing Fighter," Journal of Aircraft, Vol. 23, No. 6, June 1986.

Luttges, M.W., Somps, C., Kliss, M. and Robinson, M., "Unsteady Separated Flows: Generation and Use by Insects," Workshop on Unsteady Separated Flows, Francis M. and Luttges, M. (eds.), University of Colorado: 1984, pp. 127-136.

Luttges, M.W., Robinson, M.C. and Kennedy, D.A., "Control of Unsteady Separated Flow Structures on Airfoils," AIAA-85-0531, AIAA Shear Flow Control Conference, Boulder, Colorado, March 1985.

Mann, M.J. and Mercer, C.E., "Forward-Swept-Wing Configuration Designed for High Maneuverability by Use of a Transonic Computational Method," NASA Technical Paper 2628, Nov. 1986.

Martin, J.M., Empey, R.W., McCroskey, W.J. and Caradonna, F.X., "An Experimental Analysis of Dynamic Stall on an Oscillating Airfoil," Journal of the American Helicopter Society, Jan. 1974, pp. 26-32.

McAlister, K.W. and Carr, L.W., "Water Tunnel Visualizations of Dynamic Stall," Journal of Fluids Engineering, Vol. 1D1, Sept. 1979, pp. 376-380.

McCormick, Barnes W., Aerodynamics, Aeronautics, and Flight Mechanics, John Wiley and Sons, New York, 1979.

McCroskey, W.J., Carr, L.W. and McAlister, K.W., "Dynamic Stall Experiments on Oscillating Airfoils," AIAA-75-125, AIAA 13th Aerospace Sciences Meeting, Pasadena, California, Jan. 1975.

McCroskey, W.J., "Unsteady Airfoils," Annual Review of Fluid Mechanics, 1982, pp. 285-311.

Moore, M. and Frei, D., "X-29 and Forward Swept Wing Aerodynamic Overviews," AIAA-83-1834, AIAA Applied Aerodynamics Conference, Danvers, Massachusetts, July 1983.

Reisenthel, P.H., Nagib, H.M. and Koga, D.J., "Control of Separated Flows Using Forced Unsteadiness," AIAA-85-0556, AIAA Shear Flow Control Conference, Boulder, Colorado, March 1985.

Reynolds, W.C. and Carr, L.W., "Review of Unsteady, Driven,

Separated Flows," AIAA Shear Flow Control Conference, Boulder, Colorado, March 1985.

Robinson, M.C., Helin, H.E. and Luttges, M.W., "Control of Wake Structure Behind an Oscillating Airfoil," AIAA-86-2282-CP, AIAA Atmospheric Flight Mechanics Conference, Williamsburg, Virginia, Aug. 1986.

Robinson, M.C. and Luttges, M.W., "Unsteady Flow Separation and Attachment Induced by Pitching Airfoils," AIAA-83-0131, AIAA 21st Aerospace Sciences Meeting, Reno, Nevada, Jan. 1983.

Robinson, M.C. and Luttges, M.W., "Unsteady Separated Flow: Forced and Common Vorticity About Oscillating Airfoils," Workshop on Unsteady Separated Flows, Francis, M. and Luttges, M. (eds.), University of Colorado: 1984, pp. 117-126.

Robinson, M.C. and Luttges, M.W., "Vortex Generation Induced by Oscillating Airfoils: Maximizing Flow Attachment," 8th Biennial Symposium on Turbulence, Rolla, Missouri, Sept. 1983, pp. 13.1-13.10.

Robinson, M.C., Gilliam, F., Helin, H., Russell, J. and Walker, J., "Visualization of Three-Dimensional Forced Unsteady Separated Flow," AIAA-86-1066, AIAA 4th Joint Fluid Mechanics, Plasma Dynamics and Lasers Conference, Atlanta, Georgia, May 1986.

Saharon, D. and Luttges, M., "Three-Dimensional Flow Produced by a Pitching-Plunging Model Dragonfly Wing," AIAA-87-0121, AIAA 25th Aerospace Sciences Meeting, Reno, Nevada, Jan. 1987.

Schlichting, H., Boundary Layer Theory, McGraw-Hill Book Company, Sixth Edition, 1968.

Somps, C. and Luttges M., "Dragonfly Flight: Novel Uses of Unsteady Separated Flows," Science, Vol. 228, 14 June 1985.

Telionis, D.P. and Mathioulakis, D., "On the Shedding of Vorticity at Separation," Workshop on Unsteady Separated Flows, Francis M. and Luttges, M. (eds.), University of Colorado: 1984, pp. 106-116.

Tierney, J., "The Real Stuff," Science 85, American Association for the Advancement of Science, Sept. 1985.

Uhuad, G.D., Weeks, J.M. and Large, R., "Wind Tunnel Investigation of Transonic Aerodynamics Characteristics of Forward Swept Wings," Journal of Aircraft, 20(3), March 1983, pp. 195-202.

Walker, J., Helin, H. and Chou, D., "Unsteady Surface Pressure Measurements on a Pitching Airfoil," AIAA-85-0532, AIAA Shear Flow Control Conference, Boulder, Colorado, March 1985.

Walker, J.M., Helin, H.E. and Strickland, J.H., "An Experimental Investigation of an Airfoil Undergoing Large-Amplitude Pitching Motions," AIAA Journal, Vol. 23, No. 8, Aug. 1985.

Whipple, R.D. and Ricket, J.L., "Low-Speed Aerodynamic Characteristics of a 1/8-Scale X-29A Airplane Model at High Angles of Attack and Sideslip, " NASA Technical Memorandum 87722, Sept. 1986.

White, F. M., Viscous Fluid Flow, McGraw-Hill Book Company, 1974.

END

DATE

FILMED

JAN

1988